RADIATIVE IMPACT OF CRYOSPHERE ON THE CLIMATE OF EARTH AND MARS

by

Deepak Singh

A dissertation submitted in partial fulfillment
of the requirements for the degree of
Doctor of Philosophy
(Atmospheric, Oceanic and Space Sciences)
in the University of Michigan
2016

Doctoral Committee:

Associate Professor Mark G. Flanner, Chair
Assistant Research Scientist Germán Martínez
Professor Christopher J. Poulsen
Professor Nilton O. Renno

Dedication

To my parents

Acknowledgements

Firstly, I would like to express my sincere gratitude to my advisor, Mark Flanner for the continuous support throughout the program, for his patience, motivation, and immense knowledge. I have been amazingly fortunate to have an advisor who gave me the freedom to explore on my own, and at the same time the guidance to recover when I made mistakes. I would like to thank the rest of my thesis committee for their encouragement and insightful comments on this thesis.

My sincere thanks also goes to Dr. Ehouarn Millour, CNRS Research Engineer, LMD, France, for providing Mars GCM, and consistent support to help me sort out the technical details of the model. The collaboration with him helps me to broaden my research horizons. I am indebted to him for his continuous encouragement and guidance. Additionally, I would like to thank Mr. Darren Britten-Bozzone, Systems Administrator Intermediate in our department for helping to set up and run Mars GCM on my machine, and sort out any issues that came along the way.

I would like to thank my group members: Justin Perket, Chaoyi Jiao, Adam Schneider and Jamie Ward for their invaluable comments and suggestions related with research, stimulating discussions during meetings and their moral support.

I would also like to thank the staff members of International Center, especially John Prescott for helping me to keep all my paperwork in order, and allowing me a very peaceful stay in the country.

Last but not the least, I would like to thank my family: my parents, my little brother and my wife for their moral support throughout writing this thesis and my life in general.

Table of Contents

List of Tables

List of Figures

ABSTRACT

Radiative Impact of Cryosphere on the Climate of Earth and Mars

by

Deepak Singh

Chair: Mark Flanner

Snow- and ice-covered surfaces are the most reflective regions on Earth and Mars, and their extent can change substantially with small changes in climate. The presence of Earth's cryosphere greatly alters the planet's albedo and changes in cryospheric extent and reflectivity therefore partially determine the sensitivity of climate to anthropogenic and external forcings. Carbon dioxide ice is abundant on the Martian surface, and plays an important role in the planet's energy budget.

Firstly, we quantify the shortwave Cryosphere Radiative Effect (CrRE) on Earth. Relatively high resolution (0.05°×0.05°) MODIS (Moderate Resolution Imaging Spectroradiometer) data along with radiative kernel datasets are used to estimate the global land shortwave CrRE. We perform multiple analyses to determine the sensitivity of our estimates to the use of different thresholds for snow cover determinations, different climatologies for missing data, and radiative kernels generated with different distributions of clouds produced with various versions of the Community Atmosphere Model. We estimate a global land-based CrRE of about -2.6 Wm^{-2} during 2001-2013, with about 59% of the effect originating from Antarctica.

Secondly, we adapt the terrestrial Snow, Ice, and Aerosol Radiation (SNICAR) model to simulate CO_2 snow albedo across the solar spectrum (0.2-5.0 μm). We apply recent laboratory derived refractive indices of CO_2 ice, which produce higher broadband

CO_2 snow albedo (0.93–0.98) than previously estimated. We perform multiple analyses to determine the sensitivity of cryosphere spectral albedo to the amount and type of dust, co-presence of CO_2 and H_2O ices, ice grain size, snow layer thickness, and solar zenith angle. In addition, we also compare our simulations with observed Mars surface albedo, and achieved a reasonable fit between the two.

Finally, SNICAR is implemented with the Laboratoire de Météorologie Dynamique Mars GCM to prognostically determine ice cap (both H_2O and CO_2) albedos interactively in the model. We then explore the impact of dust on surface cryosphere albedo and its impact on Mars' shortwave energy flux. After integrating SNICAR into the Mars GCM, we find that the impact caused by dust is about 1.5 times the impact caused by the presence of snow itself on shortwave flux at the surface.

Chapter 1

Introduction

1.1 Albedo

Albedo or reflection coefficient (from the Latin *albus* for "white") is defined as the ratio of reflected radiation from the surface to incident radiation upon it. Albedo depends on the frequency of the radiation and the properties of the surface. In general, the albedo also depends on the directional distribution of incident radiation, except for Lambertian surfaces, which scatter radiation uniformly in all directions and have an albedo that is independent of the incident distribution.

Black-sky albedo (directional hemispherical reflectance) is defined as albedo in the presence of unidirectional incident light and is a function of solar zenith angle. It is the integration of the bi-directional reflectance over the viewing hemisphere. Bidirectional Reflectance Distribution Function (BRDF) gives the reflectance of a target as a function of illumination geometry (solar zenith angle for planetary albedo), and viewing geometry (e.g., point of view of a satellite). The BRDF depends on wavelength and is determined by the structural and optical properties of the surface, including effects such as shadow-casting, multiple scattering, mutual shadowing, transmission, reflection, absorption, and emission by surface elements, facet orientation distribution, and facet density. White-sky albedo (bi-hemispherical reflectance) is defined as albedo in the absence of a direct

component when the diffuse component is isotropic. It is the integration of the directional albedo over the illumination hemisphere.

Black-sky albedo (α_{bs}) and white-sky albedo (α_{ws}) mark the extreme cases of completely direct and completely diffuse illumination. The actual albedo is a value which is interpolated between these two, and can be written as:

$$\alpha = f_{dif} \cdot \alpha_{ws} + (1 - f_{dif}) \cdot \alpha_{bs} \tag{1.1}$$

where f_{dif} is the fraction of incident skylight that is diffuse, which is itself a function of the atmospheric optical depth at the frequency of interest [e.g., *He et al.,* 2012]. These terms are important because they allow the albedo to be calculated for any given illumination conditions from a knowledge of the intrinsic properties of the surface [*Roman et al.,* 2010]. Two common albedos used in astronomy are discussed below:

1.1.1 Geometric Albedo

Geometric albedo is the ratio of the global brightness of a planet, viewed from the direction of the Sun, to that of a hypothetical, white, and fully reflecting Lambertian sphere of the same size at the same distance [*Morrison and Owen*, 1996]. From *Chesley et al.*, [2002], the relationship between geometric albedo (p_v) with absolute magnitude (H), and diameter (D) of a celestial object is:

$$D = 1329\ km \times 10^{-H/5}\ p_v^{-1/2} \tag{1.2}$$

Absolute magnitude (dimensionless) is the measure of intrinsic brightness of a celestial object. Absolute magnitude is defined to be the apparent magnitude an object would have if it were located at a distance of 10 parsecs (32.6 light years) from Earth. The apparent magnitude of a celestial object is a number that is a measure of its brightness as

seen by an observer on Earth. The brighter an object appears, the lower its magnitude value. Some objects can be more reflective than the hypothetical idealized reference sphere, therefore geometric albedos higher than 1.0 are possible.

1.1.2 Bond Albedo

Bond albedo (named after US astronomer George P. Bond), is defined as the fraction of the total incident solar radiation reflected by a planet back into space. Bond albedo is a measure of the planet's solar energy balance and dependent on the spectrum of the incident radiation defined over the entire range of wavelengths. Since Bond albedo (A) tells us how much solar energy is absorbed, we can use it to calculate an effective temperature (T_e) of a planet using Stefan-Boltzmann law:

$$T_e = \left[\frac{(1-A)I_0}{4\sigma} \right]^{1/4} \tag{1.3}$$

where I_0 is the incident solar flux-density (insolation) on the planet, and σ is the Stefan-Boltzmann constant (5.67×10^{-8} $Wm^{-2}K^{-4}$).

Bond albedo can never be greater than 1.0. Enceladus, a moon of Saturn, has a geometric albedo of 1.38 [*Verbiscer et al.,* 2007] and Bond albedo of 0.9 [*Buratti and Veverka*, 1984; *Verbischer and Veverka*, 1994]. For rest of the introduction, Bond albedo will simply be referred to as albedo.

1.2 Cryosphere

The portion of Earth's surface covered by frozen water (e.g. ice caps, glaciers, etc.) is known as cryosphere. In this thesis, I will use the term *cryosphere* to refer to ice or snow present on a planet's surface due to deposition or freezing of any chemical compound or gases, e.g., water, carbon dioxide, methane, and nitrogen. Due to a very high albedo (H_2O

~0.8, CO_2 ~0.97) of pure snow, the cryosphere can play a significant role in driving global climate of any planet. Albedo feedback is also one of the most important positive feedbacks within the Earth's climate system (Chapter 2), which reinforces the importance of cryosphere in a climate system.

1.2.1 Earth

Earth's cryosphere consists of frozen water in various forms, including sea ice, lake ice, river ice, snow cover, glaciers, ice sheets, and frozen ground (which includes permafrost). Earth's permanent ice sheets are presently located on Greenland and Antarctica, with smaller glaciers present elsewhere at high elevations and latitudes. The cryosphere reflects a significant part of incoming solar energy as compared to open water (albedo ~0.07). The cryosphere exchanges heat with warmer areas of the planet, and plays a significant role in the global climate in response to global changes. Being a strong feedback mechanism, albedo feedback can significantly delay or amplify a global seasonal change like melting of glaciers.

1.2.2 Mars

Carbon dioxide ice is abundant on the Martian surface [*Leighton and Murray*, 1966; *Herr and Pimentel*, 1969; *Larson and Fink*, 1972; *Forget*, 1998; *Bibring* et al., 2005], and plays an important role in the planet's energy budget due to its high reflectivity (pure CO_2 snow albedo of ~0.97) and seasonal variation. H_2O ice is also present at the surface of the perennial ice caps, though in lesser abundance than CO_2 ice, and with small seasonal deposition in other parts of the planet [e.g., *Kieffer* et al., 2000; *Bibring* et al., 2004; *Brown* et al., 2014]. Due to the lack of any hydrogen bonding, CO_2 does not exist in liquid phase,

so on Mars the transition occurs between two phases of CO_2, viz. solid and gas, resulting in a large amount of energy exchange during the phase changes.

1.2.3 Other celestial bodies in our solar system

Many other celestial bodies in our solar system have also shown evidence of cryospheric presence on their surface. Moons of Jupiter including Europa, Ganymede, and Callisto; Moons of Saturn including Titan, Hyperion, and Enceladus; and Moons of Uranus including Titania, Umbriel, and Oberon have all shown evidence of water ice (along with ices from other chemical compounds) present on their surface [*Fink et al.,* 1973; *Spencer,* 1987; *Cruikshank*, 1980; *Buratti and Veverka*, 1984; *Verbischer and Veverka*, 1994]. Titan is known to have liquid hydrocarbon lakes, making it the only other body in our solar system with presence of stable liquid at the surface [*Mitri et al.*, 2007; *Stofan et al.*, 2007]. Enceladus has been found to be one of the most geologically dynamic objects in the solar system [*Kargel,* 2006]. Recently, evidence for presence of H_2O, CH_4 and N_2 ice has been found at the surface of Pluto [*Stern et al.*, 2015; *Cruikshank et al.*, 2015; *Trafton*, 2015].

Enceladus, Europa and Titan also show evidence of cryovolcanism [*Kargel,* 2006; *Spencer et al.,* 2009; *Greeley*, 1998; *Quick et al.,* 2013; *Sotin* et al., 2005; *Mitri et al.*, 2007; *Stofan et al.*, 2007]. A cryovolcano is a volcano that erupts volatiles such as water, ammonia or methane, instead of molten rock. The presence of cryosphere and cryovolcanism are reasons for relatively higher surface albedo of these bodies. Although Venus also has a high albedo of ~0.75, it does not have a cryosphere present on its surface. On the contrary, Venus is one of the hottest planets (mean surface temperature of 735 K) in our solar system, caused by the high amount of greenhouse gases in its atmosphere. Venus's high albedo is caused by thick, highly reflective clouds present in the planet's

atmosphere. These clouds are made up of sulfur dioxide, and concentrated sulfuric acid [*Pierrehumbert,* 2010]. Interestingly, the night side of Venus' atmosphere above 100 km is so cold (temperature as low as 100 K) that it was named the 'cryosphere' [*Bertaux et al.,* 2007].

1.3 Climate of Mars

The Martian atmosphere consists primarily of carbon dioxide with small percentages of nitrogen (N_2), argon (Ar), and trace amounts of other gases like oxygen, water vapor, carbon monoxide, and hydrogen. The mass of Mars is about 11% that of Earth, and it has gravitational acceleration about 38% that of Earth's. Therefore Mars has a very thin atmosphere with mean surface pressure of about 6 mbar (about 0.6% of Earth's mean sea level pressure). Mars' thin atmosphere and its greater distance from the sun mean that Mars is much colder than Earth. The average temperature is about -55 °C (218 K), although it can vary from -153 °C (120 K) near the poles during the winter to as much as 20 °C at midday near the equator [*Hess et al.,* 1977]. Actual temperature measurements at the Viking landers' site range from −143 °C (130 K) to 17 °C (290 K) [*Kieffer et al.,* 1977].

The axial tilt of Mars' (25°) is nearly the same as that of Earth (23.5°). Mars therefore experiences similar seasonal amplitudes, except the seasons are roughly twice as long as on Earth. In each hemisphere a polar ice cap forms each fall and winter under an obscuring layer of clouds, reaching its maximum extent at the start of spring. It then recedes with the seasonal warming, shrinking to its residual cap by the end of summer. The orbital eccentricity of Mars' orbit is 0.1, much greater than Earth's present eccentricity of about 0.02. Due to the large eccentricity, winters in the southern hemisphere are long and cold while those in the North are short and relatively warm. The planet receives a lesser amount

of net solar energy than the Earth (Mean Solar constant = 590 W/m^2) due to larger distance from Sun.

Another unique feature of Martian climate is dust storms. Although Mars' atmosphere is thin, it supports weather, clouds, and winds. Giant dust devils routinely lift the oxidized iron dust that covers Martian surface. Dust storm activity can contribute to regional surface albedo changes and the largest of these storms can generate a cloud of dust that can encircle both hemispheres of the planet for more than a Martian season [*Leovy et al.,* 1973; *Cantor,* 2007]. Most of the dust storms' generation can be explained in terms of the classical atmospheric tidal theory developed for the earth's atmosphere [*Zurek and Leovy,* 1981; *Ryan et al.,* 1981]. The radiative heat of sunlight reaching the surface of the planet is fundamentally what drives these dust storms. As sunlight is absorbed by the ground, it warms the air closest to the surface, while the upper air remains cooler. Thus, the Martian atmosphere becomes unstable, with warm air rising and lifting dust with it. Once dust is in the atmosphere, it provides a potent source for heating which have an impact on for vertical and horizontal winds. Rising plumes of warm air create weather systems ranging from small dust devils, similar to those that form in deserts on Earth, to larger continent-sized storms. These larger storms sometimes combine into global storms which cover the entire planet in atmospheric dust [*Leovy et al.,* 1973; *Ryan et al.,* 1981]. Due to higher eccentricity of orbit, these larger storms typically only occur during summer in Mars' southern hemisphere, when radiative heat forces are strongest. Once started, bigger storms can last weeks to months.

1.4 Mars General Circulation Model (GCM)

Mars GCMs have been developed to study the nature of the general circulation of the atmosphere of Mars, how that circulation is driven, and how it affects the climate of Mars in the long term. I use a Mars GCM to determine the surface albedo, and its impact on Martian climate (Chapter 4).

The GCM of the Martian atmosphere developed by the Laboratoire de Météorologie Dynamique (LMD) of the CNRS in Paris in collaboration with the Atmospheric and Oceanic Planetary Physics sub-department in Oxford [*Hourdin et al.*, 1993, 1995; *Forget et al.*, 1998, 1999] is one of the most widely used 3D models of Martian climate by the scientific community. The current model includes the *Non-local thermodynamic equilibrium* (N*LTE*) radiative transfer code [*López-Puertas and López-Valverde*, 1995] valid at up to 120 km altitude, tracer transport, the water cycle with water vapor and ice, the ”double mode” dust transport model (*Madeleine et al.*, 2011), and optional photochemistry and extension into the thermosphere up to 250 km altitude.

The model uses a sigma- P (sigma-pressure) hybrid coordinate which is equivalent to sigma coordinates near the surface, and gradually shifting to purely pressure coordinates with increasing altitude. The distribution of the vertical layers is irregular, to enable greater precision at ground level. The resolution of the model is 64×48 grid cells horizontally, corresponding to 3.758 degrees latitude by 5.6258 degrees longitude. 25 levels are used to represent the atmosphere to a height of 80 km, 32 levels for simulations up to 120 km, or 50 levels to include the thermosphere. The first layer describes the first few meters above the ground, whereas the upper layers span several kilometers.

The radiative transfer equation accounting for the absorption and scattering of solar radiation by dust and other atmospheric constituents is based on the numerical scheme of *Fouquart and Bonel* [1980]. The upward and downward fluxes are obtained from the reflectances and transmittances of the layers, computed using the Delta-Eddington approximation. The available studies of Martian dust optical properties have suggested that the single-scattering properties are characterized by an abrupt change around wavelengths of 0.5 μm, near the peak of the incident solar flux [*Ockert-Bell et al.,* 1997]. The LMD Mars GCM therefore uses two broad bands (0.1-0.5 μm and 0.5-5 μm) to resolve spectral dust properties and represent radiative transfer.

The deposition and sublimation of carbon dioxide on the ground is controlled by relatively simple physical processes. When the surface temperature falls below the condensation temperature, CO_2 condenses, releasing the latent heat required to keep the solid–gas interface at the condensation temperature. Conversely, when CO_2 ice is heated, it partially sublimes to keep its temperature at the frost point temperature. Two kinds of mechanisms which lead to atmospheric condensation are radiative cooling and adiabatic cooling [*Forget et al.,* 1998].

1.5 Organization of the Thesis

In Chapter 2 [*Singh et al.,* 2015], we discuss the quantification of the shortwave Cryosphere Radiative Effect (CrRE) on Earth. This study uses relatively high resolution (0.05°×0.05°) MODIS (Moderate Resolution Imaging Spectroradiometer) data along with radiative kernel datasets as applied by *Perket et al.,* [2014], to derive an estimate of the global land shortwave CrRE. We also perform multiple analyses to determine the sensitivity of our estimates to the use of different thresholds for snow cover determinations,

different climatologies for missing data, and radiative kernels generated with different distributions of clouds produced with various versions of the Community Atmosphere Model (CAM).

In Chapter 3 (*manuscript under review*), we adapt the terrestrial Snow, Ice, and Aerosol Radiation (SNICAR) model to simulate CO_2 snow albedo across the solar spectrum (0.2-5.0 μm). In this study, we apply recent laboratory derived refractive indices of CO_2 ice, which produce higher broadband CO_2 snow albedo (0.93–0.98) than previously estimated. We perform multiple analyses to determine the sensitivity of cryosphere spectral albedo to the amount and type of dust, co-presence of CO_2 and H_2O ices, ice grain size, snow layer thickness, and solar zenith angle. In addition, we also compare our simulations with observed Mars surface albedo.

Finally, in Chapter 4 we describe the integration of SNICAR into the LMD Mars GCM to compute real time albedo in the model. We then explore the impact of dust on surface cryosphere albedo and its impact on Mars' energy budget. Chapter 5 summarizes the key results, and also discusses the relevant research directions for future work.

Chapter 2

The Global Land Shortwave Cryosphere Radiative Effect during the MODIS era

As appears in:
Singh, D., M. G. Flanner, and J. Perket, (2015), *The global land shortwave cryosphere radiative effect during the MODIS era*, The Cryosphere, 9, 2057-2070, doi:10.5194/tc-9-2057-2015.

2.1 Introduction

Snow- and ice-covered surfaces are the most reflective regions on Earth, and their extent can change substantially with small changes in climate. The presence of Earth's cryosphere greatly alters the planet's albedo and changes in cryospheric extent and reflectivity therefore partially determine the sensitivity of climate to anthropogenic and external forcings. After water-vapor and cloud feedback, the albedo feedback is the third most powerful positive feedback mechanisms operating within the current climate system [e.g., *Bony et al.,* 2006; *Winton*, 2006; *Randall et al.*, 2007; *Soden et al.*, 2008; *Shell et al.*, 2008; *Flato et al.,* 2013].

Earth's Cryosphere has shown compelling indications of climate change during recent decades, including mass loss from ice sheets and glaciers [e.g., *Rignot et al.*, 2011, *Gardner et al.,* 2013], rapid ablation of autumn Arctic sea-ice [e.g., *Serreze et al.*, 2007; *Stroeve et*

al, 2012], and reduced seasonal snow coverage [e.g., *Dery and Brown,* 2007; *Brown and Robinson,* 2011]. The Arctic is one of the most sensitive regions on Earth to global climate change [*Manabe et al.,* 1992; *Manabe and Stouffer* 1994; *Miller and Russell* 2000; *Meehl and Washington* 1990]. Several recent studies [e.g., *Chapman and Walsh,* 2007, *Monaghan et al.,* 2008, *Steig et al.,* 2009] have shown that climate is also warming over west Antarctica, and is related to Pacific Ocean warming [*Ding et al.,* 2011] and circumpolar winds.

The shortwave Cryosphere Radiative Effect (CrRE) is the instantaneous influence of snow- and ice-cover on Earth's top of atmosphere (TOA) solar energy budget [*Flanner et al.*, 2011; *Hudson*, 2011; *Perket et al.*, 2014]. CrRE depends not only on snow and sea-ice coverage, but also on local insolation, cloud cover, and properties of the snow, ice and their underlying surface that determine reflectance. These features determine the impacts of cryospheric presence on net TOA solar flux [e.g., *Winton*, 2006; *Qu and Hall,* 2005]. Changes in the extent of seasonal snow cover and sea-ice can drive large changes in CrRE on sub-decadal timescales, whereas the areal coverage of ice sheets and glaciers tend to evolve on much longer timescales. The presence of the cryosphere also perturbs Earth's longwave energy budget, e.g., through changes in emissivity and surface temperature resulting from the insulating effect of snow and the change in surface elevation induced by ice sheets. This study, however, concentrates exclusively on the shortwave component of CrRE (hereafter referred to simply as CrRE).

Our work focuses on developing a global, gridded, time-resolved dataset of the land-based CrRE, using modern remote sensing observation of surface albedo and snow presence; combined with radiative kernels that provide TOA radiative impacts. *Flanner et*

al [2011] derived a 30-year record of the northern hemisphere CrRE from coarse-resolution determinations of snow cover extent. Here we apply higher-resolution, higher quality remote sensing data from the MODerate-resolution Imaging Spectroradiometer (MODIS) to derive global land-based CrRE over 2001-2013, helping inform on the utility of the longer-term record derived by *Flanner et al* [2011], and broadening the scope of these estimates to include the southern hemisphere. We generate CrRE for both all-sky and clear-sky conditions to help assess the masking effect of clouds and atmospheric aerosols. We provide statistics including global, hemispheric, glaciated and non-glaciated land CrRE averages. We also perform multiple analyses to determine the sensitivity of our estimates to the use of different thresholds for snow cover determinations, different climatologies for missing data, and radiative kernels generated with different distributions of clouds. These sensitivity analyses help us identify the sources of uncertainty that have relatively high impact on CrRE. In this paper, we focus only on land based CrRE, and refer readers to other recent estimates of CrRE from Arctic sea-ice [*Pistone et al.*, 2014; *Cao et al.*, 2015].

2.2 Methods

2.2.1 Satellite Dataset Used

MODIS MCD43C3 collection 5 surface albedo data [e.g., *Schaaf et al.*, 2002] and accompanying snow coverage statistic (both provided at spatial resolution 0.05°×0.05°) are the primary input datasets we use to generate land based CrRE (LCrRE) at 16-day resolution. The snow presence parameter (0-100%) is a measure of the fraction of native measurements within each 16-day period and each 0.05° pixel in which the presence of snow is detected. We assume any pixel with snow coverage greater than zero has a surface albedo that was affected by the presence of snow. We apply data with quality flag 4 and

better to maximize the spatial and temporal coverage of albedo measurements. Missing data in this collection arise from cloud cover and absence of sunlight at high latitudes during winter. To derive a spatially and temporally continuous LCrRE record, we also apply snow-cover information from the Near-real-time Ice and Snow Extent (NISE) dataset [*Nolin et al.,* 1998], as described in the next subsection. NISE provides daily binary snow-cover at 25 km Equal-Area Scalable Earth Grid (EASE-grid) spatial resolution, projected on a polar stereographic grid. Because it is determined from microwave remote sensing observations, it offers estimates of snow presence under all conditions, including environments with clouds and low illumination. Since these datasets have different spatial resolutions, the NISE dataset has been remapped to the higher resolution MODIS grid prior to analysis.

We use global gridded estimates of snow-free albedo derived from MODIS [*Moody et al.*, 2008], also provided at 16-day and 0.05 degree resolution, as a baseline for determining the surface albedo contrast induced by snow. These data are climatological 16-day averages derived from 2000-2004 MODIS measurements.

2.2.2 Global Albedo Climatology for filling missing data

A 16-day global surface-albedo climatology with spatial resolution of 0.05°×0.05° is generated to fill any missing MODIS data-points, using the following steps:

Step 1: For each pixel and each 16-day period of the year, we take the average albedo over all the years (2001-2013) of MODIS data during periods with valid measurements and non-zero snow cover. Since this is a seasonally-varying gridded

climatology, it is primarily used to replace albedo of missing MODIS data in situations deemed to be snow-covered in the NISE dataset.

Step 2: We take the annual mean of the albedo values generated from the previous step for each snow-covered unfilled pixel in step 1. We only apply this average at locations and times when the climatology from step 1 does not provide valid data (e.g., at pixels and 16-day intervals that had substantial cloud cover during each of the 13 years of MODIS observations).

Step 3: Albedo values generated from the previous two steps are averaged spatially over all pixels within each land classification type defined in the MODIS MCD12C1 product using IGBP (Type 1) land cover classification. This procedure produces an annual-mean snow-covered albedo climatology by land classification (listed in Table A.1), and is used to fill any remaining missing pixels unfilled by steps 1 and 2.

MCD12C1 provides the global dominant land cover types at 0.05°×0.05° spatial resolution. It is continuous and therefore completely eliminates the chance of having any missing pixels after applying step 3.

Although the snow-free surface albedo dataset is continuous, it is undefined in regions with large solar zenith angle or near-permanent snow cover. To define snow-free albedo in these regions, we apply annual averages of the snow-free albedo values for each pixel (similar to method applied in step 2).

The ice-free surface albedo for permanent glaciated areas (e.g. Greenland, Antarctica) is assumed to be 0.26, an average value of snow-free albedo over barren land

(*Flanner et al.*, 2011). This assumption enables a rough estimate of the TOA impact associated with presence of the full ice sheets. While our estimates of absolute LCrRE in these regions are therefore subject to ambiguities (such as the type of vegetation that would thrive without the ice sheet), seasonal and inter-annual changes in glacier surface albedo, e.g., as caused by altered insolation, melt extent, and snow metamorphic state, drive changes in LCrRE that are unaffected by this assumption, since the ice-free albedo is assumed to be static.

Considering the current bed topography removal of the West Antarctic Ice Sheet would expose open-ocean (albedo 0.07). Although, we still use barren land albedo because of several other uncertain effects that would occur in the event of total ice sheet ablation, e.g., isostatic rebound of land, sea-level rise, encroachment of vegetation over open land. Our objective is to quantify the instantaneous LCrRE and quantifying all the aforementioned uncertainties in this study are beyond the scope of this paper. We also note that the MODIS land mask applied in our study excludes ice shelves.

2.2.3 Methodology

Our interest lies in the change in solar energy reflected because of snow, and we therefore assume that measured albedo increase in the presence of snow, relative to the snow free state, is caused entirely by snow. *Flanner et al* [2011] employed a definition of CrRE that utilizes snow cover fraction, in order to facilitate the use of snow extent data without coincident albedo measurements from several decades ago. Here we utilize a simpler definition that omits snow cover fraction, since we have direct measurements of surface albedo from MODIS. Using this approach, the mathematical framework to

describe CrRE at time *t* within a region *R* that is composed of *N* partially snow- or ice-covered grid-cells *i* is:

$$CrRE(t,R) = \frac{1}{A(R)} \sum_{i=1}^{N} Max\left[\left(\alpha(t,i) - \alpha_{snow-free}(t,i)\right),\ 0\right] \frac{\partial F}{\partial \alpha}(t,i) A(i)$$

(2.1)

where A is area, $\alpha - \alpha_{\text{snow-free}}$ is the albedo contrast ($\Delta\alpha$), and $\partial F/\partial \alpha$ is the change in TOA net solar energy flux with changing surface albedo. The 'Max' function is used to avoid any negative albedo contrast values. We determine $\partial F/\partial \alpha$ using radiative kernels that provide the instantaneous effect on TOA energy budget associated with small perturbations in surface albedo [e.g., *Shell et al.,* 2008]. This equation is only applied to gridcells where snow presence has been detected, and LCrRE is otherwise assumed to be zero.

We created kernel datasets using the general framework of *Perket et al.*, [2014], using the Community Atmosphere Model versions 4 and 5 (CAM4 and CAM5). TOA energy fluxes were calculated with and without surface albedo perturbations every model time-step for one year of simulation, and flux differences were then averaged into monthly resolved kernels. We also apply radiative kernels generated previously with the CAM3 model [*Shell et al.,* 2008] and Geophysical Fluid Dynamics Laboratory Atmosphere Model (AM2) [*Soden et al.,* 2008].

A graphical representation of the basic algorithm used in our analysis is shown in Figure 2.1, and can be summarized as follows:

a) We first check for the presence of snow in a particular pixel using MODIS data. If snow was present at any time during the 16-day retrieval (snow flag >0) then the difference between actual (16-day) surface albedo and snow-free albedo is taken as the albedo contrast.

b) If MODIS data were missing then presence of snow is checked using NISE data. If snow is present during some or all of the 16-day period, then albedo contrast is determined by taking the difference between climatological snow-covered albedo for that gridcell (and time of year, as described in the previous subsection) and snow-free albedo. Since the NISE dataset is continuous and daily-resolved, we are able to determine those situations when a particular pixel was covered with snow for only a portion of the 16-day period of MODIS measurements. In those cases, if a pixel is covered with snow for D days out of 16, then the albedo contrast is multiplied with a scaling factor of $D/16$.

c) If MODIS determines a pixel is not snow-covered (snow flag = 0) or in the absence of MODIS data if NISE does not indicate any snow ($D = 0$), then albedo contrast and LCrRE are set to zero for that pixel.

d) After determining the albedo contrast, this term is multiplied with the various radiative kernels to derive different estimates of all-sky and clear-sky LCrRE. Except as noted in sensitivity studies described later, subsequent LCrRE results are derived from the CAM4 radiative kernel,

which simulates an intermediate level of cloud masking compared with the other kernels.

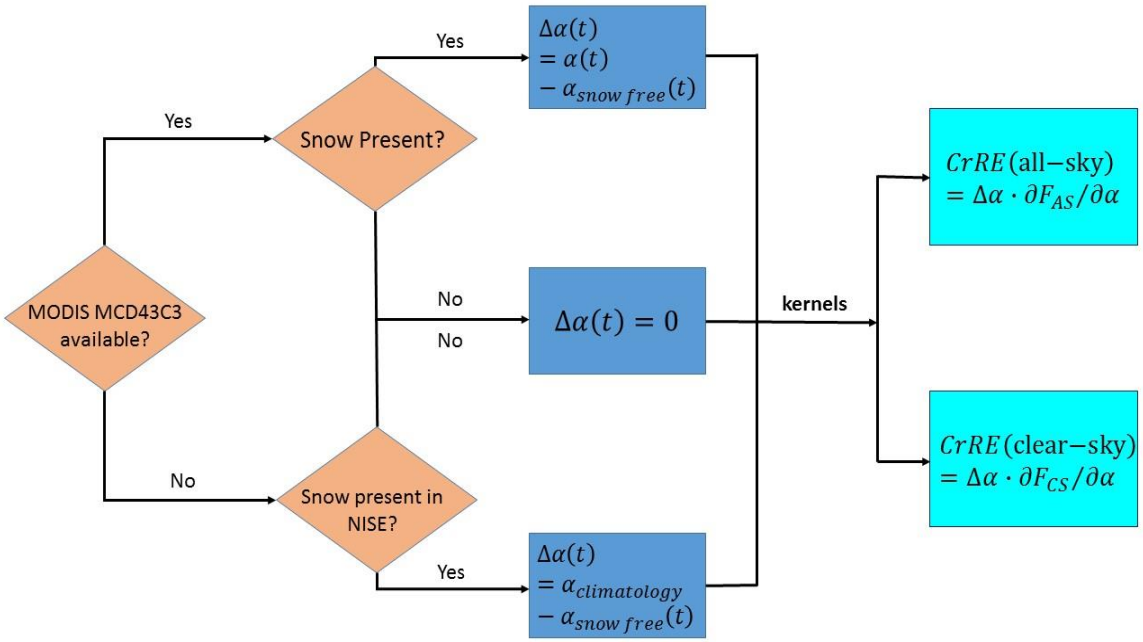

Figure 2.1: Algorithm for calculating CrRE

2.3 Results and Discussion

2.3.1 Spatial and Seasonal Variability of the Mean Climate State

All-sky global annual-mean LCrRE during 2001-2013 calculated using the CAM4 kernel is -2.58 Wm^{-2}, and ranges from -2.16 to -2.96 Wm^{-2} with application of different radiative kernels. Table 2.1a shows LCrRE averages over different domains and calculated with different radiative kernels. Permanent glaciated regions (e.g., Greenland and Antarctica) contribute about two-thirds of the net global LCrRE, due to their persistently high albedo around the year. For this discussion, land classified as snow or ice in the MODIS MCD12C1 land type dataset (Appendix A) is considered as permanently glaciated.

Due to the size of the Antarctic Ice Sheet, the Southern Hemisphere contributes about 60% of the global LCrRE. On the other hand, non-glaciated regions in Northern Hemisphere contribute about 32% of the global LCrRE. Because the areal extent of seasonal snow has little "memory" beyond a year, non-glaciated component of the LCrRE can respond rapidly to climate change and drive albedo feedback on sub-decadal timescales. Impact of non-glaciated region in Southern Hemisphere is negligible because of less land presence at mid and high latitudes (Figure 2.2), contributing only about 0.08% of the global LCrRE. In the Northern Hemisphere, non-glaciated regions contribute about 3.7 times more to LCrRE than glaciated areas. LCrRE associated with permanent glacier cover in mountain regions (e.g., the Himalaya) is also clearly visible, even though they are situated at much lower latitudes (Figure 2.2). Table 2.1 (b) and 2.1 (c) shows percentage contribution of different domains and separate land masses to the global LCrRE respectively.

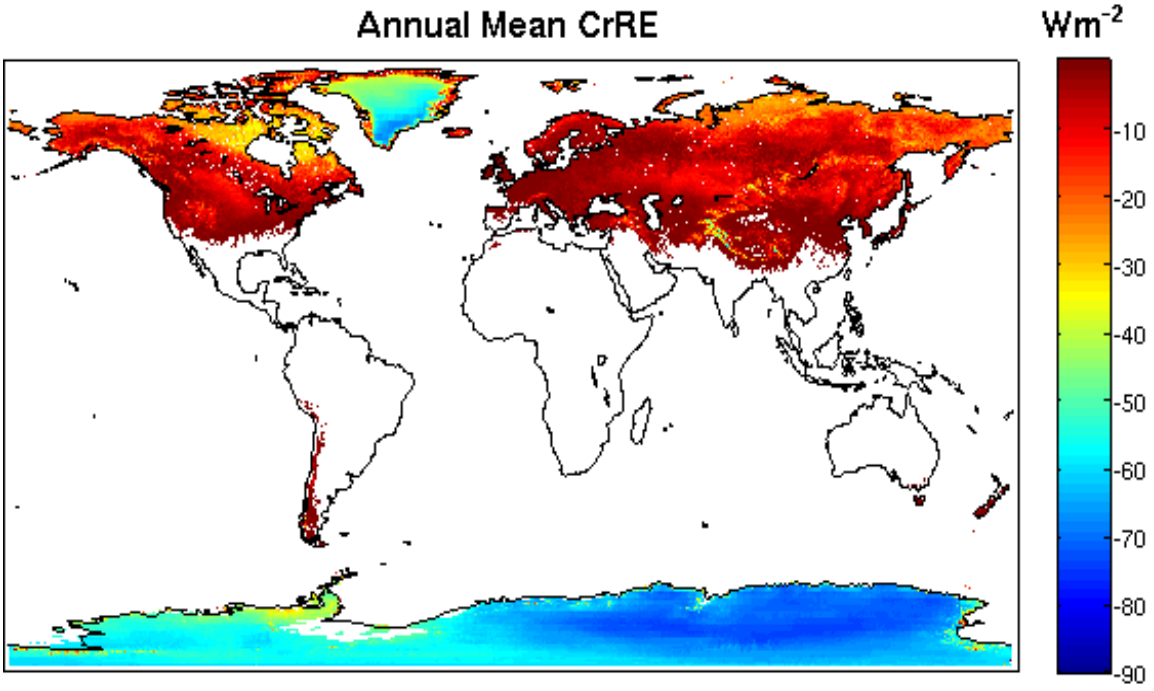

Figure 2.2: Map showing annual-mean all-sky land CrRE, averaged over 2001-2013, derived with the CAM4 kernel.

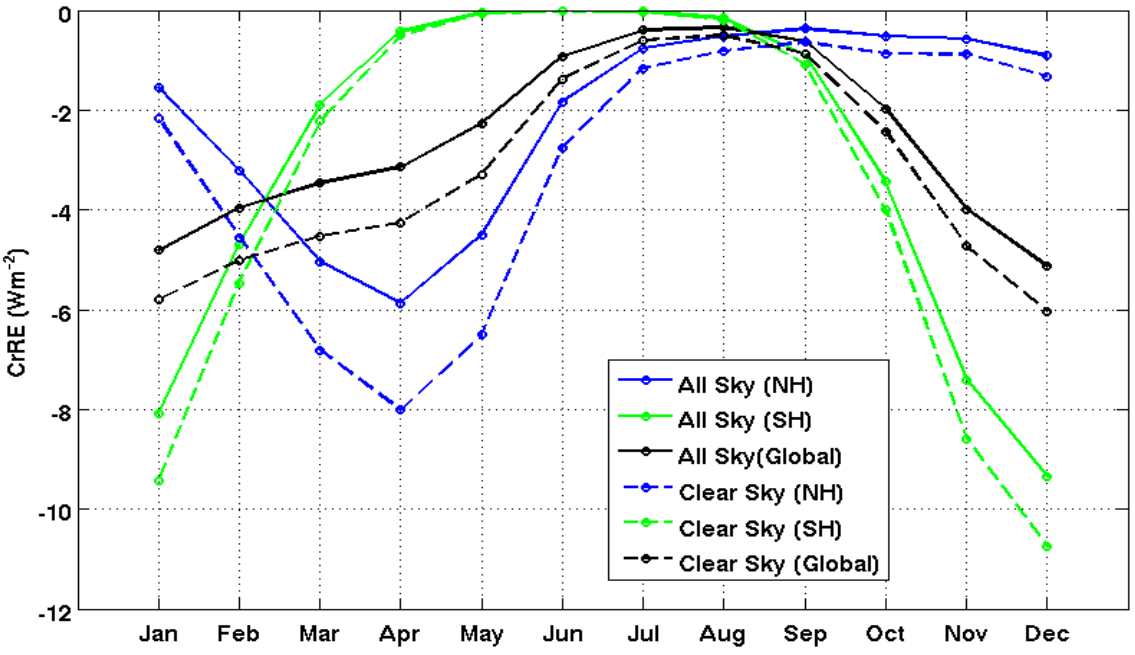

Figure 2.3: Annual cycle of hemispheric and global LCrRE for both all-sky and clear-sky conditions, derived from the CAM4 radiative kernels.

Table 2.1: ***(a)*** *All-sky (clear-sky) cryosphere radiative effect averaged over different domains and derived with various radiative kernels (Wm^{-2}).* ***(b)*** *Percentage contribution of different domains to the global LCrRE using CAM4 kernels.* ***(c)*** *Percentage contribution of different land masses to the global LCrRE using CAM4 kernels.*

(a)		CAM4 kernel	CAM5 kernel	CAM3 kernel	AM2 kernel
Northern Hemisphere	Glaciated	-0.45 (-0.62)	-0.56 (-0.63)	-0.36 (-0.61)	-0.45 (-0.60)
	Non-Glaciated	-1.67 (-2.4)	-1.95 (-2.48)	-1.16 (-2.42)	-1.40 (-2.24)
Southern Hemisphere	Glaciated	-3.08 (-3.58)	-3.41 (-3.61)	-2.79 (-3.58)	-3.16 (-3.59)
	Non-Glaciated	-0.004 (-0.007)	-0.005 (-0.008)	-0.003 (-0.007)	-0.004 (-0.007)
Global	Glaciated	-1.77 (-2.1)	-1.99 (-2.12)	-1.58 (-2.09)	-1.81 (-2.09)
	Non-Glaciated	-0.84 (-1.2)	-0.98 (-1.25)	-0.58 (-1.21)	-0.70 (-1.12)
Global	Global	-2.58 (-3.28)	-2.96 (-3.37)	-2.16 (-3.31)	-2.51 (-3.22)

(b)		% Contribution
Northern Hemisphere	Glaciated	8.7 (9.5)
	Non-Glaciated	32.4 (36.6)
Southern Hemisphere	Glaciated	59.7 (54.6)
	Non-Glaciated	0.08 (0.1)
Global	Glaciated	68 (64)
	Non-Glaciated	32 (36)
Global	Global	100 (100)

(c) Land Mass	LCrRE	% Contribution
Antarctica	-1.51 (-1.76)	58.6 (53.6)
Europe+Asia	-0.55 (-0.79)	21.1 (23.94)
North America	-0.34 (-0.49)	13.02 (14.83)
Greenland	-0.19 (-0.25)	7.2 (7.5)
South America	-0.0024 (-0.0043)	0.09 (0.13)
Australia	-2.28E-04 (-4.37E-04)	~0
Africa	-5.59E-05 (-6.2E-05)	~0
Global	-2.58 (-3.28)	100 (100)

Clear-sky LCrRE values are expectedly higher than all-sky LCrRE values because of the absence of cloud scattering. Similarly, all-sky LCrRE derived from the CAM5 kernel is higher than that derived from the CAM4 kernel because cloud masking is substantially less in CAM5, due to the prevalence of thinner clouds (*Kay et al.*, 2012, *Perket et al.*, 2014). AM2 and CAM4 values are similar, indicating a similar degree of cloud masking in these two kernels, whereas the CAM3 kernel provides substantially greater attenuation of surface albedo anomalies at the TOA (*Flanner et al.*, 2011). *Cao et al.*, (2015) determined that the CAM3 and AM2 radiative kernels likely mask too much of the Arctic sea-ice radiative effect, but it is unclear if these kernel biases exist over land and have persisted in the more modern CAM4 and CAM5 models.

Figure 2.3 shows global and hemispheric monthly variations of LCrRE for both all-sky and clear-sky conditions. Seasonal variations are apparent in both hemispheres. LCrRE values peak (become most negative) during April in the Northern Hemisphere, about 2 months before the peak boreal solstice insolation. On the other hand, Southern Hemisphere LCrRE peaks in December, during maximum austral insolation. These differences occur because the Northern Hemisphere LCrRE is dominated by seasonal snow, while Southern Hemisphere LCrRE is dominated by permanent glaciated Antarctica, and thus the seasonal cycle of LCrRE is determined more directly by insolation in the Southern Hemisphere. Spatial distributions of tri-monthly seasonal averages of LCrRE are shown in Figure 2.4, indicating the same insolation-modulated tendencies over glaciated terrain described earlier. The timing of peak LCrRE in regions with seasonal snow, however, depends on the timing of melt onset, which almost always precedes the peak insolation period.

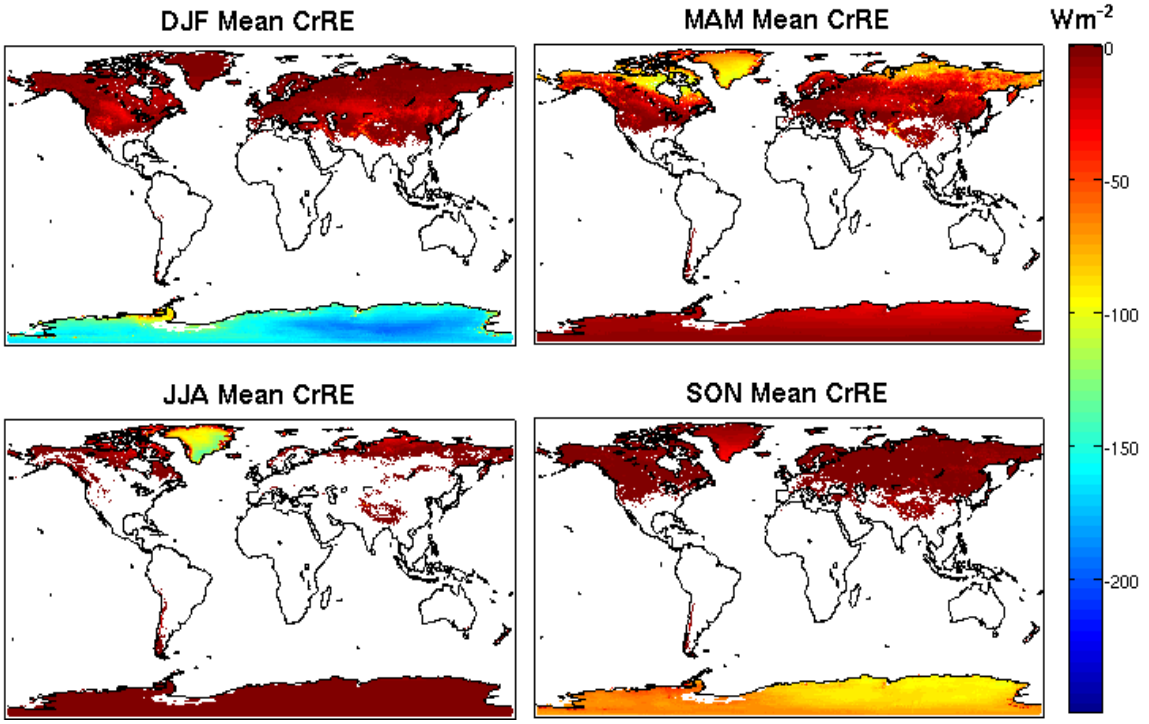

Figure 2.4: Tri-monthly seasonally averaged LCrRE derived with the CAM4 all-sky kernel. (DJF – December, January, February; MAM – March, April, May; JJA – June, July, August; SON – September, October, November).

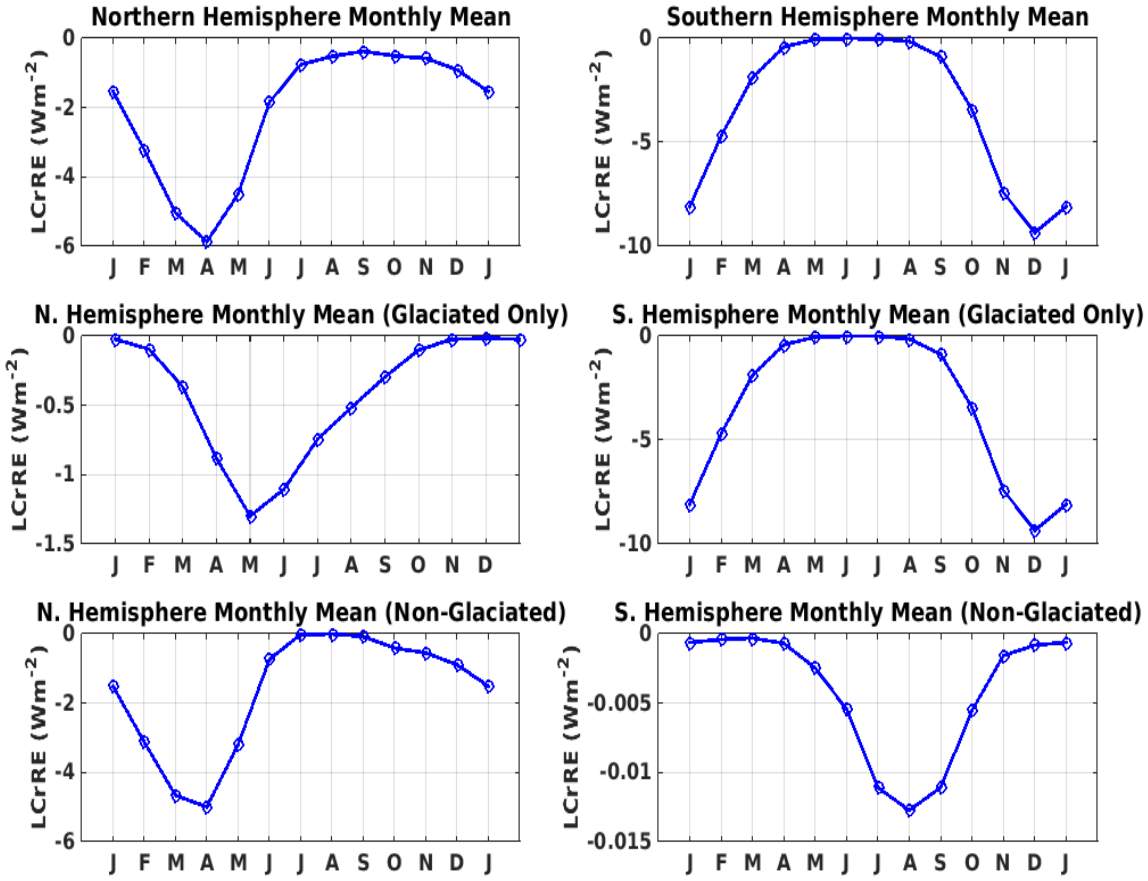

Figure 2.5: All-sky LCrRE averaged over the Northern (left) and Southern (right) Hemisphere, shown as contributions from all land within the hemisphere (top), permanently glaciated areas only (middle), and non-glaciated areas only (bottom). Data were derived with the CAM4 radiative kernel.

Peak LCrRE over glaciated regions of the Northern Hemisphere occurs in May, lagging the peak over non-glaciated regions by about one month (Figure 2.5). Glaciated LCrRE in the Northern Hemisphere peaks before the summer solstice because Greenland surface albedo decreases between May and the end of June as summer melt commences. This tendency is not apparent over Antarctica because a smaller portion of the Antarctic Ice Sheet experiences surface melt during summer. Also the LCrRE change is more gradual for glaciated than non-glaciated regions during both melting and freezing seasons. As the temperature rises, temporary snow over non-glaciated land ablates relatively quickly. This causes a rapid decrease in surface albedo and hence lowering of the albedo contrast. Similar observations cannot be made for Southern Hemisphere due to negligible LCrRE contribution from non-glaciated region. Global LCrRE values show less seasonal variation than the hemispheric averages because they are basically averages of two hemispheric seasonal cycles that are somewhat out of phase with each other. Nonetheless, global LCrRE does exhibit a minimum during July and August, when there is little seasonal snow cover in the Northern Hemisphere and Antarctica receives little insolation.

We observe a contribution of about -0.037 Wm^{-2} (1.43% of the global total) from high mountainous regions (Himalayas, Andes, etc.) towards global LCrRE. The Himalayan region alone contributes about 93.8% of the total mountainous region LCrRE. (Here, we define the high mountainous contribution to LCrRE as that coming from permanent glaciated areas between latitudes of 60°S and 60°N.) The contribution from these high-altitude areas is relatively smaller but consistent throughout the year. Our use of 0.05 degree resolution data allows us to determine LCrRE over many regions with patchy snow extent, though mountain snow cover varies substantially on even smaller spatial scales.

Figure 2.6 shows LCrRE contribution of the Andes and the Himalayas averaged over the MODIS era.

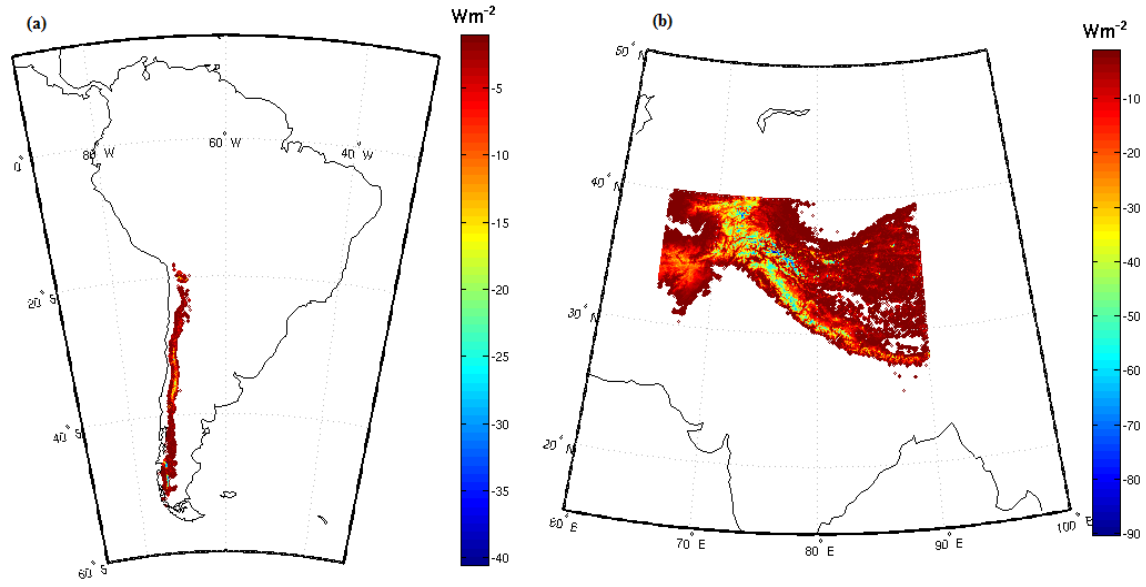

Figure 2.6: Maps showing all-sky LCrRE, averaged over 2001-2013 over (a) Andes and (b) Himalayan mountain ranges.

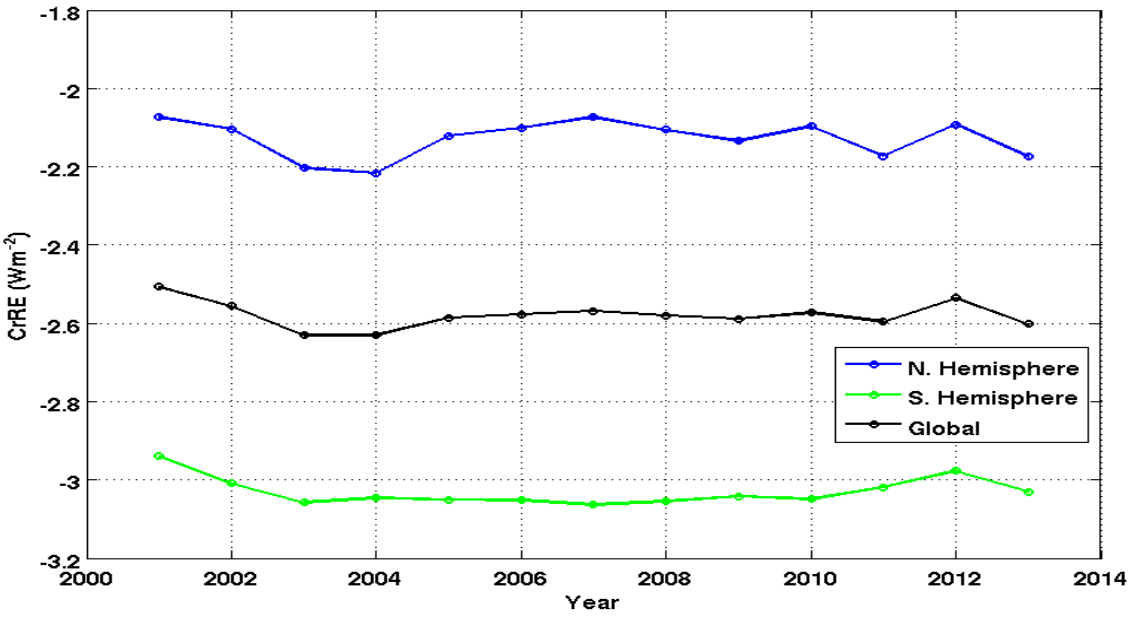

Figure 2.7: Annual mean land LCrRE time series during 2001-2013 for the globe and each hemisphere.

2.3.2 Sensitivity Analysis

A sensitivity analysis of LCrRE has been done to estimate its dependence on various parameters included in the algorithm (Table 2.2). In this part of the study, CAM4 kernels are used and other parameters are varied. The first column represents the LCrRE values from the default case using the algorithm discussed in section 2.3 (Figure 2.1). The second column lists LCrRE values generated using only the NISE snow flag (i.e., snow presence is determined exclusively with NISE measurements, rather than MODIS). Differences between these estimates are due to the different remote sensing techniques applied to determine snow presence and different spatial and temporal resolutions of the NISE and MODIS datasets.

The third and fourth columns are similar to first and second columns, respectively, but apply the land class climatology of albedo contrast instead of spatially- and temporally-varying albedo contrast (section 2.2.2). The derivation of these land class climatology values is described in step 3 of section 2.2.2. A list of mean albedo values and standard deviations for the different land classes is provided in Appendix A. In these cases land class climatology albedo values have been used irrespective of data availability in MODIS, in combination with snow presence determined from MODIS+NISE (column 3) and exclusively from NISE (column 4). This sensitivity study is designed to assess the utility of using much simpler estimates of snow-covered albedo than our more involved space- and time-dependent estimates.

LCrRE values in the second, third and fourth columns (Table 2.2) are very similar to each other. In all three cases the estimated LCrRE is lower than the original analysis

(column 1). This indicates the dependence of LCrRE on MODIS snow flag and global albedo climatology, and changing either of those drops the LCrRE estimates by about 8% globally. Also when land class climatological albedos are used, LCrRE is very similar for different choice of snow flags. This may be due to the fact that the land class climatology only depends on land class type and does not vary with time.

MODIS MCD43C3 albedo data are accompanied by quality flags, indicating the fraction of input measurements to each 16-day data point that were made under cloud-free conditions with sufficiently small solar zenith angle [e.g., *Schaaf et al,* 2002]. Table 2.3 shows a comparative study of LCrRE determined without quality flag filtering (i.e., quality flag 4 and better), and determined using only quality flag 2 or better albedo data. Quality flag 2 is mixed, with 75% or less of the underlying data derived from inverting reflectance for the BRDF retrievals, and 25% or less of the underlying data filled. Using better albedo data (lower quality flag) does not make a significant difference in our determination of global LCrRE. This indicates that the fill values applied in the MCD43C3 retrieval algorithm are similar to our developed climatology (section 2.2.2).

2.3.3 Inter-annual trends

Annual global LCrRE averages do not show significant inter-annual trends during the MODIS era (Figure 2.7), perhaps partially due to the relatively short duration of this period. Slopes for global, northern hemisphere and southern hemisphere LCrRE are -2×10^{-3} $Wm^{-2}yr^{-1}$, -1.3×10^{-3} $Wm^{-2}yr^{-1}$ and 7.3×10^{-4} $Wm^{-2}yr^{-1}$, respectively. These trends are not significant at the 95% confidence level.

To better understand the LCrRE trend, pixel-by-pixel trend maps have been generated using the Mann-Kendall regression technique with 95% significance level (Figure 2.8). A strong positive trend (indicating less negative LCrRE) is observed over some regions of the Northern Hemisphere, especially over Northern Asia during the spring season (Figure 2.8b). Positive trends over seasonally snow covered areas are most likely due to a decrease in snow coverage [e.g., *Qu and Hall,* 2007; *Vaughan et al.,* 2013], and the trend in LCrRE that we find over Northern Asia is consistent with studies showing recent declines in snow cover over this region [e.g., *Dery and Brown*, 2007; *Brown and Robinson,* 2011; *Derksen et al.,* 2014]. Possible reasons for the positive trends seen over Greenland include: 1) increased snow metamorphism and black carbon deposition [e.g., *Box et al,* 2012; *Keegan et al., 2014*], 2) transport and deposition of dust and other light-absorbing impurities over the ice-sheets due to increased dust source areas associated with increased snow-free area [*Dumont et al.,* 2014], 3) higher melt extent across the Greenland ice sheet expose more fresh water at the surface (*Tedesco et al.,* 2014) and 4) MODIS sensor degradation on the Terra satellite during recent years [*Sun et al.,* 2014*; Lyapustin et al.,* 2014], which would indicate a spurious decline in albedo.

We also observe slightly negative LCrRE trends over Antarctica, which may be due to increases in snowfall that have decreased the duration that surface snow has to "age", thereby increasing surface albedo [*Picard et al.,* 2012]. Interestingly, LCrRE has also become more negative over some regions of Central Asia, presumably due to increased temporal coverage of snow.

Table 2.2: All-sky (Clear-Sky) CrRE (Wm-2) derived with different algorithms. All cases apply the CAM4 radiative kernels.

		Both flags with original climatology	**Only NISE flag with original climatology**	**Both flags with land class climatology**	**Only NISE flag with land class climatology**
Northern Hemisphere	Glaciated	-0.45 (-0.62)	-0.37 (-0.51)	-0.39 (-0.54)	-0.38 (-0.51)
	Non-Glaciated	-1.67 (-2.4)	-1.4 (-2.0)	-1.41 (-2.05)	-1.47 (-2.1)
Southern Hemisphere	Glaciated	-3.08 (-3.58)	-3.03 (-3.51)	-2.91 (-3.38)	-2.91 (-3.38)
	Non-Glaciated	-0.004 (-0.007)	-0.004 (-0.006)	-0.005 (-0.008)	-0.008 (-0.012)
Global	Glaciated	-1.77 (-2.1)	-1.7 (-2.0)	-1.65 (-1.96)	-1.65 (-1.95)
	Non-Glaciated	-0.84 (-1.2)	-0.7 (-1.0)	-0.71 (-1.03)	-0.74 (-1.05)
Global	Global	-2.58 (-3.28)	-2.4 (-3.01)	-2.36 (-2.99)	-2.38 (-3.0)

Table 2.3: All-sky (Clear-Sky) CrRE (Wm-2) with different quality flag filters, derived using CAM4 kernels in all cases.

		Quality flag 4 or better	**Quality flag 2 or better**
Northern Hemisphere	Glaciated	-0.45 (-0.62)	-0.43 (-0.59)
	Non-Glaciated	-1.67 (-2.4)	-1.6 (-2.29)
Southern Hemisphere	Glaciated	-3.08 (-3.58)	-3.07 (-3.57)
	Non-Glaciated	-0.004 (-0.007)	-0.004 (-0.006)
Global	Glaciated	-1.77 (-2.1)	-1.75 (-2.08)
	Non-Glaciated	-0.84 (-1.2)	-0.8 (-1.15)
Global	Global	-2.58 (-3.28)	-2.55 (-3.23)

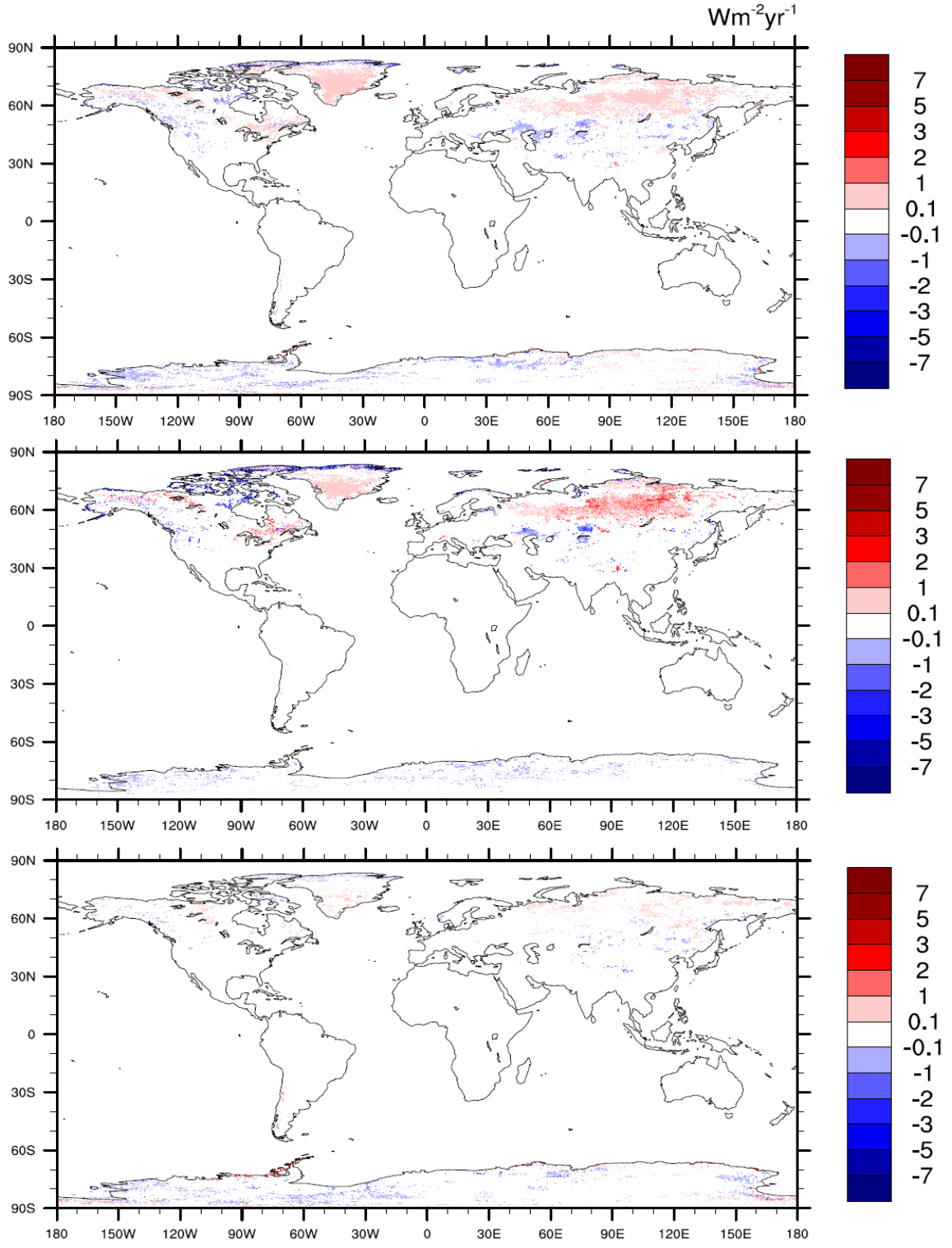

Figure 2.8: LCrRE trend maps for annual (Top), MAM (Middle) and SON (Bottom) seasons (MAM – March, April, May; SON – September, October, November). Trends were derived using Mann-Kendall regression technique. Only regions with significant trends (p=0.05) are shown in the map.

2.3.4 Comparison with previous study

The current study and that of *Flanner et al.,* [2011] have a common overlap period of 2001-2008. To compare the derivations of LCrRE between these two studies, we re-derived Northern Hemisphere LCrRE during 2001-2008 using the CAM3 radiative kernel and an assumption of ice-free albedo over Greenland of 0.316, as in *Flanner et al.* [2011]. For this overlap period, and using these assumptions, the current study gives a LCrRE value of about -1.41 Wm^{-2} over the northern hemisphere as compared to -1.72 Wm^{-2} from *Flanner et al.,* [2011], who determined snow presence during 1979-2008 from coarse-resolution AVHRR data [e.g., *Robinson et al,* 2000]. (The 1979-2008 mean northern hemisphere LCrRE found by *Flanner et al,* [2011] was -2.0 W/m^2, indicating less boreal cryospheric influence during 2001-2008 compared with 1979-2001). To understand this difference, an LCrRE difference map between the current study and *Flanner et al.,* (2011) has been generated (Figure 2.9). This difference was taken between annual mean LCrRE values over the common overlap period. We find that the use of coarse-resolution snow cover data [*Flanner et al,* 2011] likely leads to overestimation of LCrRE along the continental edges and in mountainous regions like the Himalayas. Some of the differences along the continental edges (especially of Greenland), depicted in Figure 2.9 at 1 degree resolution, are likely due to poor resolution of land cover fraction in the AVHRR snow cover data used by *Flanner et al* [2011], and possibly also the influence of land-fast sea-ice. Snow in mountainous regions is difficult to resolve in any model because of irregular topography, and is uncertain in both datasets. The annual mean LCrRE time-series (Figure 2.10) of both datasets show similar patterns and exhibit a correlation coefficient of 0.78, lending confidence in the application of longer-term AVHRR data to derive estimates of large-

scale LCrRE trends. We expect that the current analysis will be useful in determining correction algorithms for biases in the Himalayas and along the coastal margins of Greenland that may result from use of coarse-resolution AVHRR data.

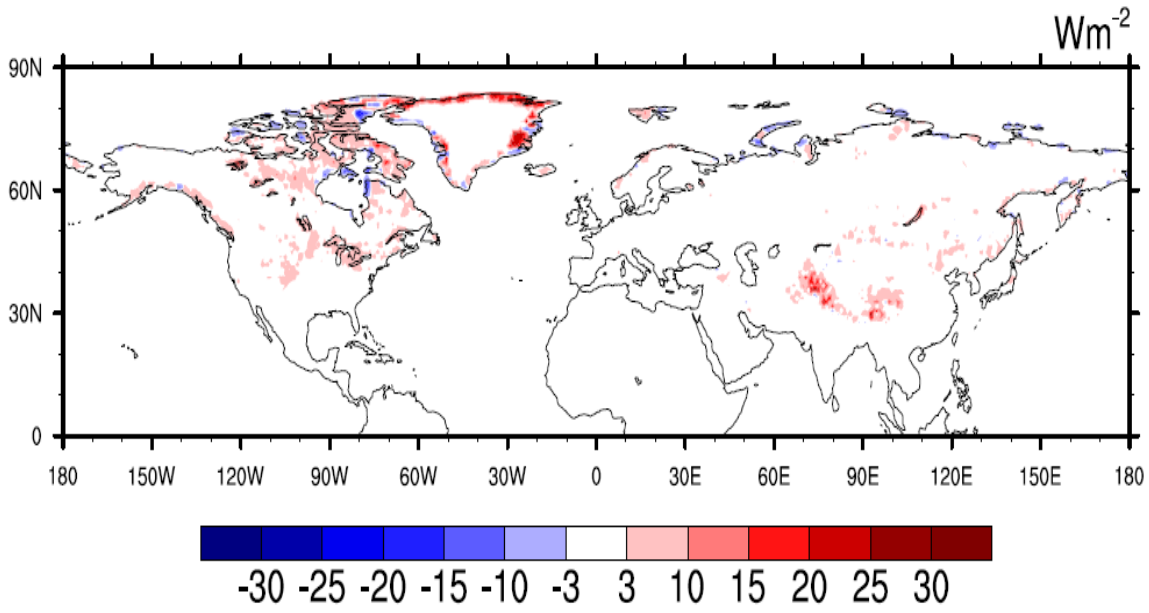

Figure 2.9: Difference of 2001-2008 mean LCrRE between the current study and Flanner et al., (2011) using CAM3 kernels. Areas of red indicate a stronger (more negative) LCrRE determined by Flanner et al [2011] than determined here.

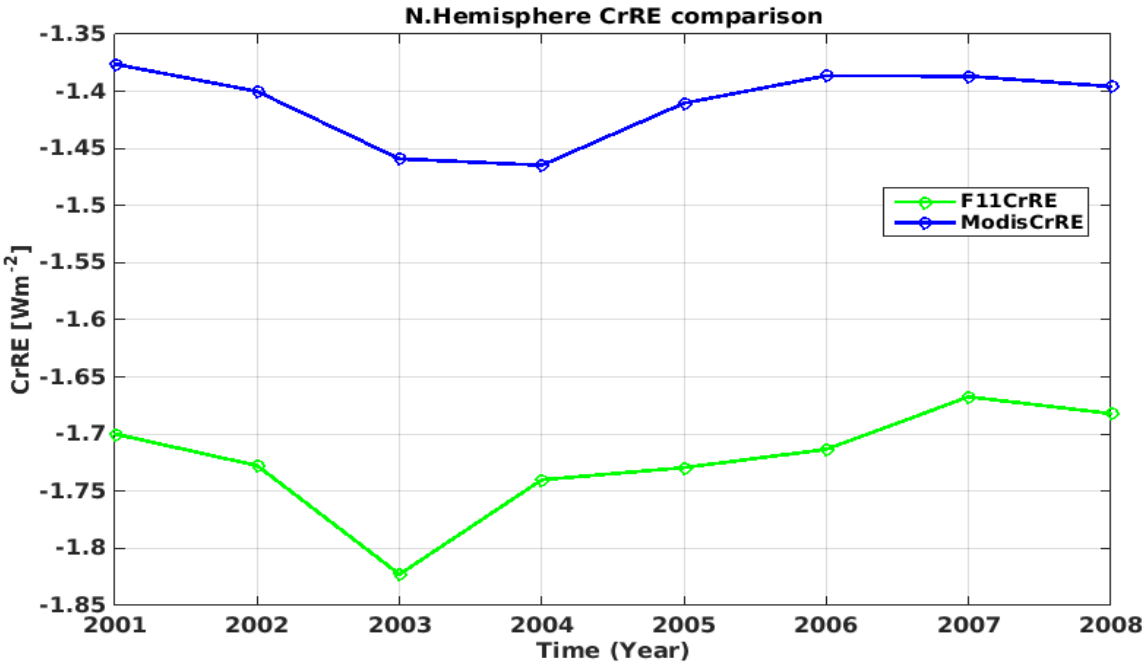

Figure 2.10: Annual mean Northern Hemisphere LCrRE timseries derived for the current study (ModisCrRE) and by Flanner et al., [2011] (F11CrRE) using CAM3 kernels.

2.4 Conclusions

We have estimated a global land-based CrRE (LCrRE) of about -2.6 Wm^{-2} during 2001-2013, with about 59% of the effect originating from Antarctica. For a particular region, LCrRE can vary significantly (e.g., from 0 to -250 Wm^{-2} over Antarctica; Fig. 5) depending on the season. Due to a large contribution from seasonal snow, northern hemisphere LCrRE peaks during April, whereas southern hemisphere LCrRE peaks during the December solstice. About 78% of Northern Hemisphere LCrRE originates from seasonal or non-glaciated snow while about 99.9% of Southern Hemisphere LCrRE comes from glaciated areas. Mountainous region provide a small (-0.037 Wm^{-2}) yet consistent contribution towards LCrRE throughout the year. Higher resolution data has improved the LCrRE estimates relative to previous studies by better resolving the snow impact in mountainous regions and in coastal areas, leading to a 18% smaller estimate of northern

hemisphere LCrRE during 2001-2008 in this study than in *Flanner et al.* (2011). Inter-annual variations between these two studies are well correlated (r=0.78), indicating that these data are useful in determining longer term trends in LCrRE.

Snow cover, however, is patchy on substantially smaller spatial scales than the 0.05 degree resolution analysis applied here. No significant trend over time has been observed in global annual LCrRE values between 2001 and 2013, though significant reductions in cryospheric influence are evident over large areas of northern Eurasia, especially during spring. Slightly negative LCrRE trends (indicating increased albedo) are evident over Antarctica, possibly due to increased snowfall frequency. LCrRE primarily depends on albedo contrast induced by snow and the propagation of surface albedo anomalies to top-of-atmosphere energy fluxes. A slight variation in either of the two can cause a major impact on LCrRE estimates. Sensitivity analysis shows a secondary dependency of LCrRE on MODIS snow flag and global climatology derived using MODIS surface albedo product, and changing either of those drops the LCrRE estimates by about 8% globally. Using different MODIS data quality flags (Q2 & Q4) does not have a significant effect on our LCrRE estimates. Using different radiative kernels can cause a variation of about 3-16% in global LCrRE as compared to LCrRE with the CAM4 kernel, depending on the atmospheric attenuation present in each particular model due to cloud cover and aerosols.

For the consistency, we tried not use any partial year data available at the time of analysis. Also, adding another year of the data (year 2014) would not have made any significant impact on the results. However, it would be beneficial to look into long term trends (about 20-30 years) and comparison with previous research, with more MODIS data available in future.

Appendix A: Snow-covered albedo climatology by land classification

Definitions for different land classes used in the MODIS MCD12C1 product are provided by the International Geosphere-Biosphere Programme (IGBP). Table A.1 provide mean (μ) and standard deviation (σ) of surface albedo for each land class type using section 2.2 algorithm.

Table A.1: Mean (μ) and standard deviation (σ) of snow-covered surface albedo for different land class types. The averaging filter used to determine snow presence was based on both MODIS and NISE datasets of snow, and thus these averages are specific to the current study. MODIS provides surface albedo only over land, so albedo for water cannot be determined.

Land Class Type	**Mean (μ)**	**Std Dev (σ)**
Water	N/A	N/A
Evergreen Needleleaf forest	0.30	0.008
Evergreen Broadleaf forest	0.21	0.005
Deciduous Needleleaf forest	0.33	0.024
Deciduous Broadleaf forest	0.33	0.018
Mixed forest	0.29	0.013
Closed shrublands	0.42	0.023
Open shrublands	0.54	0.046
Woody savannas	0.40	0.025
Savannas	0.46	0.031
Grasslands	0.48	0.038
Permanent wetlands	0.41	0.027
Croplands	0.49	0.036
Urban and built-up	0.37	0.019
Cropland/Natural vegetation mosaic	0.41	0.026
Snow and ice	0.72	0.033
Barren or sparsely vegetated	0.37	0.023

Chapter 3

An improved carbon dioxide snow spectral albedo model: Application to Martian conditions

3.1 Introduction

The Martian atmosphere consists primarily of carbon dioxide, and Martian polar caps are covered primarily with carbon dioxide ice [*Leighton and Murray*, 1966; *Herr and Pimentel*, 1969; *Larson and Fink*, 1972; *Forget*, 1998; *Bibring* et al., 2005]. H_2O ice is also present at the surface of the perennial ice caps, with small amounts of seasonal deposition in other parts of the planet [e.g., *Kieffer* et al., 2000; *Bibring* et al., 2004; *Brown* et al., 2014]. Significant portions of atmospheric CO_2 (25-30%) deposit seasonally in each hemisphere, as indicated by model simulations and surface pressure measurements [*Tillman* et al., 1993; *Forget* et al., 1998; *Kieffer and Titus*, 2001]. To understand the impact of these ices on the planet's cryosphere albedo, it is important to accurately determine the spectral dependence of CO_2 snow albedo and influences of properties such as dust content, ice grain size, and snow thickness, as well as the albedo effects of mixing and layering of CO_2 and H_2O snow.

Our work determines the albedo of CO_2 snow by extending the Earth-based Snow, Ice, and Aerosol Radiation (SNICAR) model [*Flanner* et al., 2007; *Flanner* et al., 2009], originally designed for H_2O snow. SNICAR utilizes the multiple scattering, multi-layer

two-stream radiative approximation described by *Toon* et al. [1989], with the delta-hemispheric mean approximation. We extend the current version of SNICAR from 470 bands (over the wavelength range 0.3-5.0 μm) to 480 bands spanning 0.2-5.0 μm at 10 nm spectral resolution. We include these extra 10 bands in the ultraviolet (UV) spectrum because of the lack of ozone in the Martian atmosphere compared to Earth [*Montmessin and Lefèvre*, 2013], meaning more UV radiation reaches the Martian surface and interacts with snow. A single-layer implementation of SNICAR can be operated interactively on the web at: *http://snow.engin.umich.edu*.

Very few studies have focused on modeling of Martian CO_2 snow albedo across the UV, visible and near-IR spectrum [*Warren* et al., 1990; *Hansen*, 1999; *Bonev* et al., 2008]. *Langevin et al*., [2007] and *Appéré et al.*, [2011] present modeled near-IR albedo of Martian cryospheric surfaces, as discussed in Section 4. With the availability of more accurate and spectrally-resolved laboratory measurements of CO_2 ice complex refractive indices across the solar spectrum [*Hansen*, 1997; *Hansen* 2005], we provide improved and updated spectral albedos of carbon dioxide snow with applicability to Martian conditions. The presence of light-absorbing impurities generally lowers snow albedo. We simulate the impact of Martian dust [*Wolff* et al., 2006; *Wolff* et al., 2009; *Wolff* et al., 2010] and palagonite [*Clark* et al., 1990; *Clancy* et al., 1995] on surface cryosphere albedo. Palagonite is a volcanic rock and serves as a terrestrial analog for Martian dust [*Banin* et al., 1997]. We perform multiple analyses to determine the sensitivity of cryosphere spectral albedo to the amount and type of dust, presence of both ices, ice grain size, snow layer thickness, and solar zenith angle. We also compare the results of our simulations with observed Mars surface albedo derived from Compact Reconnaissance Imaging Spectrometer (CRISM)

measurements, and the OMEGA instrument [*Appéré et al.,* 2011] (section 4). Apparent albedo, derived by *Brown* et al [2014] using CRISM measurements, were provided by Adrian Brown (SETI Institute, personal communication), and observations and modeled albedo from the OMEGA instrument were provided by Thomas Appéré (IPAG, Grenoble, personal communication).

3.2 Data and methodology

Hansen [1997, 2005] made extensive laboratory measurements of the complex refractive indices of solid CO_2 ice in the spectral range from 0.174 μm to 333 μm. We apply these data along with Mie calculations to derive optical properties of different lognormal size distributions of CO_2 ice particles, reported with effective radius (r_{eff}), or the surface area-weighted mean radius of the size distribution. Our simulations of H_2O snow albedo utilize refractive indices of H_2O ice provided by *Warren and Brandt* [2008]. We use "central hematite" dust mineral fractions from *Balkanski* et al. [2007] as a proxy of typical Earth dust. These mineral abundances are representative of aeolian dust from the Saharan desert. Refractive indices for this dust mixture are derived using the Maxwell-Garnett mixing approximation, following e.g., *Sokolik and Toon* [1999], along with measurements of mineral refractive indices from various sources. Refractive indices of Martian dust (hereafter Mars dust) were provided by Mike Wolff (Space Science Institute, personal communication), and were derived using data from instruments onboard the Mars Reconnaissance Orbiter (MRO), as described by *Wolff* et al. [2009], and *Wolff* et al. [2010]. We combine refractive indices of palagonite from *Clark* et al. [1990] over the 0.2 μm to 0.6 μm spectral range and measurements from 0.6 μm to 5 μm made by *Clancy* et al. [1995]

to derive data over the solar spectrum. In this study, we divide our broadband (0.2-5.0 μm) into two sub-regions: Visible (0.2-0.7 μm) and near-IR (0.7-5.0 μm).

We determine the spectrally-varying single scatter albedo (ω_0), scattering asymmetry parameter (g), and mass extinction cross-section for all three dust types using Mie Theory with an assumed gamma size distribution [*Hansen and Travis,* 1974] with r_{eff}=1.5μm and effective variance (ν_{eff})=0.3 [*Wolff* et al., 2006]. Figure 3.1 shows the optical properties for these dust types. Mass absorption cross-section (Figure 3.1d) is the product of single scatter co-albedo (Figure 3.1a) and mass extinction cross-section (Figure 3.1b). We assume the same dust density of 2000 kg/m^3 for both palagonite and Mars dust [*Stroncik and Schmincke*, 2002], and a dust density of 2570 kg/m^3 for Earth dust, based on the volume fraction-weighted densities of the constituent minerals [*Balkanski* et al., 2007].

The bulk optical properties (extinction optical depth (τ), ω_0, and g) for each snow layer are calculated from the abundances of each constituent [e.g., *Flanner* et al, 2007], with τ calculated as the sum of that associated with each constituent, ω_0 as a τ-weighted average of each constituent, and g as a scattering optical depth (product of τ and ω_0) weighted average of the asymmetry parameter of each constituent. These bulk layer properties are then applied in the two-stream multiple scattering approximation adopted by SNICAR. We utilize this extended framework of SNICAR to first simulate the albedo of pure CO_2 snow across the visible and near-IR spectrum. We then explore and compare the impacts of Earth dust, Mars dust and palagonite on CO_2 and H_2O snow albedo. Finally, we adopt a two layer model (with the bottom layer being semi-infinite) to calculate the impacts of H_2O snow presence on top of CO_2 snow and vice-versa. In all other cases we assume only a single snow layer, either with semi-infinite thickness or varying shallow thicknesses.

Here, a layer with thickness of 100 m is referred to as semi-infinite. Figure 3.2 shows simplified diagrams of the various model configurations applied in this study.

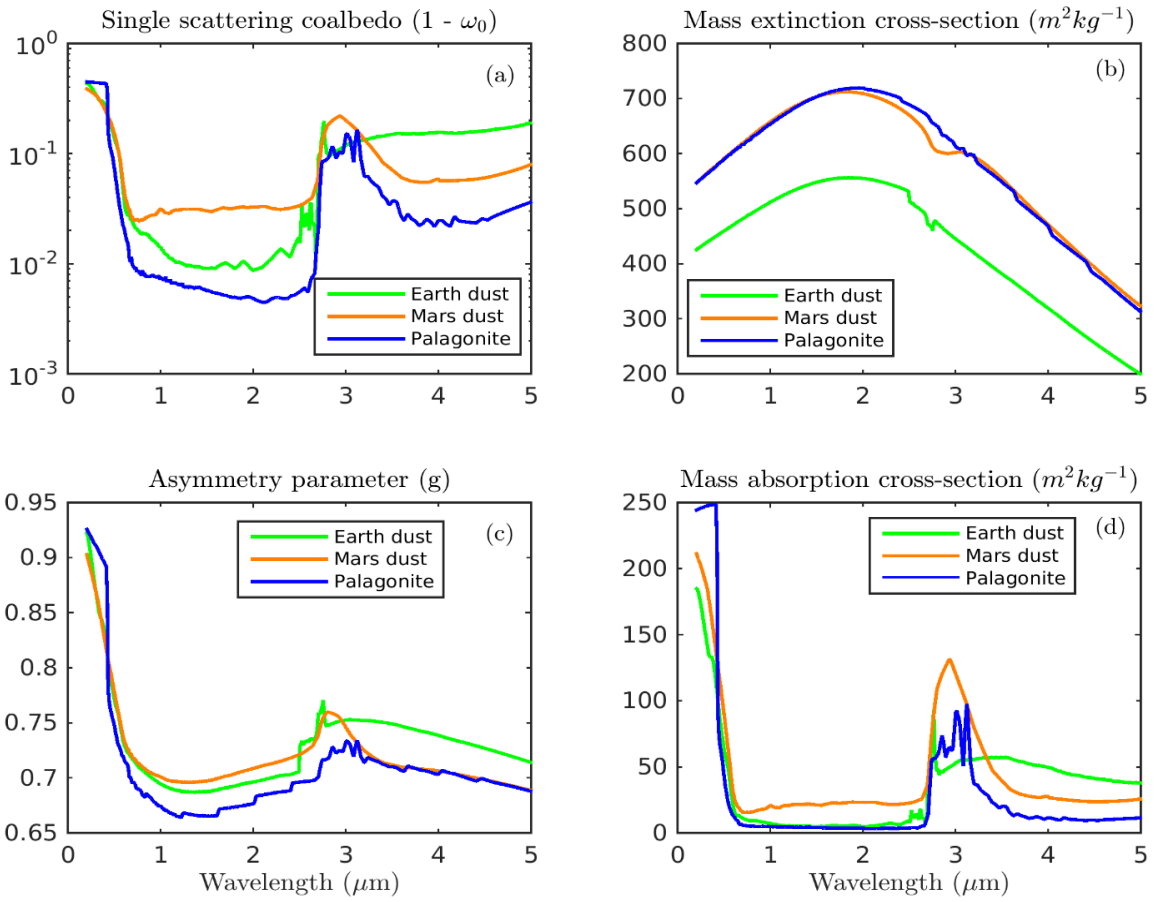

Figure 3.1: Spectral optical properties of the Earth dust, Martian dust, and palagonite applied in this study.

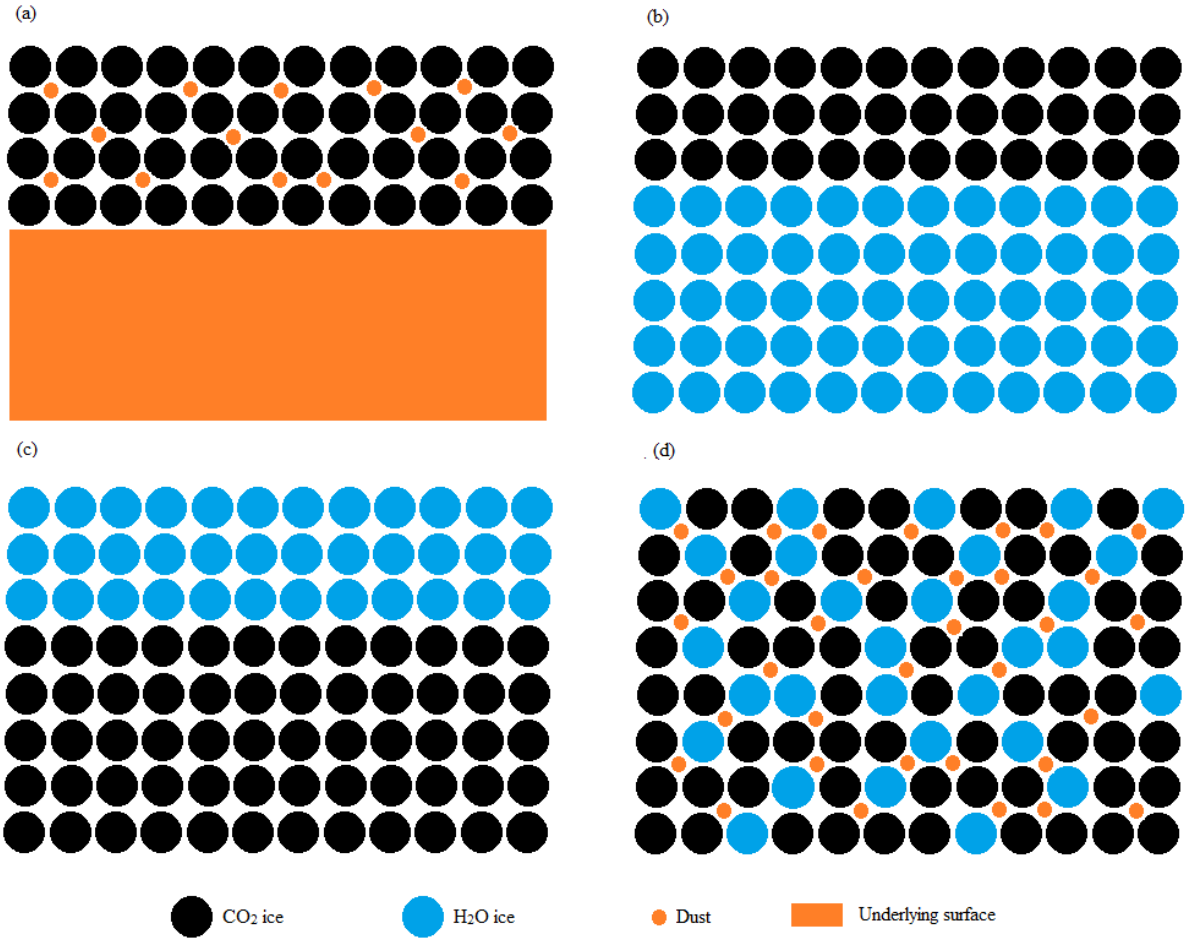

Figure 3.2: Schematic of the various model configurations applied in this study: (a) a single CO_2 or H_2O snow layer (with dust) on top of solid underlying surface; (b) CO_2 snow with variable thickness on top of a semi-infinite H_2O snow layer; (c) H_2O snow with variable thickness on top of a semi-infinite CO_2 snow layer; (d) mixed snow layers with dust.

3.3 Results

Figure 3.3 shows the spectral hemispheric albedo of pure, semi-infinite CO_2 and H_2O snow with spherical grain effective radius of 100 μm and solar zenith angle of 60°. It is evident that the CO_2 is more reflective than H_2O snow, especially in the near-IR spectrum. Table 3.1 compares solar broadband, visible and near-IR albedo for both types of snow, where band-averaged values are weighted with solar spectral irradiance measurements from *Labs and Neckel* [1968]. H_2O snow albedo is only about two-thirds of the CO_2 snow albedo in the near-IR spectrum, although this ratio is grain size dependent (section 3.3.2). With the presence of both CO_2 and H_2O ices on Martian polar caps, the contrasting reflectivity of these types of snow could significantly impact planetary shortwave energy fluxes, both at the surface and top of atmosphere.

Snow albedo depends on many physical quantities, including grain size, solar zenith angle, layer thickness, and type and amount of impurities. We performed a sensitivity analysis to understand the effect of these parameters on carbon dioxide snow albedo, and describe this analysis below. We assume an effective grain size of 100 μm and solar zenith angle of 60° for all analyses, unless stated otherwise. For comparing CO_2 and H_2O albedo, we also assume identical pore volume fractions for each type of ice. A typical bulk density of settled snow on Earth is 200 kg/m^3 (e.g., *EN 1991-1-3*). Because the bulk densities of H_2O and CO_2 ice are assumed to be 917 kg/m^3 and 1500 kg/m^3, respectively, we therefore assume H_2O and CO_2 snow densities of 200 kg/m^3 and 327.15 (= 200×1500/917) kg/m^3, respectively.

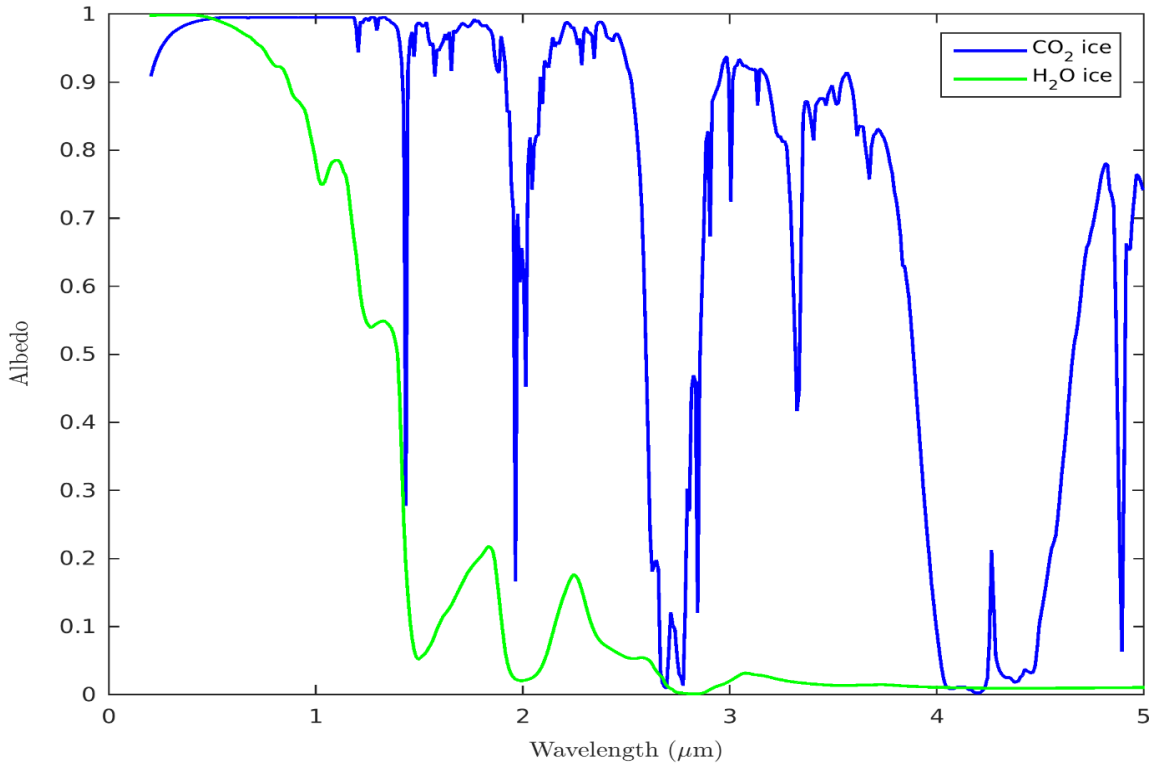

Figure 3.3: Comparison of CO_2 and H_2O snow spectral albedo simulated with the SNICAR model (Grain size = 100 µm and solar zenith angle = 60°)

Table 3.1: Albedo values for pure, semi-infinite CO2 and H2O snow in different spectral bands (Grain size = 100 µm and solar zenith angle = 60°)

	pure CO_2	**pure H_2O**
Visible (0.2-0.7 µm)	0.991	0.988
Near-IR (0.7-5.0 µm)	0.952	0.609
Broadband (0.2-5.0 µm)	0.970	0.787

3.3.1 Solar zenith angle

We see little effect of solar zenith angle on CO_2 snow albedo (Figure 3.4). The broadband albedo only changes from 0.98 to 0.96 over the 80° change in zenith angle. This compares with H_2O snow albedo, which varies from 0.75 to 0.82 for the same set of parameters. Variability in albedo with solar zenith angle is greater in more absorptive parts of the spectrum (i.e., the near-IR), but for CO_2 snow the variability is small in the parts of the spectrum containing most of the solar energy.

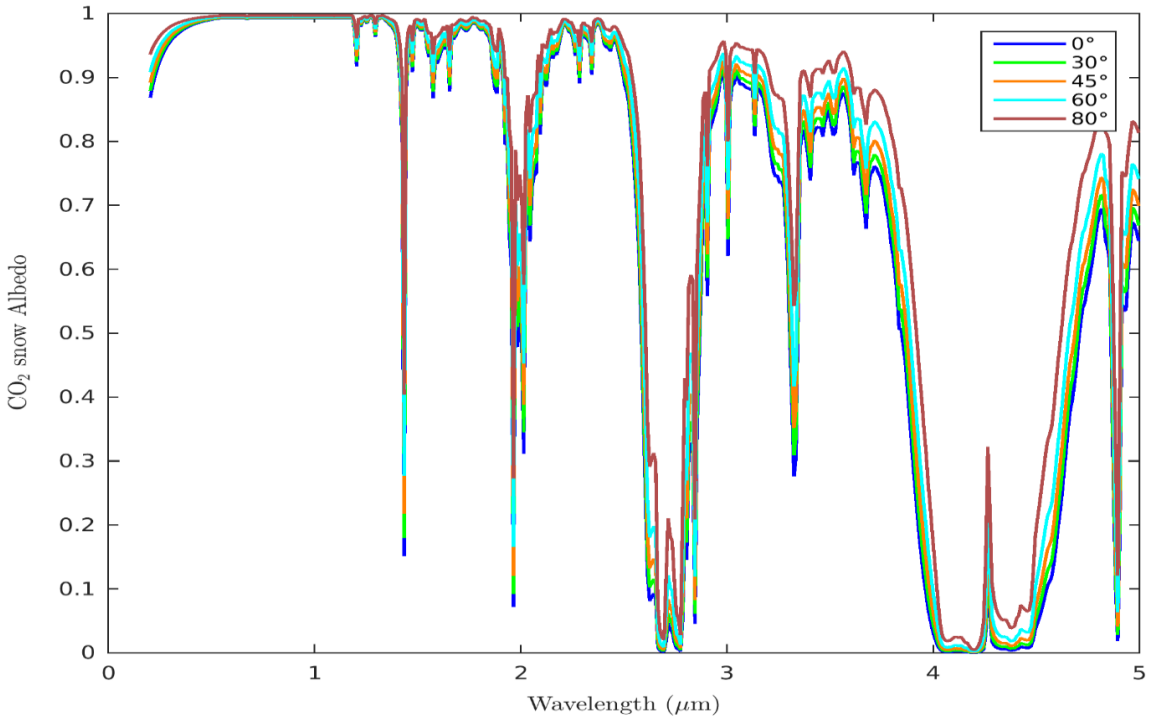

Figure 3.4: Variation of CO_2 snow albedo with solar zenith angle

3.3.2 Grain Size

The results of our simulation indicate a monotonic decrease in snow albedo with increasing effective grain size (Figure 3.5). With larger grain size, ice volume per surface area increases, resulting in greater absorption of light, as also occurs with H_2O snow [e.g., *Wiscombe and Warren*, 1980]. The broadband (near-IR) albedo of CO_2 snow drops from 0.98 to 0.93 (0.96 to 0.89) for grain size increasing from 50 μm to 1500 μm. This is also smaller variability than exhibited by H_2O snow, whose broadband (near-IR) albedo changes from 0.82 to 0.65 (0.66 to 0.37) over the same range in effective grain size. CO_2 snow albedo varies less with grain size because CO_2 ice is inherently less absorptive in the near-IR than H_2O ice. Consequently the incremental increase in absorption associated with increasing photon path length within larger ice grains is smaller for CO_2 snow than H_2O snow.

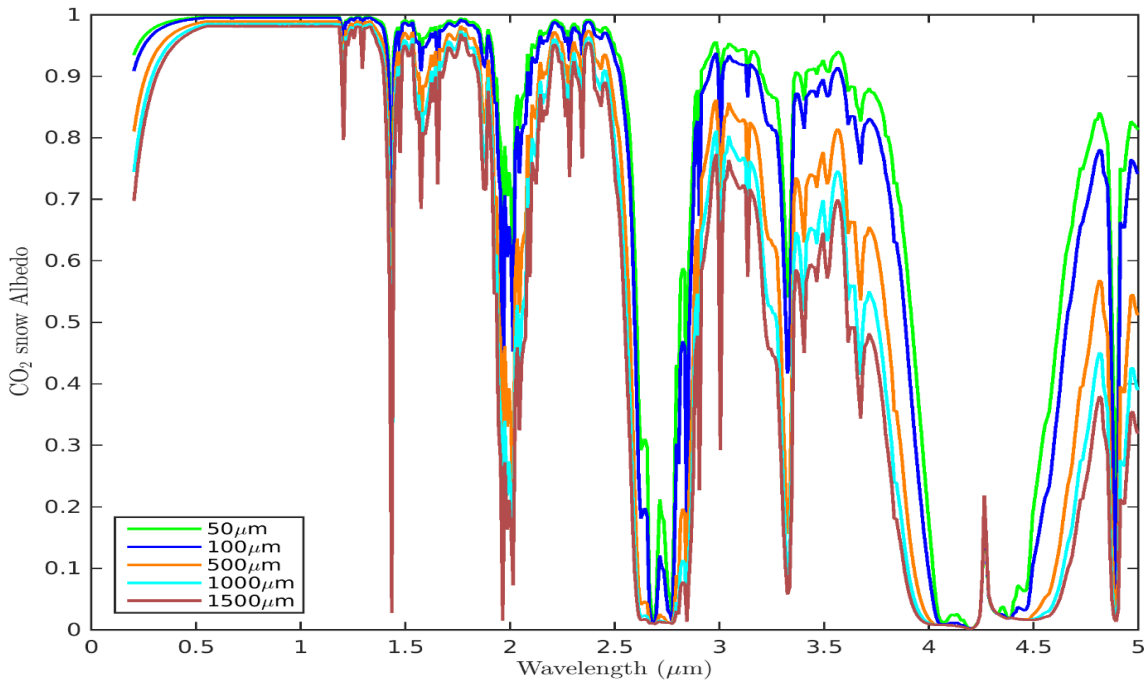

Figure 3.5: Variation of CO_2 snow albedo with effective grain radius

3.3.3 Snow thickness

Figure 3.6 shows the combined impacts of snow thickness and grain size on CO_2 and H_2O broadband snow albedo, for snow overlying a surface with spectrally constant albedo of 0.2 (model configuration shown in Figure 3.2a). For a given grain size, CO_2 snow albedo has a larger variation over the entire thickness range compared to H_2O snow albedo. CO_2 snow albedo is almost independent of grain size when the snow layer is thick, and consequently all curves saturate at a similarly high albedo ranging from 0.93-0.98. However, H_2O snow albedo has greater dependence on grain size, as each curve saturates at a different albedo ranging from 0.65-0.82.

We define "saturation thickness" as the snow thickness needed for the broadband albedo to differ by less than 0.01 from its semi-infinite value. Once the snow layer thickness exceeds the saturation thickness, the impact of the underlying surface becomes negligible as an insignificant amount of light penetrates through the snow to interact with the underlying surface. We note, however, that the penetration depth of radiation in snow depends strongly on wavelength, with multiple scattering leading to much deeper penetration and influence of underlying substrate at wavelengths where the ice absorbs weakly [e.g., *Wiscombe and Warren*, 1980]. The saturation thickness also depends on snow density, with higher density producing lower saturation thickness. Table 3.2 presents the saturation thickness required for different grain sizes for both types of snow. The saturation thickness is grain size-dependent, increasing from about 6 to 100 cm, and from about 5 to 83 cm as grain size increases from 50 to 1500 μm for CO_2 and H_2O snow, respectively. With other factors equal, CO_2 snow has higher saturation thickness than H_2O snow because CO_2 ice is less absorptive than H_2O ice, especially in the near-IR region, enabling multiple-

scattered photons to penetrate deeper in the snow. Also the difference in saturation thicknesses increases with larger grain size because of less dependency of CO_2 snow albedo on grain size compared to H_2O snow (section 3.3.2). Finally, we note that studies on optical properties of ice particles have found that the scattering asymmetry parameter is generally smaller for non-spherical ice particles than equal volume/area ice spheres [e.g., *Fu*, 2007; *Libois* et al., 2013; *Räisänen* et al., 2015]. An implication of this is that saturation thickness will be smaller for non-spherical ice particles than values reported here, as photons are scattered less preferentially into the forward direction.

Table 3.2: Saturation snow layer thickness with various grain sizes for each type of snow. CO_2 and H_2O snow densities are 327.15 and 200 kg/m^3, respectively.

Grain Size	CO_2 snow saturation thickness	H_2O snow saturation thickness
50 µm	6.5 cm	5.0 cm
100 µm	10.9 cm	8.9 cm
250 µm	24.0 cm	18.8 cm
500 µm	43.1 cm	33.7 cm
1000 µm	73.8 cm	59.4 cm
1500 µm	100.2 cm	83.2 cm

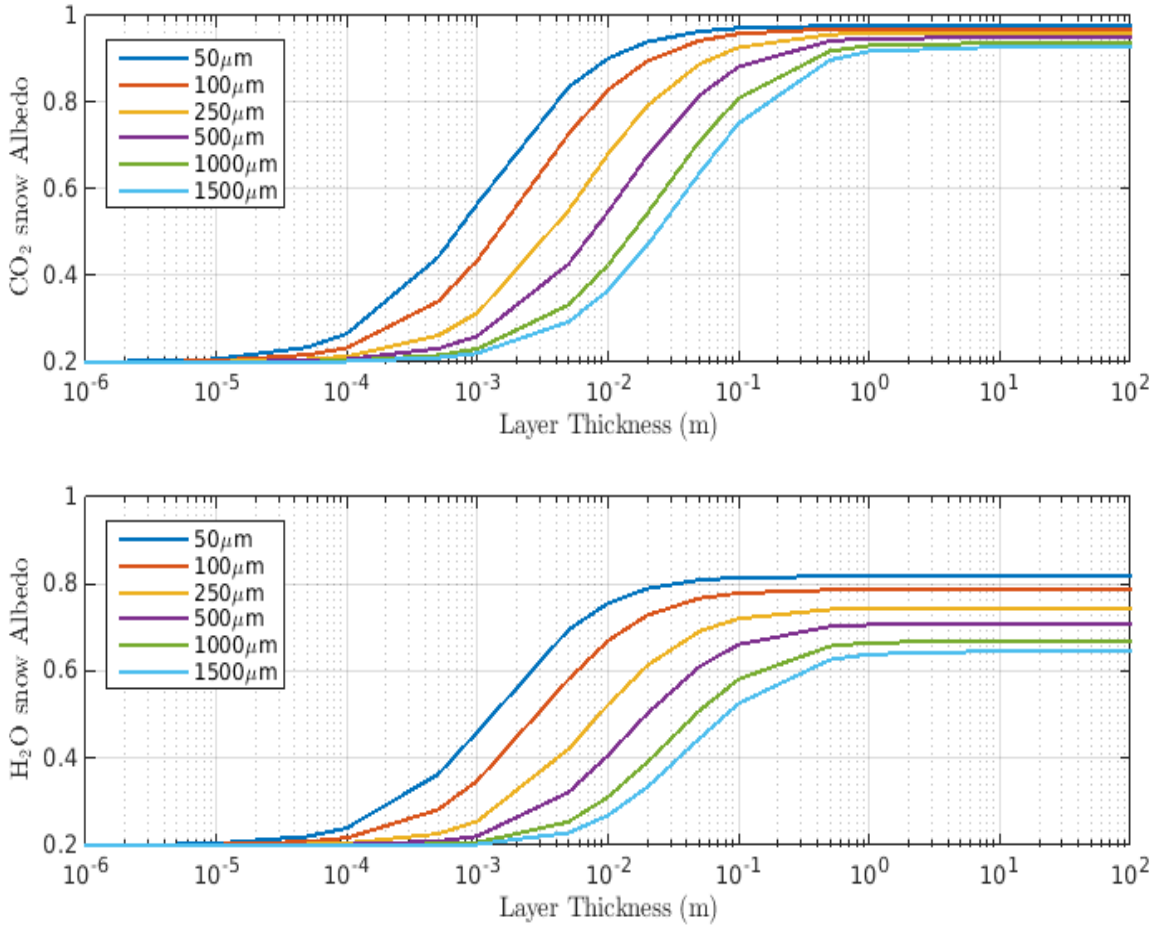

Figure 3.6: Broadband CO_2 (top) and H_2O (bottom) snow albedo dependence on snow layer thickness for various effective grain sizes. The underlying surface is assumed to have a constant albedo of 0.2. The snow density is 327.15 kg/m^3 and 200 kg/m^3 for CO_2 and H_2O snow, respectively.

3.3.4 Dust type

The snow albedo impacts of different types of dust depend on their optical properties, and in particular on their mass absorption cross-section. Here we compare the impacts of Earth dust, Mars dust and palagonite on semi-infinite snow albedo (Figure 3.7). Again, identical size distributions are assumed for each type of dust, and only the refractive indices are varied as input to Mie calculations. Mars dust has the greatest albedo impact of the three between wavelengths of 0.5 and 2.5 μm, which contains most of the incident solar energy, while palagonite has the least. Mars dust is relatively dark due to the presence of higher amount of iron oxides [*Bell III* et al., 1990; *Bell III*, 1996; *Christensen* et al., 2000; *Christensen* et al., 2001a; *Christensen* et al., 2001b], combined with its large mass extinction cross-section. Although average Earth dust has a lower near-IR single-scatter albedo than the Mars dust, it also has a lower mass extinction cross-section across the spectrum, due to its larger density, leading to lower absorption per unit mass of dust, expressed via the mass absorption cross-section (Figure 3.1d).

We consider "mass mixing ratio" as the mass of impurity divided by the mass of ice in which the impurity is mixed. Table 3.3 presents the effective CO_2 snow albedo in the presence of 0.01% mass mixing ratio of dust (kg of dust / kg of ice). Dust causes a larger albedo drop in the visible region (~0.6) compared to the near-IR region (~0.3) because all three types of dust have very low single scatter albedo in the blue and green spectra while ice grains scatter very efficiently at these wavelengths (Figure 3.1). Furthermore, the drop in albedo in the blue spectrum (~0.8) is much higher than the drop in the red spectrum (~0.3), helping explain the planet's red appearance even in its cryospheric regions.

Although palagonite is less absorptive than Mars dust, the spectral variations in albedo impacts of the two species are similar.

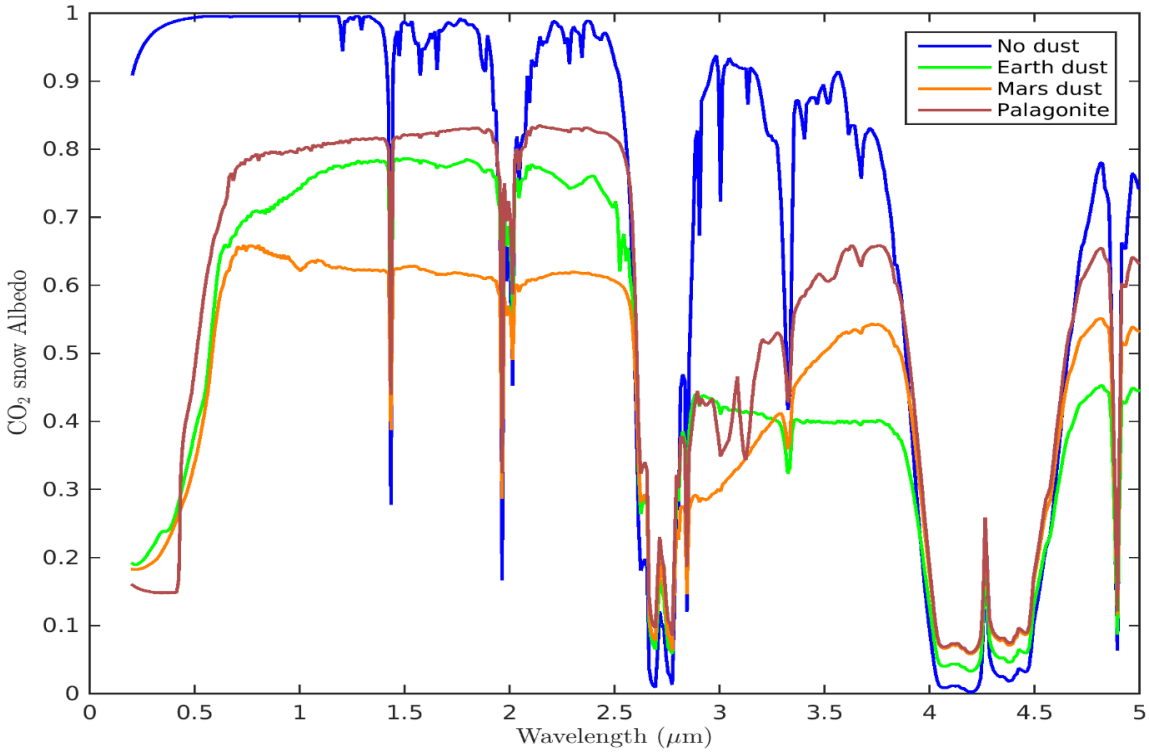

Figure 3.7: Impact of different types of dust on CO_2 snow albedo, with dust mass mixing ratio of 0.01%. The assumed snow grain size is 100 µm.

Table 3.3: Impact of different types of dust on CO_2 broadband snow albedo (grain size of 100 µm), with dust mass mixing ratio of 0.01%.

	pure CO_2	**Earth dust**	**Mars Dust**	**Palagonite**
Visible (0.2-0.7 µm)	0.991	0.429	0.395	0.477
Near-IR (0.7-5.0 µm)	0.952	0.718	0.616	0.779
Broadband (0.2-5.0 µm)	0.970	0.583	0.513	0.637

Table 3.4: Impact of different types of dust on H_2O broadband snow albedo (grain size of 100 μm), with dust mass mixing ratio of 0.01%

	pure H_2O	**Earth dust**	**Mars Dust**	**Palagonite**
Visible (0.2-0.7 μm)	0.988	0.450	0.415	0.494
Near-IR (0.7-5.0 μm)	0.609	0.551	0.503	0.599
Broadband (0.2-5.0 μm)	0.787	0.504	0.461	0.550

Table 3.4 presents the effective H_2O snow albedo in the presence of 0.01% mass mixing ratio of dust. Pure H_2O snow is relatively absorptive in the near-IR spectral region (Table 3.1 & Table 3.4), so dust has little impact on near-IR albedo, or in the most absorptive portions of the spectrum, it even increases albedo (Figure 3.8). Fundamentally, this occurs because the single-scatter albedo of dust exceeds that of H_2O ice grains at wavelengths longer than about 1.5 μm. Similar to CO_2 snow, the drop in albedo is large in the visible region for H_2O snow. However in the near-IR region the change is less than 0.1, leading to smaller broadband albedo impacts of dust on H_2O snow albedo than on CO_2 snow albedo. These differences indicate that dust can have greater impact on Martian cryosphere albedo than Earth cryosphere albedo due to the higher abundance of CO_2 ice compared to H_2O ice.

3.3.5 Dust Concentration

Figure 3.9 shows the effect of varying amounts of Mars dust on CO_2 snow albedo (Figure 3.2a). It is obvious that albedo decreases with increasing amount of dust, except in the strong absorption bands of CO_2 ice (e.g., near 1.4 μm, 1.9 μm, and 2.7 μm). Again we see maximum impact in the visible part of the spectrum. Saturation of the albedo from this type of dust is evident with dust mixing ratios exceeding 0.01%, with almost no difference

in albedo between scenarios with 0.1% and 1% dust. Also, the strong absorption features of CO_2 snow at various wavelengths disappear with high dust concentrations.

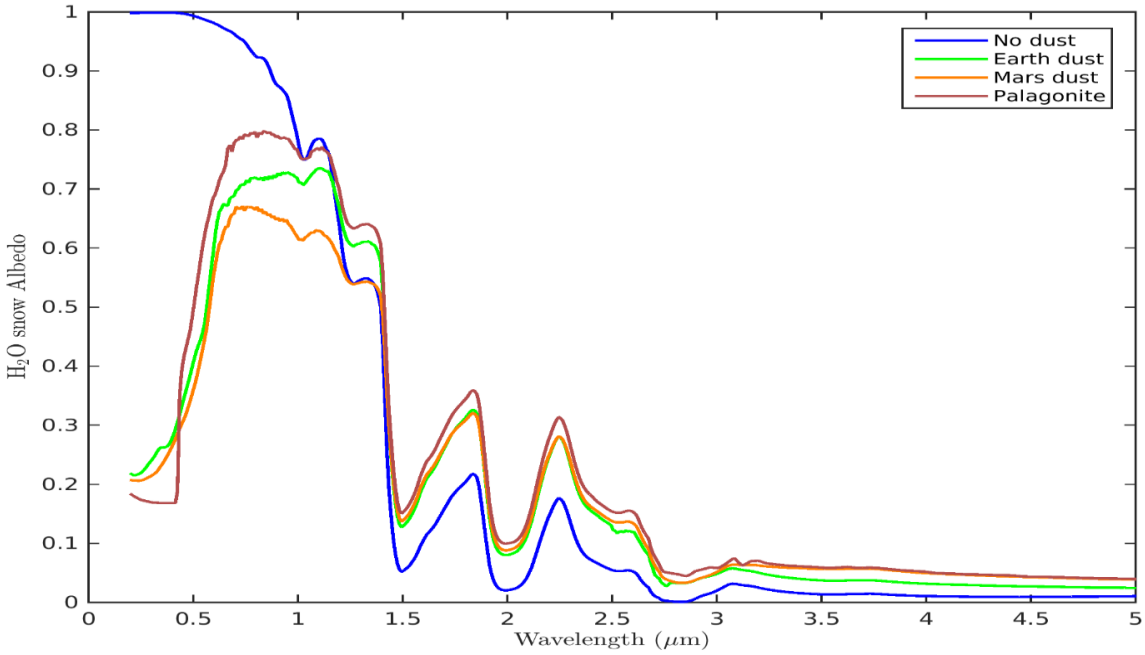

Figure 3.8: Impact of different types of dust on H_2O snow albedo, with dust mass mixing ratio of 0.01%. The assumed snow grain size is 100 µm.

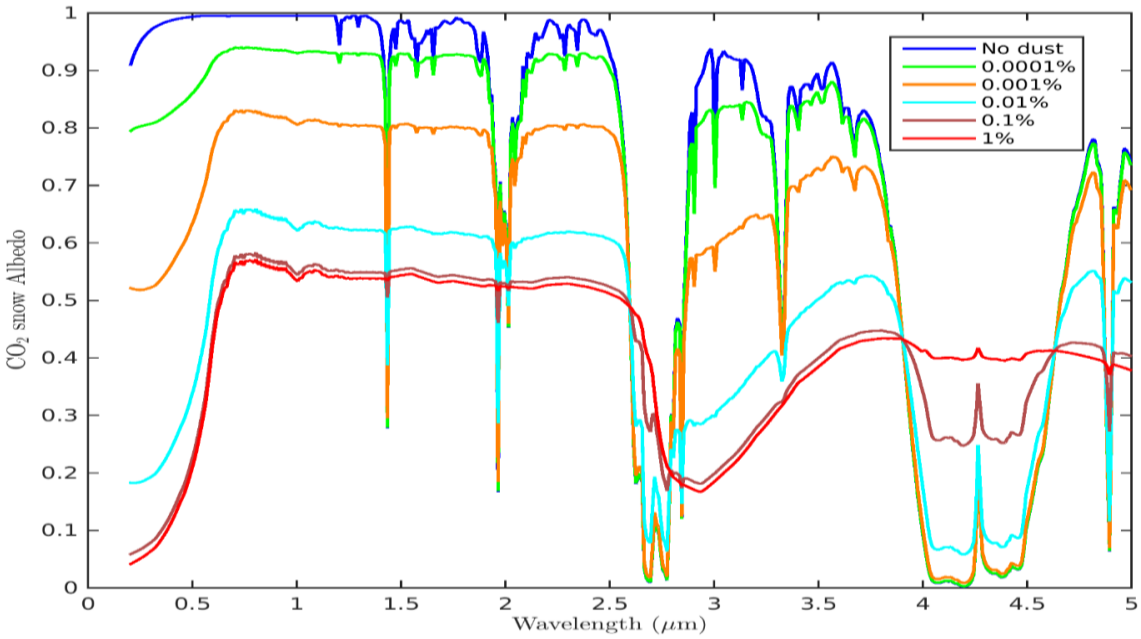

Figure 3.9: Impact of various amounts of Martian dust on CO_2 snow albedo. Snow effective grain radius is 100µm.

3.3.6 Presence of both H_2O and CO_2 ice

3.3.6.1 Separate layers

H_2O and CO_2 ice interact quite differently with radiation in the visible and near-IR portions of the spectrum and also exhibit different sensitivities to different physical parameters. These ice types are also known to co-exist on the surface of Mars [e.g. *Byrne* et al., 2008; *Brown* et al., 2014]. Here, we explore the albedo effects associated with thin slabs of one type of ice overlying the other, building on sensitivity studies conducted by *Warren* et al., [1990]. Figure 3.10 shows spectral albedo of surfaces with H_2O snow on top of CO_2 snow (scenario shown in Figure 3.2c), and Figure 3.11 shows albedo with the reverse situation (scenario shown in Figure 3.2b).

Albedo decreases markedly with the presence of thin slabs of H_2O snow on top of CO_2 snow. This decrease occurs more rapidly with increasing thickness of H_2O ice than the rate of albedo increase that occurs with increasing thickness of CO_2 snow overlying H_2O snow. For a grain size of 100 μm, about 2.5 cm of H_2O snow is required to completely mask out the albedo effect of CO_2 snow (Table 3.5), whereas about 5.5 cm of CO_2 snow is required to completely mask out the albedo effect of underlying H_2O snow (Table 3.6). Again, differences are more pronounced in the near-IR spectrum (e.g., Figure 3.3, Table 1), where the contrast in absorptivity between CO_2 and H_2O ice is greater (Table 3.5 & Table 3.6). Rows marked with an asterisk (*) correspond to saturation thickness. In summary, very little H_2O snow is needed to mask the presence of underlying CO_2 snow, whereas a larger thickness of CO_2 snow is needed to prevent underlying, more absorptive H_2O snow from effecting surface albedo.

Warren et al., [1990] determined that the presence of H_2O snow on top of CO_2 snow will increase the net surface albedo, contrary to the analysis presented here. The CO_2 ice refractive indices applied in that study, however, were measured using unpurified commercial dry ice [*Egan and Spagnolo*, 1969], and data in the 1.0-2.5 μm spectral region were extrapolated from the 0.3-1.0 μm spectral region. The higher quality measurements on pure CO_2 ice provided by *Hansen* [1997, 2005], and applied here, indicate that CO_2 ice is much less absorptive than previously assumed, leading to our opposite conclusion.

Figure 3.12 shows the broadband net surface albedo dependence on layer thickness for different snow types. The black lines indicate the saturation thickness (section 3.3.3) for the two scenarios discussed above. To further explore the behavior of albedo with layer thickness, we divide each curve into two regions: with thickness lesser and higher than saturation thickness. Table 3.7 lists the slopes of albedo per layer thickness for these two regions. For top layer thickness less than saturation thickness (first region), higher slope (in absolute values) of data shown in Figure 3.12a than Figure 3.12b substantiates the conclusion that H_2O snow is harder to mask out compared to CO_2 snow. However, for the second region with thickness higher than saturation thickness, the scenario with overlying CO_2 snow (Figure 3.12b) demonstrates higher absolute slope than the reverse situation. This indicates that H_2O snow is less sensitive to thickness variation (once a minimum threshold is reached), owing to its more absorptive nature in the near-IR spectrum compared to CO_2 snow.

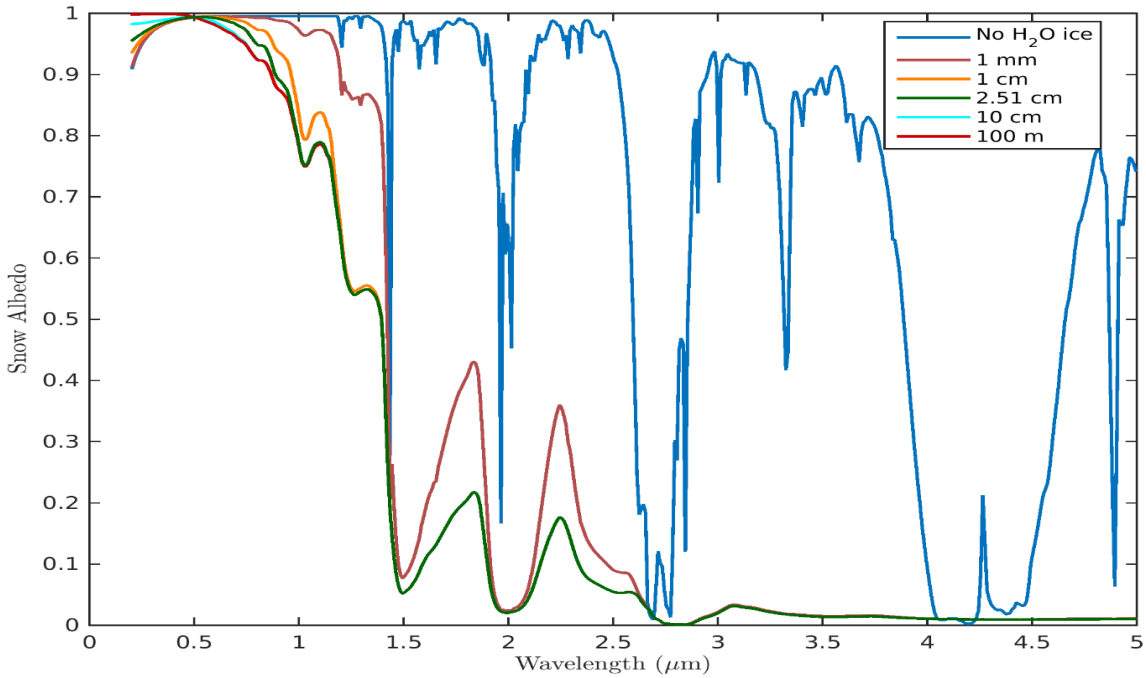

Figure 3.10: Spectral albedo of surfaces with H_2O snow layers of varying thickness on top of CO_2 snow. The green curve thickness corresponds to saturation thickness.

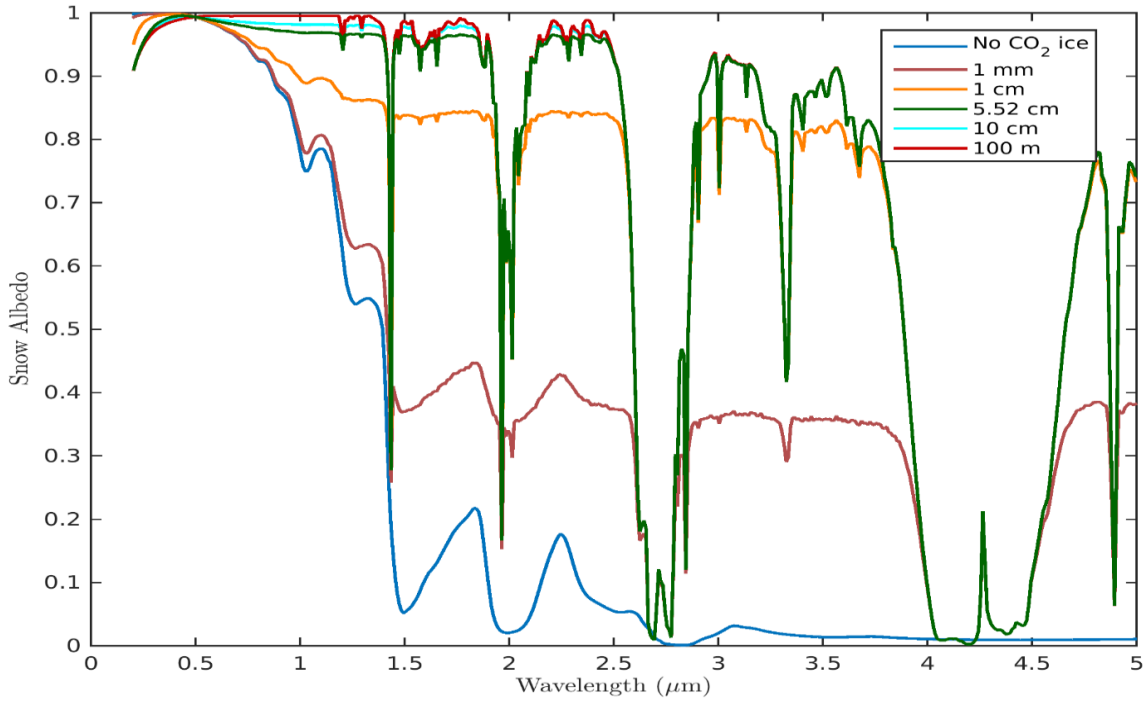

Figure 3.11: Spectral albedo of surfaces with CO_2 snow layers of varying thickness on top of H_2O snow. The green curve thickness corresponds to saturation thickness.

Table 3.5: Broadband albedos of surfaces with H_2O snow layers on top of CO_2 snow

H_2O layer thickness	Vis	Near-IR	Broadband
0	0.991	0.952	0.970
1 mm	0.991	0.739	0.857
1 cm	0.991	0.639	0.804
2.51 cm*	0.987	0.618	0.793
10 cm	0.990	0.610	0.787
100 m	0.988	0.609	0.787

*Saturation thickness (section 3.3.3)

Table 3.6: Broadband albedos of surfaces with CO_2 snow layers on top of H_2O snow

CO_2 layer thickness	Vis	Near-IR	Broadband
0	0.988	0.609	0.787
1 mm	0.988	0.703	0.837
1 cm	0.989	0.869	0.925
5.52 cm*	0.989	0.934	0.960
10 cm	0.990	0.943	0.965
100 m	0.991	0.952	0.970

*Saturation thickness (section 3.3.3)

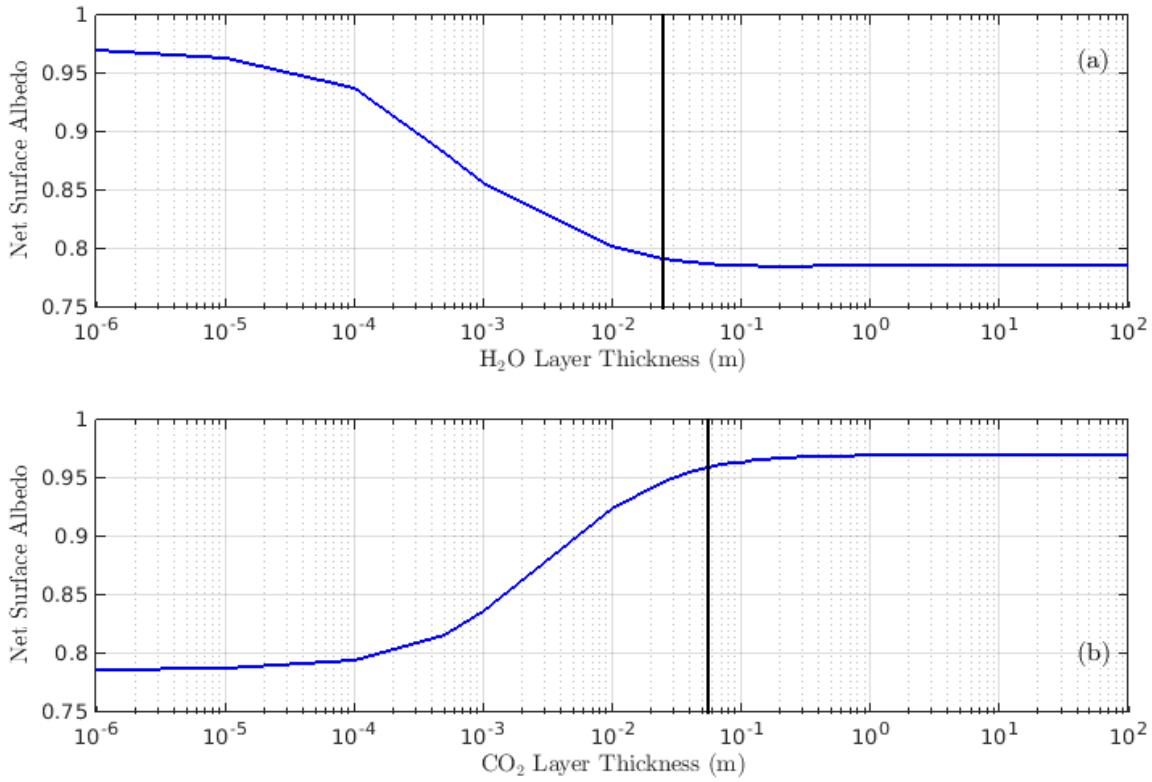

Figure 3.12: Dependence of net surface broadband snow albedo on layer thickness for (a) an H_2O snow layer on top of a semi-infinite CO_2 snow layer, and (b) a CO_2 snow layer on top of a semi-infinite H_2O snow layer. The black line indicates the saturation thickness for each case. Snow grain size is assumed to be 100 µm in both cases.

Table 3.7: Slopes of albedo per change in layer thickness for the two scenarios shown in figure 12

Thickness regime	**H_2O snow layer on top of CO_2 snow layer (Fig 11a)**	**CO_2 snow layer on top of H_2O snow layer (Fig 11b)**
Less than saturation thickness	$-7.10\ m^{-1}$	$+3.14\ m^{-1}$
Higher than saturation thickness	$-5.54\times10^{-5}\ m^{-1}$	$+1.05\times10^{-4}\ m^{-1}$

3.3.6.2 Mixed layers

In addition to the possibility of different snow types being present as separate layers, both types of snow can also become mixed together on the surface of Mars [e.g. *Brown* et al., 2014]. In this section, we explore the net surface albedo changes caused by one snow type becoming mixed with the other snow type. In practice, this is simulated by treating the less abundant ice type as an externally-mixed "impurity" with specified mass mixing ratio (scenario shown in Figure 3.2d), analogous to the treatment of dust described earlier. Figure 3.13 shows the net surface albedo when H_2O snow is present as an impurity within CO_2 snow, and Figure 3.14 shows the net surface albedo for the reverse situation. We assume a semi-infinite snow layer, and effective grain size of 100 μm for both snowpacks.

Broadband (near-IR) albedo drops by ~0.18 (~0.34) for an associated increase of H_2O snow from 0% to 10% within CO_2 snow. However, broadband (near-IR) albedo increases by ~0.10 (~0.18) in the reverse situation. This is consistent with our earlier findings that H_2O snow is relatively darker (especially in the near-IR region) compared to CO_2 snow, hence causing larger impact on net surface albedo. 0.01% of H_2O snow is sufficient to reduce the net broadband albedo of the mixture by 0.03, while 1% of CO_2 snow is required to increase the net surface broadband albedo of the mixture by same amount.

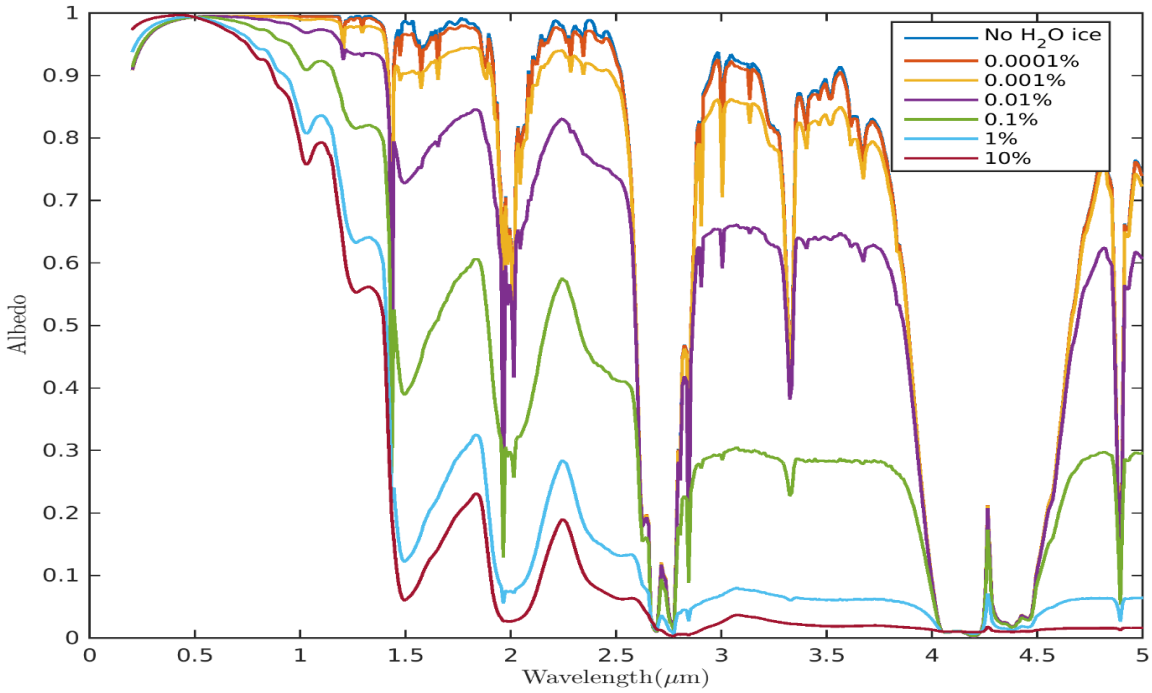

Figure 3.13: Spectral albedo of surfaces with H_2O ice present as an impurity within CO_2 snow. Effective grain size for both snow types is 100 µm and the layer is semi-infinite.

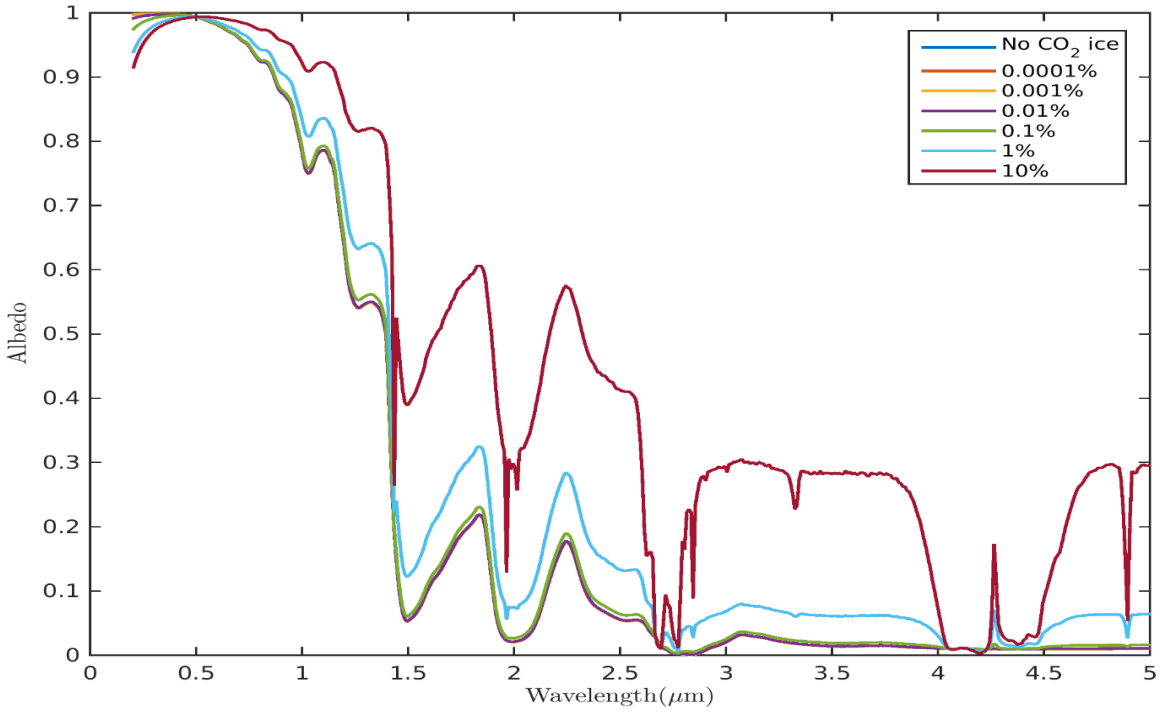

Figure 3.14: Spectral albedo of surfaces with CO_2 ice present as an impurity within H_2O snow. Effective grain size for both snow types is 100 µm and the layer is semi-infinite.

3.4 Comparison with observed Martian albedo

In this section, we compare the results of our simulations with some observations of surface albedo in the Martian cryosphere and try to identify parameter combinations that produce reasonable agreement between the modeled and observed data.

3.4.1 Comparison with CRISM measurements

We obtained spectral albedo data for one location in the Southern Hemisphere [point A, Fig. 3 of *Brown* et al., 2014] identified to have a majority of CO_2 ice (hereafter location S), and one location from the Northern Hemisphere [point B, Fig 4c of *Brown* et al., 2012] identified to have mostly H_2O ice (hereafter location N). The observed albedos were obtained using radiance measurements from CRISM in the 1-4 μm spectral range. Therefore we only compare our simulations in this spectral range.

Since the albedo data display a time dependency, we first take the average of all available spectra to generate a mean spectral curve for each location. Then we determine the best fit for each location by minimizing the weighted RMSE between the mean spectral curve and our simulations, which span a wide range of the parameter space described earlier. Spectral weighting for the RMSE calculation is done with the same solar spectral irradiance measurements [*Labs and Neckel*, 1968] applied throughout this study.

Table 3.8 lists the best fit values of various parameters along with spectrally-weighted RMSE values for both locations. The presence of any CO_2 ice tends to increase the RMSE at location N. This happens because observations from location N occurred during early spring to mid-summer in that hemisphere, when there is likely no CO_2 ice present on the surface [e.g. *Brown* et al., 2014]. Location S needs about one-third the amount of dust as compared to location N for optimal fitting. One reason for this is that

Location S is deemed to have some coincident H_2O ice, which functions as a competing impurity to dust because H_2O snow substantially darkens albedo in the near-IR spectral region. For location S, changing CO_2 ice grain size does not have any significant impact on RMSE, while the H_2O ice grain size has significant impact on RMSE for location N. This is consistent with our results in section 3.3.2.

Table 3.8: Best fit parameter combinations for each Mars location. The H_2O ice at Location S is simulated as a mixture within the CO_2 snow, as opposed to a distinct layer.

Location S		**Location N**	
CO_2 ice grain size	1000 μm	H_2O ice grain size	250 μm
H_2O ice grain size	200 μm	CO_2 ice grain size	n/a
Amount of H_2O ice	0.07%	Amount of CO_2 ice	0%
Amount of dust	0.007%	Amount of dust	0.02%
RMSE	0.0676	RMSE	0.0542

Figure 3.15 and Figure 3.16 show the observed spectral albedo curves along with simulated curves using parameter values shown in Table 8. We observe an outlier point at 2.7 μm wavelength in the observed data for both locations and at all times. Albedo values at this wavelength are uncharacteristically higher than at nearby wavelengths, whereas both CO_2 and H_2O snows have very high absorptivity at this wavelength (Figure 3.3). This leads us to conclude that the high observed albedos at this wavelength are spurious, and may be due either to an artefact of the measuring spectrometer (CRISM), atmospheric anomalies associated with dust or clouds [*Brown et al*, 2010], and/or a calibration issue in the retrieval of surface reflectance at that wavelength.

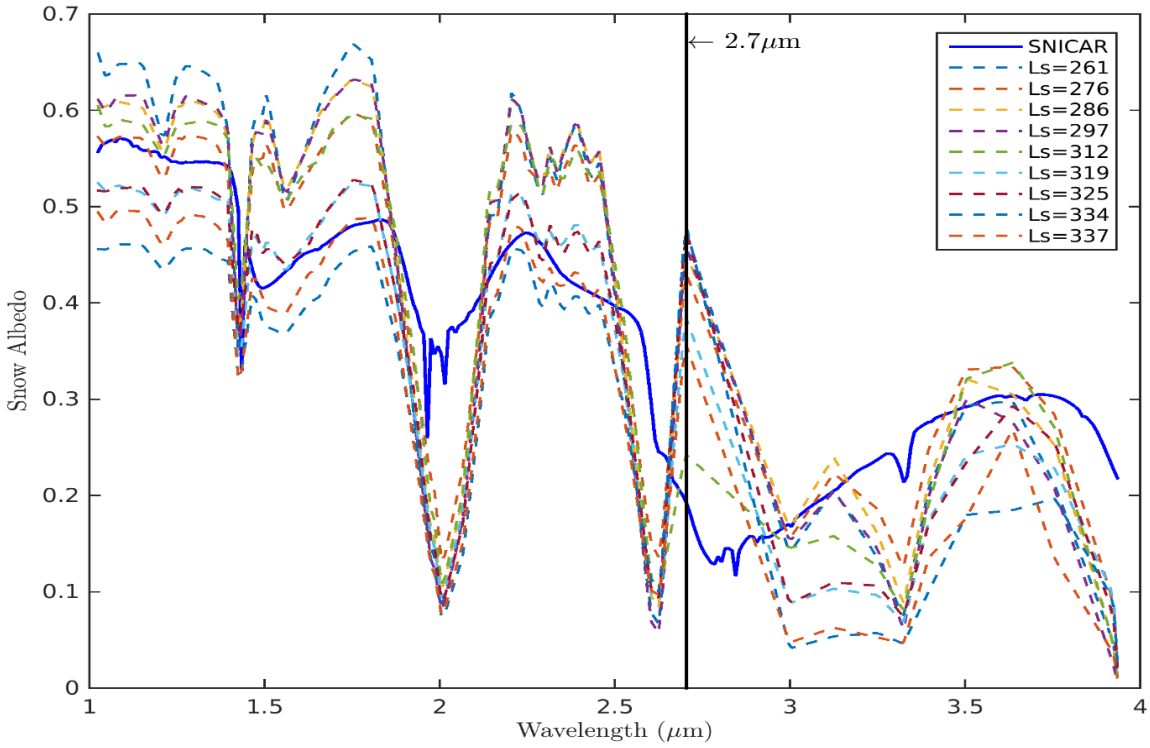

Figure 3.15: Observed albedo for location S (dotted curves) along with modeled albedo using best-fit parameters (solid blue curve). The black vertical line at 2.7 μm indicates the outlier described in the text.

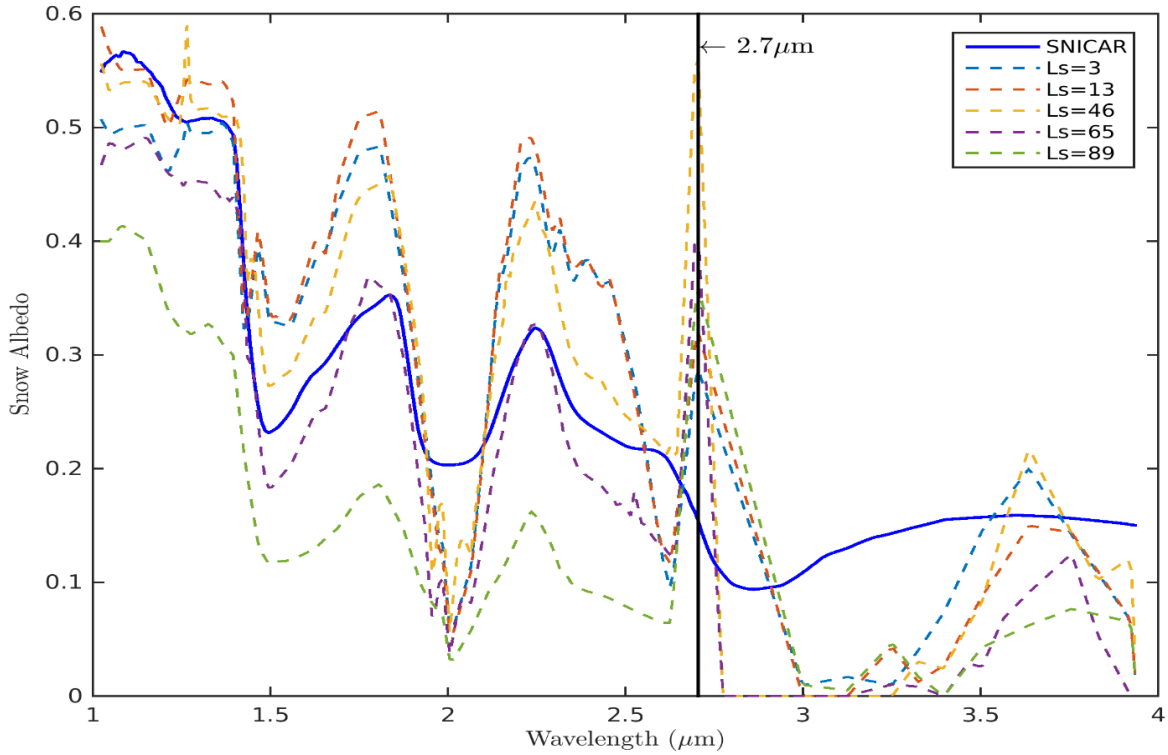

Figure 3.16: Same as fig. 15 but for location N

3.4.2 Comparison with OMEGA measurements

We also obtained spectral albedo for Observation 2621_1 (extracted at 65.3°N/341°E acquired at Ls = 2.4°) from the OMEGA instrument [Fig. 18 from *Appéré et al.,* 2011; shown later here], and modeled spectral albedo of CO_2 ice [Fig. 1 from *Appéré et al.,* 2011] simulated with a different radiative transfer model developed by *Douté and Schmitt* [1988]. Figure 3.17 shows the comparison of CO_2 snow albedo spectra from both models. The grain size applied in both models is 1 mm. The model used by *Appéré et al.,* [2011] shows weaker absorption in the key absorption bands (e.g., near 1.4 μm, 1.9 μm, and 3.3 μm), consistent with the use of optical constants in that study from *Quirico and Schmitt* [1997]. Updated CO_2 ice optical constants applied here were measured from thick samples [*Hansen,* 2005], which have significant advantages (described in detail by *Hansen,* 2005) over the measurements of optical constants conducted by *Quirico and Schmitt* [1997] using thin films. The differences in CO_2 snow spectral albedo simulated by these two models translates into a net spectrally-weighted RMSE of 0.090 for CO_2 snow. These differences, while not that large, could affect the determination of best-fit model parameters derived from observations.

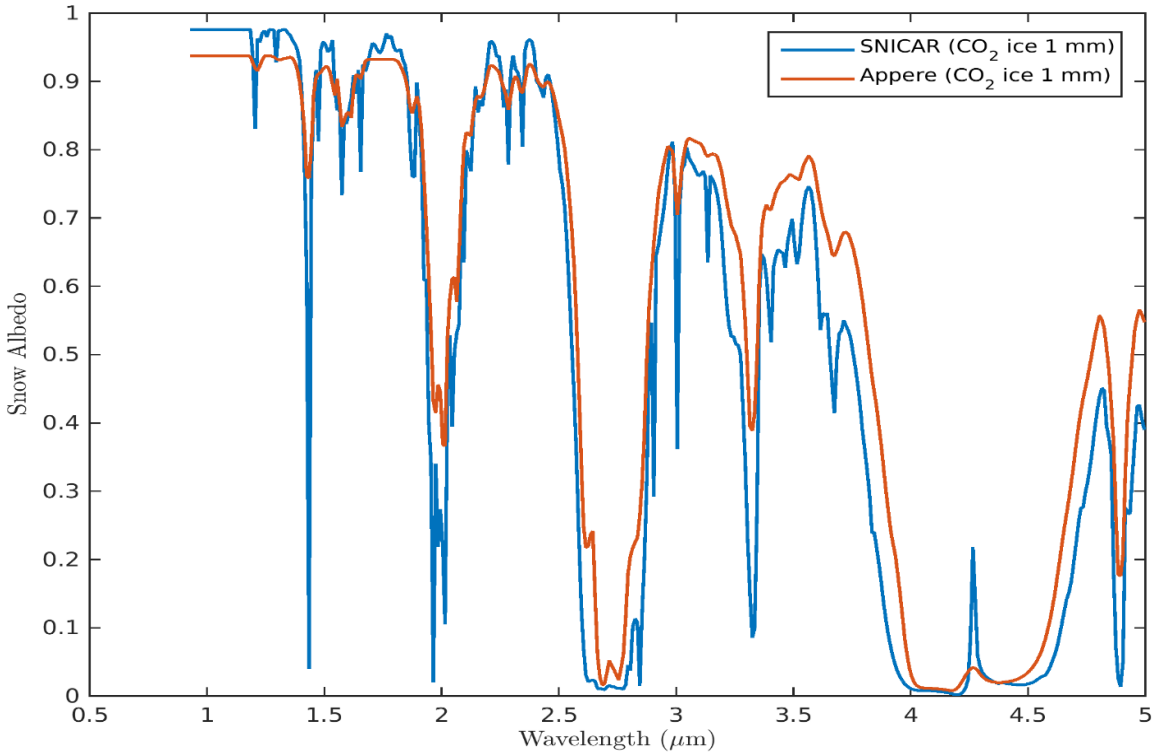

Figure 3.17: Comparison of CO_2 snow albedo simulated with SNICAR and shown in figure 1 of Appéré et al. [2011]. The snow grain size assumed in both models is 1mm.

Table 3.9: Comparison of best-fit parameters between SNICAR and Appéré et al., [2011]

	SNICAR	***Appéré et al.*, [2011]**
CO_2 ice grain size	3000 µm	7 cm
Amount of CO2 ice	99.83%	99.75%
H_2O ice grain size	100 µm	200 µm
Amount of H_2O ice	0.16%	0.19%
Dust grain size	1.5 µm	13 µm
Amount of dust	0.0094%	0.06%
RMSE	0.027	0.016

As shown in Table 3.9 and Figure 3.18, *Appéré et al.*, [2011] results are in good agreement with simulated near-IR snow albedo and OMEGA observations of a CO_2-rich deposit. This result was obtained by assuming a mixed CO_2/H_2O snow configuration with a CO_2 grain size of 7 cm, which interestingly is much larger than what is deemed to be realistic under most conditions [*Barr and Milkovich*, 2008]. We also obtained a reasonable agreement (spectrally-weighted RMSE of 0.027) with the OMEGA observations presented by *Appéré et al.*, [2011] using a mixed CO_2 and H_2O configuration of SNICAR applying a smaller CO_2 grain radius and slightly different mass fractions of dust and H_2O (Table 3.9; Figure 3.18). However, our results do not agree as well as that of *Appéré et al.* [2011]. Interestingly, the quality of our fit ceases to change much with larger grain sizes of CO_2 ice.

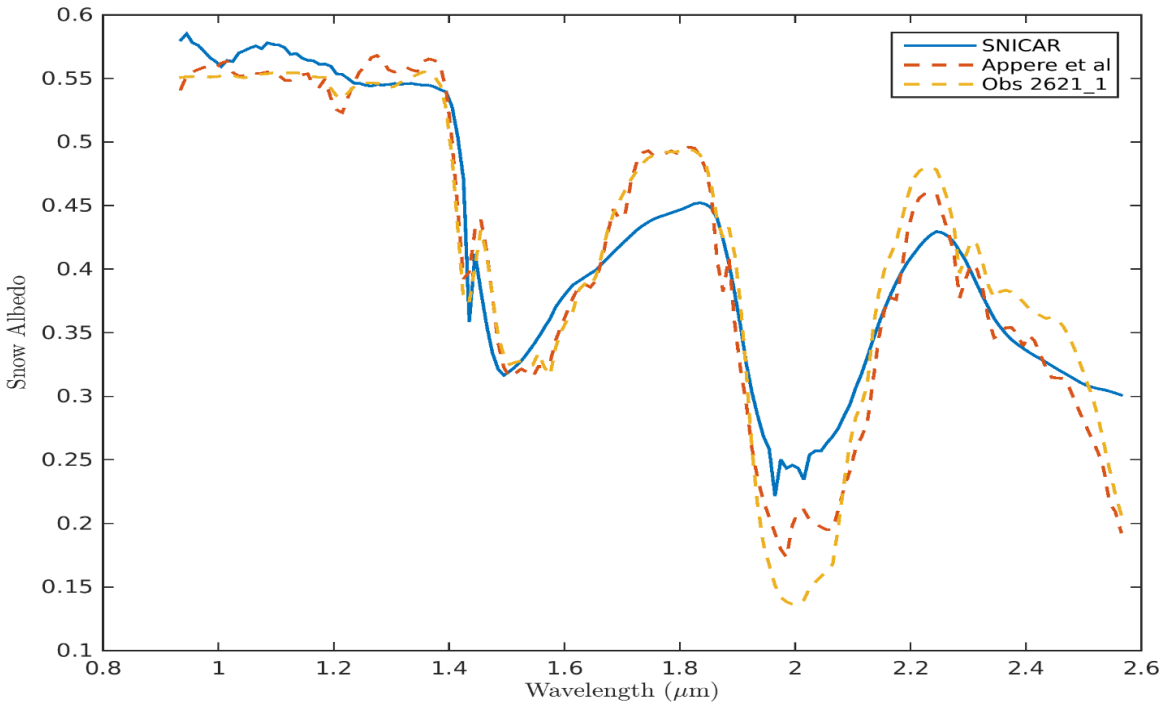

Figure 3.18: Comparison of best fit albedo using SNICAR and the model applied by Appéré et al., [2011] against data from OMEGA observation 2621_1.

3.5 Conclusions

We have simulated the spectral albedo of CO_2 snow using an enhanced 480-band version of SNICAR, which was previously developed for terrestrial snow. We explored CO_2 snow albedo across the entire solar spectrum, including UV, visible and near-IR wavelengths. Our analysis shows significant differences between H_2O and CO_2 snow albedos. H_2O snow is about 8 times more absorptive than CO_2 snow in the near-IR region, and 7 times more absorptive averaged over the entire solar spectrum. CO_2 snow albedo has very little dependence on solar zenith angle and a weaker dependence on grain size than H_2O snow. The broadband albedo of CO_2 snow decreases by only 0.064 as effective grain size increases from 50 to 1500 μm.

The presence of thin snow layers exposes underlying surfaces to incoming radiation, hence impacting the surface albedo. The saturation thicknesses for CO_2 snow and H_2O snow range from approximately 6.5 – 100 cm and 5 – 83 cm, respectively, for effective grain sizes ranging from 50 to 1500 μm, though we caution again that these thicknesses may be smaller with non-spherical ice particles. Non-spherical grains scatter less strongly in the forward direction, thereby decreasing the penetration depth of solar radiation. Thicker CO_2 snow is required to negate the impact of underlying surface because CO_2 ice grains scatter more strongly than H_2O ice grains, especially in the near-IR spectrum. The presence of 0.01% dust reduces the broadband albedo of CO_2 snow by about 50%, with Martian dust being the darkest type of dust explored here, followed by typical Earth dust and palagonite. The spectral shape of albedo changes caused by palagonite, which is often used as a Martian dust analog, closely follow those of Mars dust, but palagonite is not as

absorptive as Mars dust. The impact of dust on CO_2 snow albedo saturates after its mass mixing ratio exceeds roughly 0.1%.

Because of the contrasting properties of H_2O and CO_2 ice in the near-IR spectrum, different layering and mixing configurations of these types of snow can have substantial impact on net surface albedo. With an effective grain size of 100 μm, only about 2.5 cm of H_2O snow is needed to mask the influence of underlying CO_2 snow on net surface albedo (Table 3.5), while more than double this amount of CO_2 snow is needed to mask the influence of H_2O snow (Table 3.6). Such effects are relevant for the perennial H_2O ice caps of Mars, and where water vapor from the atmosphere condenses on top of CO_2 ice in other areas of the planet. When both snow types are present as a mixture rather than separate layers, 0.01% of H_2O snow reduces the broadband albedo of CO_2 snow by 0.03, while 1% of CO_2 snow is required to increase the broadband albedo of H_2O snow by the same amount.

With the identification of optimal snow parameter combinations, our results show a decent agreement between modeled and observed spectral albedo of the Martian polar ice caps in the 1–4 μm spectral range. The CRISM data exhibit anomalously high albedo at 2.7 μm, which cannot be explained with presence of either CO_2 or H_2O ice, as both media are highly absorptive at this wavelength. SNICAR also provides realistic best-fit parameters for matching OMEGA near-IR observations. Simulations presented here could potentially be used in combination with observed data to refine the calibration of surface albedo retrieval algorithms. This study also indicates that spectral albedo observations of the Martian cryosphere could be used in combination with inverse modeling to loosely infer parameters such as the amount of dust, presence of each ice type, and H_2O effective

grain size. Model results can also be used to interpolate measurements to higher spectral resolution. The new spectrally resolved albedos for CO_2 snow presented here have potentially wide applicability to any planet or system with CO_2 ice, especially Mars.

Chapter 4

Integration of SNICAR with LMD Mars GCM

4.1 Introduction

As discussed in the previous chapters, surface albedo plays an important role in any planet's energy budget and driving its climate system. Water-vapor, cloud and, albedo feedbacks are the three most powerful positive feedback mechanisms operating within the current climate system on Earth [e.g., *Bony et al.,* 2006; *Winton,* 2006; *Randall et al.*, 2007; *Soden et al.*, 2008; *Shell et al.*, 2008; *Flato et al.*, 2013]. Due to the small amounts of water-vapor on Mars (as compared to Earth), cloud (carbon dioxide) and albedo feedbacks are primary feedback mechanisms of climate change. Dust is a critical component of Martian climate, and plays an important role on the Martian climate [e.g., *Madeleine et al.*, 2011]. It can either amplify or weaken the other feedback mechanisms significantly.

Dust is tightly coupled with the other components of the climate system. Global dust storms can cause changes in meteorological phenomena (i.e., dust storms, dust devils, clouds, recession of the polar caps, and surface temperatures) that can persist for periods ranging from few weeks to more than one Mars year [*Cantor,* 2007]. The dust and CO_2 cycles have long been known to greatly affect the present-day climate of Mars. Although

dust cycles are highly variable on the Mars, CO_2 condensation cycle is highly repeatable on multi-annual timescales [*Hess et al.,* 1980]. The dust and CO_2 cycles on Mars show no correlation between them [e.g., *Kahre and Haberle,* 2010]. Viking landers measurements (VL-1 and VL-2) show a highly repeatable CO_2 cycle on multi-annual timescales [*Hess et al.,* 1980], while demonstrating a highly variable dust cycle (including large dust storms) over the years [e.g., *Zurek and Martin,* 1993]. Snow albedo is largely affected by the amount of impurity present in it.

Current version of LMD Mars GCM (hereafter MGCM) uses annually repeating albedo values from the Thermal Emission Spectrometer (TES) observations. These observations also show significant seasonal variation of snow (both H_2O and CO_2) albedo [*Kieffer et al.,* 2000; *Kieffer and Titus,* 2001]. Small changes in albedo would have compelling impact on the climate dynamics, especially for very low pressure (<1% of Earth's atmosphere) atmosphere of Mars. Therefore, it is important to prognostically determine ice cap (both H_2O and CO_2) albedos interactively in real-time inside the model.

4.2 Methodology

We apply the extended SNICAR model (chapter 3) to the current version of MGCM to calculate real-time interactive surface broadband snow albedo. Extended version of SNICAR utilizes 480 bands spanning 0.2-5.0 μm at 10 nm spectral resolution. We divide our broadband (0.2-5.0 μm) into two sub-regions (0.2-0.5 μm and 0.5-5.0 μm) which are used for atmospheric radiative transfer calculations in original MGCM. These band-averaged values are weighted with solar spectral irradiance measurements from *Labs and Neckel* [1968]. We determine the optical properties of Martian dust [*Wolff* et al., 2006; *Wolff* et al., 2009; *Wolff* et al., 2010] using Mie Theory with an assumed gamma size

distribution [*Hansen and Travis*, 1974] with r_{eff}=1.5μm and effective variance (υ_{eff})=0.3 [*Wolff* et al., 2006] (chapter 3, section 3.2). SNICAR replaces the original scheme which used a simple prescribed surface albedo. SNICAR coupled with MGCM calculates surface albedo interactively using prognostic surface dust deposition flux (already present in the model) as an input. As pure snow albedos are much higher than observed albedos, first step in this process was to determine a base amount of dust to bound simulated albedos within realistic limits. First the original model was run for a long-term with dust accumulation throughout. The dust amount at the time-step for which minimum difference between TES observed albedo and modeled albedo is achieved is used as a "baseline dust" for model initialization. This albedo difference was minimized only for snow-covered regions.

Next step in the process was to have realistic amount of dust in snow for long duration model runs. Dust exchange on Martian surface is caused by the winds around the entire planet. We used an exponential decay mechanism to achieve consistent dust amount in ice caps. For a given time *'t'*, net concentration of dust in snow $d(t)$ at the surface is given by:

$$d(t) = \left[d(t-1) + d_0\right] e^{-t_0/\tau} \tag{4.1}$$

where 'd_0' is the dust deposition flux calculated by original MGCM for that time step, 't_0' is the physical time-step (1/48 sol; 1 sol = 88775 seconds) of model run, and 'τ' is the decay constant. For t = 0, we use baseline dust to represent $d(t-1)$. To calculate the value of 'τ', first we run the model for one Martian Year (MY) without any decay mechanism. Next, we replace $d(t)$ with average baseline dust determined earlier, $\left[\left(d(t-1) + d_0\right)\right]$ with average model accumulated dust at the end of run, and 't_0' with the

total run-time (in seconds) of the model. We found the value of 'τ' to be equal to 1.36×10^8 seconds (~1528 sols) using this technique.

Finally, the new version of SNICAR was implemented in MGCM to provide higher resolution, and more precise albedo simulations for snow/ice covered surface. We also determine the impact of cryosphere and dust on shortwave energy flux of the Mars. We assume zero change in all physical quantities at non-snow covered regions for all scenarios in this chapter. Therefore changes over non-snow covered regions are not plotted in any maps. All global average parameters are area-weighted means for that particular quantity.

4.3 Results and Discussion

Figure 4.1 shows the global annual mean surface albedos for various scenarios on Mars. Snow-free albedo is bare ground albedo (prescribed in the model) without the presence of any snow. Dust-free albedo is pure snow albedo, and original MGCM albedo is simulated using original version of MGCM (without SNICAR). SNICAR albedo (global annual mean) is the albedo computed after the integration of SNICAR into the MGCM. This results in an albedo that has a correlation of 0.999 with original MGCM albedo. Dust-free and snow-free albedos are derived from diagnostic dust-free and snow-free albedo calculations respectively within MGCM. These diagnostic calculations do not affect the simulated climate state. The global annual mean values are not far apart for both original MGCM and SNICAR scenarios (Table 4.1). Table 4.1 also presents mean albedo values calculated over snow-covered surface only. Dust-free albedos are much higher than the SNICAR albedo due to the presence of high amount of dust within snow (chapter 3, section 3.3.5). Also CO_2 snow is more susceptible to dust darkening as compared to H_2O snow, especially in the near-IR spectral region (chapter 3, section 3.3.4).

Table 4.1: 7-year global annual mean albedo for various scenarios on Mars. First row correspond to values plotted in Figure 4.1. All means are area-weighted.

Scenario	SNICAR	Original MGCM	Dust-free	Snow-free
Mean Albedo (Global)	0.24	0.23	0.3	0.2
Mean Albedo (Snow-covered)	0.34	0.33	0.63	0.21

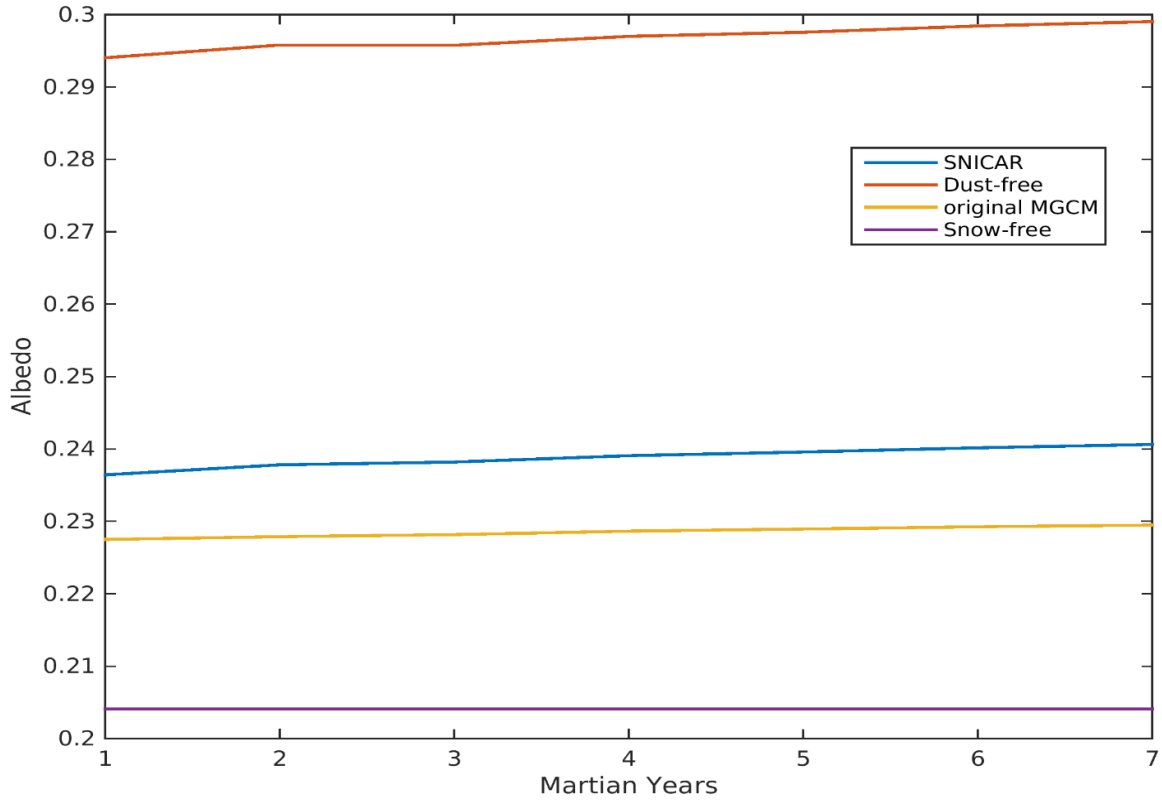

Figure 4.1: Annual global mean surface albedo of Mars calculated for various scenarios.

4.3.1 Comparison between SNICAR and MGCM simulations

Figure 4.2 shows the global map of difference in albedo simulated using SNICAR and original MGCM. Difference is taken by subtracting MGCM annual mean values from SNICAR annual mean values. In general, SNICAR albedos are higher than MGCM albedos near poles while smaller near mid-latitudes. MGCM simulates much higher dust deposition near mid-latitudes as compared to poles (Figure 4.3), resulting in lower snow albedo simulated by SNICAR. This effect was not present in original version of MGCM because the albedo was insensitive to the dust variability on surface. Dust deposition flux in Figure 4.3 is consistent with the original MGCM generated dust flux, although the distribution has been amplified due to baseline dust used with SNICAR implementation. Figure 4.4 shows the variation of albedo difference, dust deposition flux and net surface wind speed. We estimate a high correlation coefficient of 0.69 between wind speed and dust deposition flux. This indicates that the wind pattern is primary cause for specific dust distribution features. Albedo changes also follow the similar distribution as dust deposition flux (positive with lower dust concentration and negative with higher dust concentration), especially in Northern Hemisphere. We observe a relatively higher change in albedo in Southern Hemisphere due to higher abundance of CO_2 ice [e.g., *Kieffer et al.*, 2000], which is brighter than H_2O ice (chapter 3). These changes in albedo significantly impact the shortwave flux, especially at the surface (Figure 4.5). After SNICAR integration, we estimate global annual mean change in albedo and shortwave flux (at surface) of -0.0053 and 0.47 W/m^2 respectively from original MGCM.

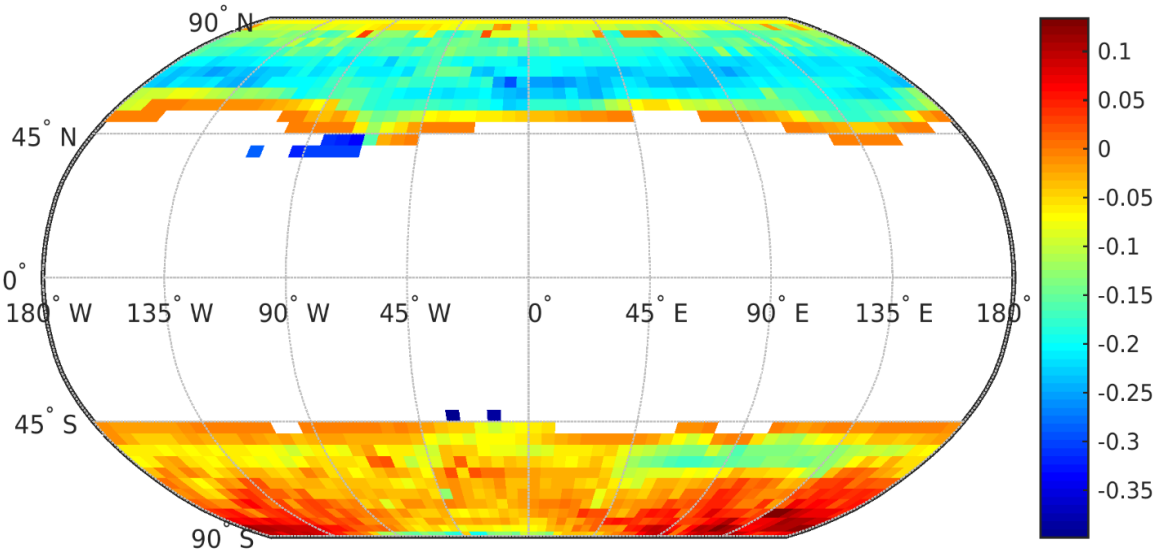

Figure 4.2: Global map of mean albedo difference between SNICAR and MGCM (mean SNICAR albedo – mean MGCM albedo).

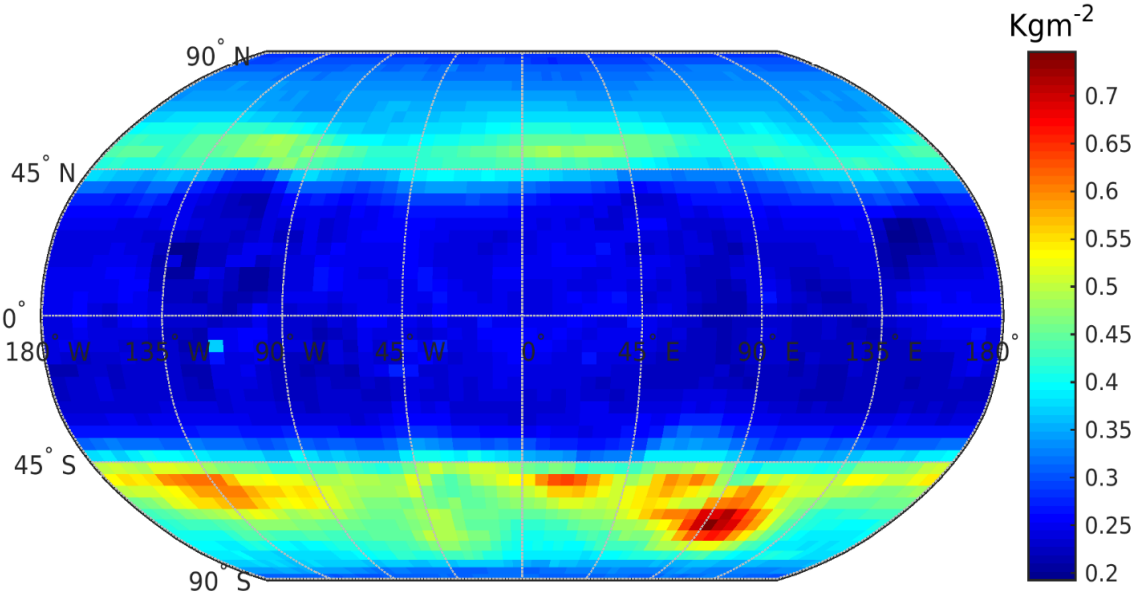

Figure 4.3: Global map of 7-years annual mean dust deposition on Mars surface.

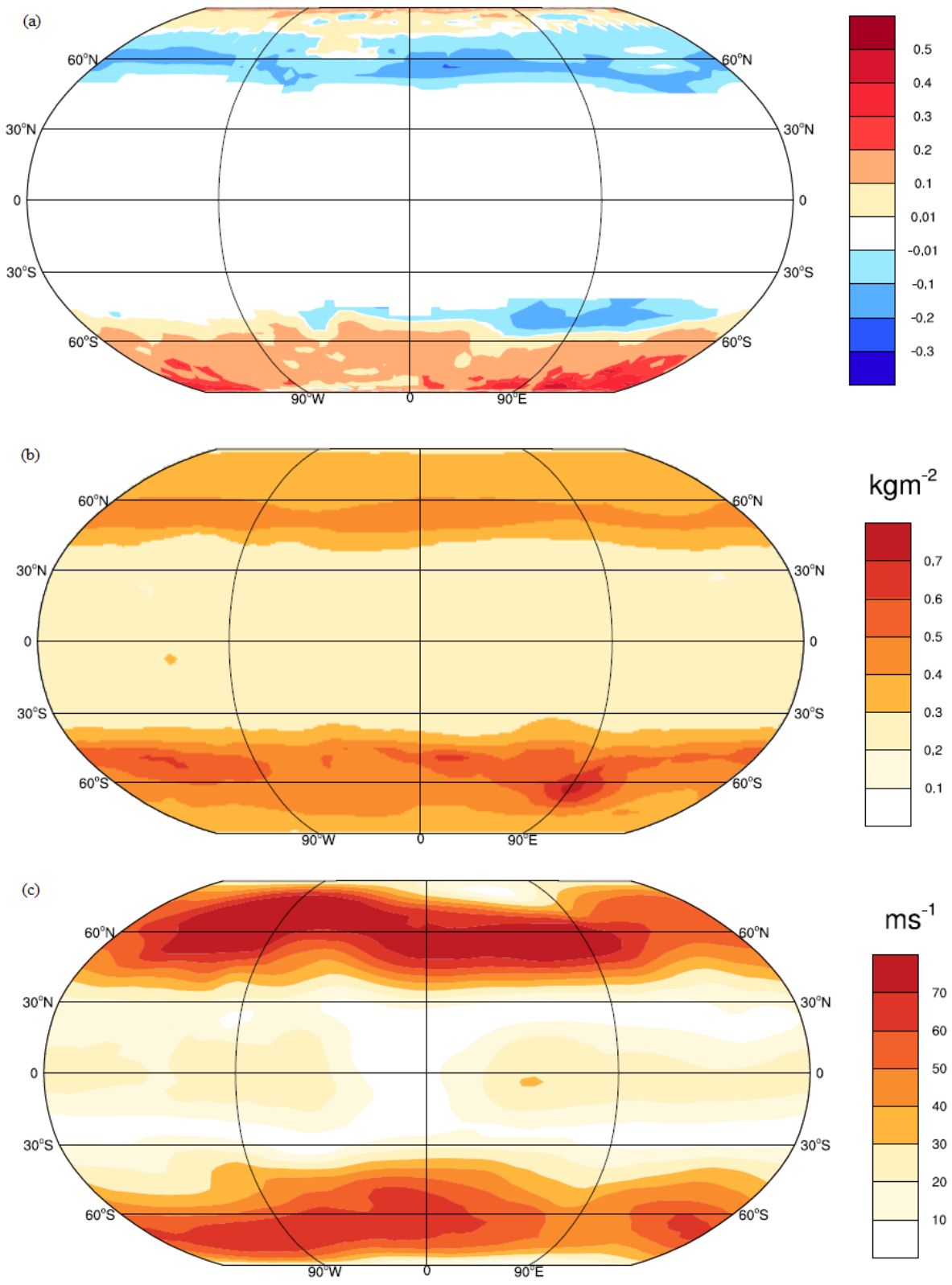

Figure 4.4: Annual mean maps highlighting (a) albedo difference (re-plot of Fig. 4.2); (b) net dust deposition flux (re-plot of Fig. 4.3); (c) absolute surface wind speed.

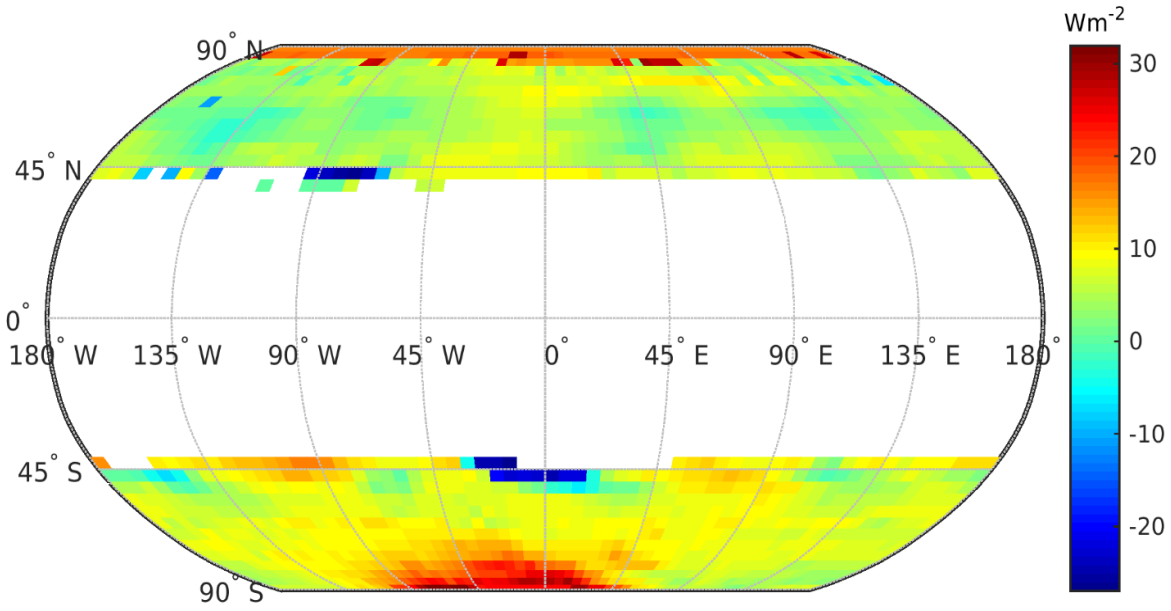

Figure 4.5: Global map of mean shortwave flux difference at the surface between SNICAR and MGCM (mean SNICAR albedo – mean MGCM albedo).

4.3.2 Comparison between snow-covered and snow-free scenarios

After integrating SNICAR into the MGCM, we estimate the impact of cryosphere on Martian albedo and shortwave energy flux. Both snow-free and snow-covered simulations are done with baseline dust and model generated dust deposition flux present within the system. Net concentration of dust in snow is determined using Equation 4.1. Figure 4.6 shows the global map of difference of bare ground albedos from snow-covered albedos. Few grid-points near mid-latitudes show a slightly higher albedo for bare ground as compared to snow-covered albedo. In these regions snowfall frequency and amount are both lower as compared to Polar Regions. A high concentration of dust within small amount of snow can decrease the surface albedo significantly, and bring it lower than the actual bare ground albedo. Also, the strong absorption features of CO_2 snow at various wavelengths disappear with high dust concentrations (chapter 3, section 3.3.5). Figure 4.6 shows the changes in shortwave energy flux at surface between snow-covered and snow-

free scenarios. On Mars, cryosphere causes a global annual mean change of 0.015 and -0.27 W/m^2 in albedo and shortwave flux (at surface) respectively.

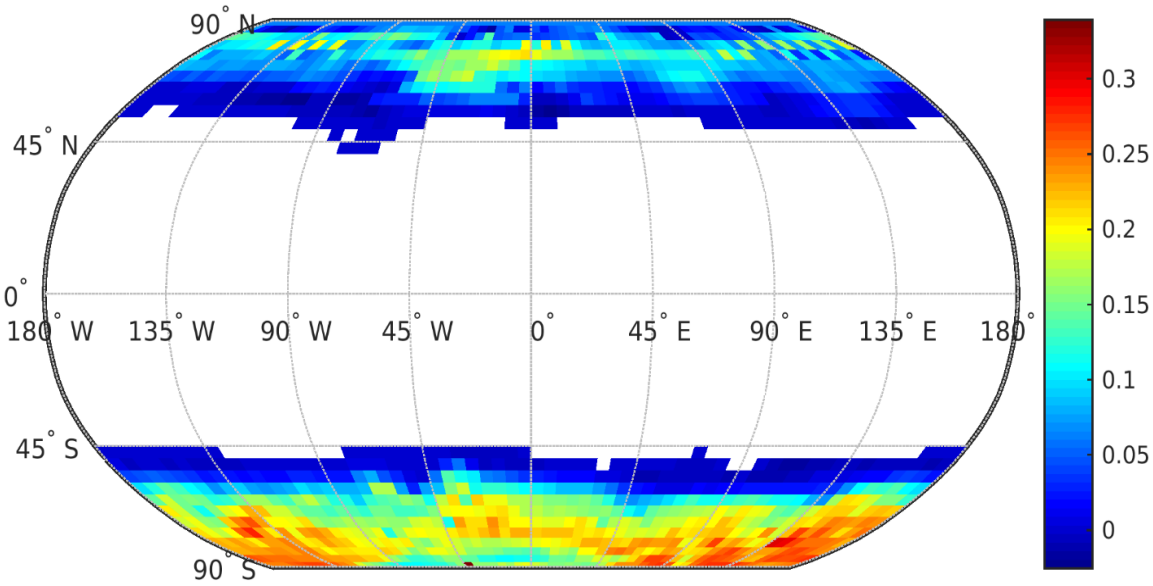

Figure 4.6: Global map of mean albedo difference between snow-covered and snow-free albedo

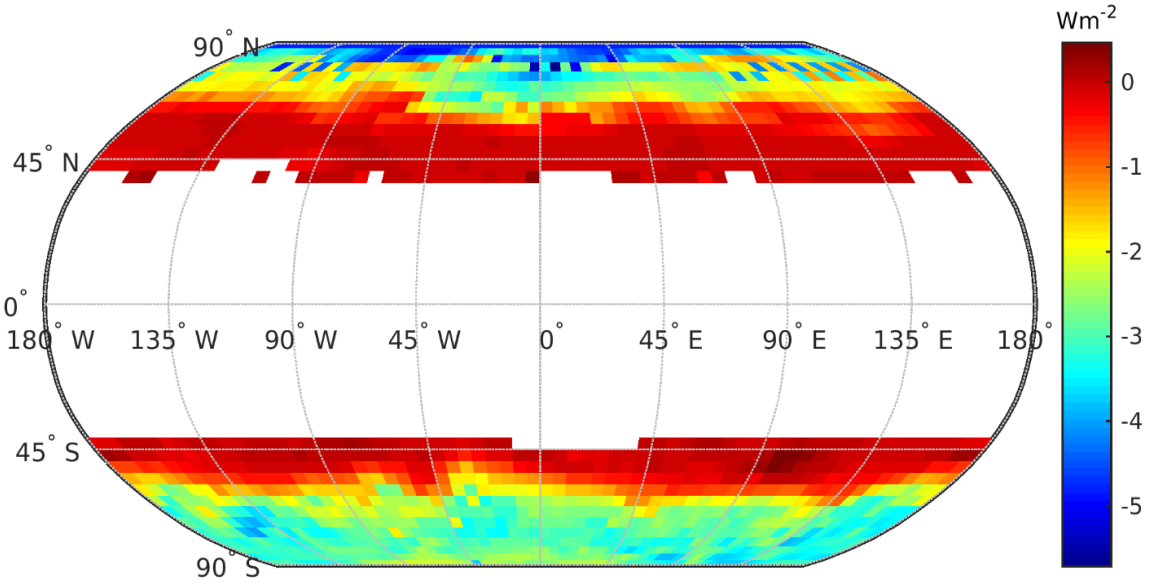

Figure 4.7: Global map of mean shortwave flux difference at the surface between snow-covered and snow-free scenarios using SNICAR.

4.3.3 Impact of dust

Next we calculate the impact of dust darkening on Martian snow albedo and shortwave energy flux. Net global annual mean dust-free albedo is higher by about 0.06 than the actual albedo calculated using SNICAR (Figure 4.8). Differences are negligible near the cap edge due to scarcity of snow. Except for those edges, albedo change is higher near mid-latitudes as compared to poles. This happens due to decrement in dust amount from mid-latitudes to poles (Figure 4.4b). Dust causes a global annual mean change of 0.41 W/m^2 in shortwave flux at the surface (Figure 4.9). Change caused by dust in snow is higher (absolute values) than the snow+dust cryosphere itself. This indicates the importance of dust in the Martian climate system.

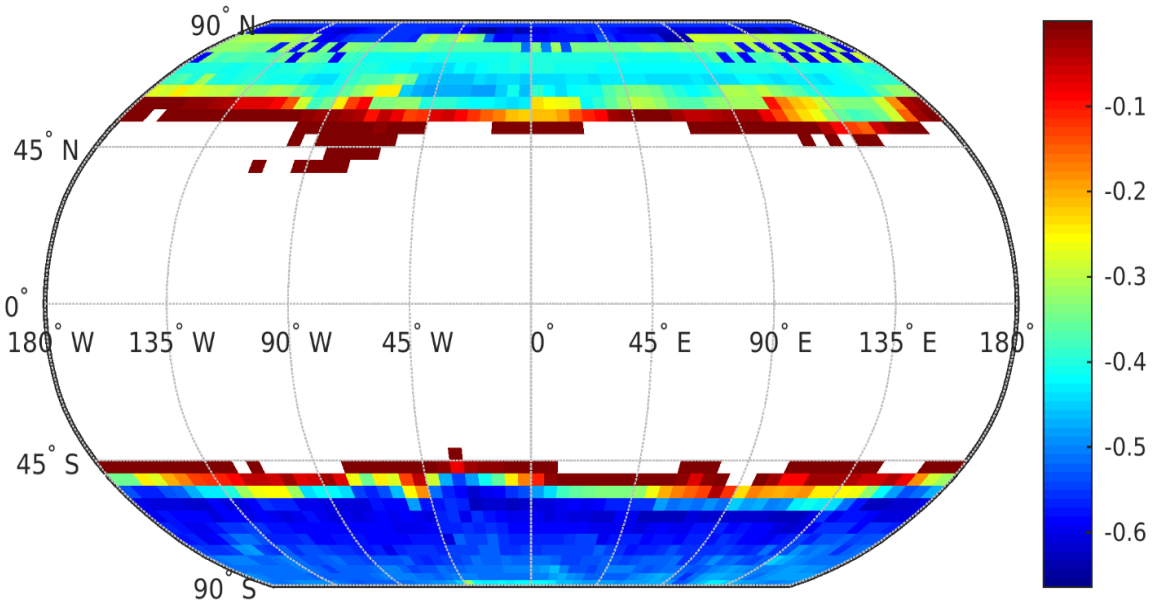

Figure 4.8: Global map of mean albedo difference between SNICAR albedo and dust-free albedo.

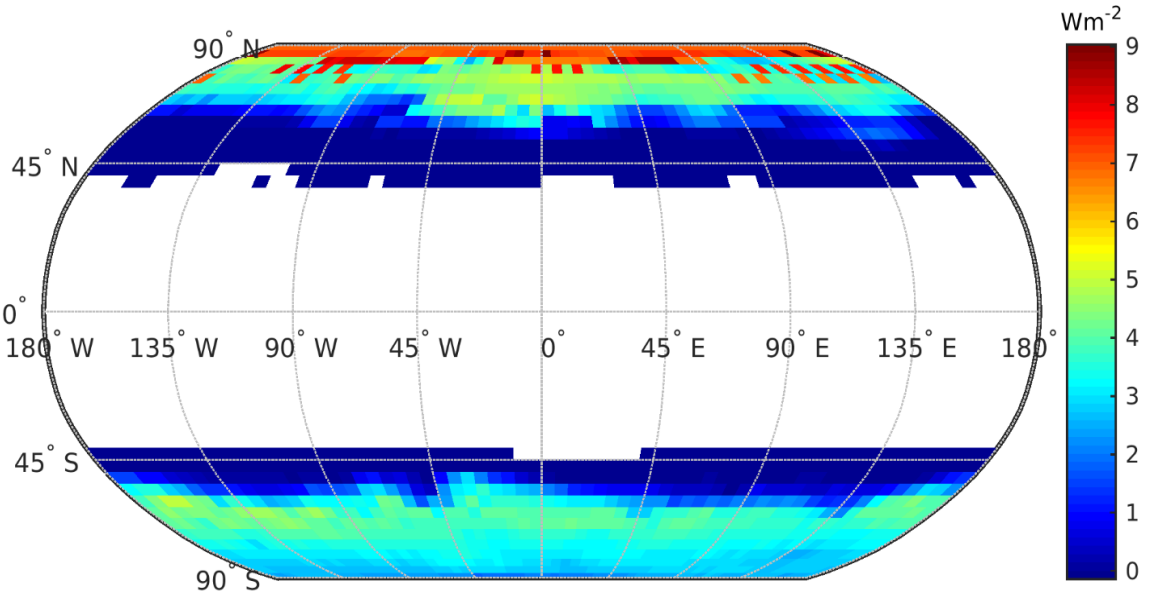

Figure 4.9: Global map of mean shortwave flux difference at the surface between SNICAR albedo and dust-free scenarios using SNICAR.

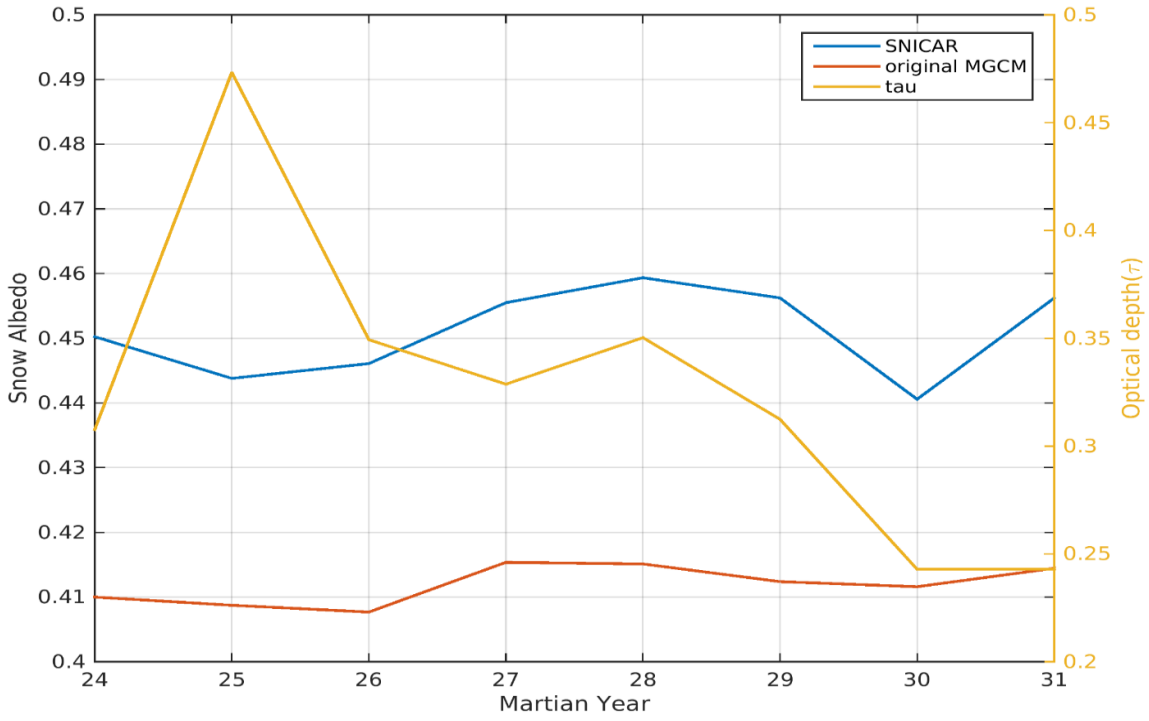

Figure 4.10: Global annual mean of snow albedos using SNICAR and MGCM, and optical depth of dust for various Martian years.

Finally, we run the MGCM for various Martian Years (MY24 – MY31) separately using different initial conditions specific to each year shown in Figure 4.10. We initially observe that the original MGCM albedos are not very sensitive to dust optical depth over the years. We observe a higher sensitivity of albedo with dust with SNICAR integrated into the model. We achieved a correlation of 0.64 with SNICAR as compared to 0.5 with original MGCM (both values are absolute). MY30 has some issues (yet to be determined) with SNICAR integrated run, and therefore not included in the correlation calculations for either cases.

4.4 Conclusions

We successfully integrated SNICAR into the current version of the MGCM. We use an initial dust content to constrain the surface albedo within realistic boundaries for Mars. We also use an exponential decay method to release dust on the surface over time. Although the new SNICAR integrated model produces slightly higher albedo than the original MGCM, it generates albedos with higher sensitivity to surface dust content as compared to original MGCM. In some cases SNICAR albedo is smaller because of higher dust in that region. Changes in albedo and surface dust content also impact the shortwave energy flux at the surface. SNICAR integrated model simulates a change of 0.47 W/m^2 in shortwave flux. We observe a high dependency (correlation coefficient = 0.69) of dust deposition at surface with surface wind speed. Changes in albedo also show the similar distribution as dust concentration over the globe.

Real snow albedos are much lower than the dust-free albedos due to the high amount of dust deposition on Mars, and higher susceptibility of CO_2 snow albedo to dust darkening as compared to H_2O snow. Dust is one of the key elements in determining the climate state

of Mars. The impact caused by dust is about 1.5 times (absolute values) of the impact caused by the presence of snow itself on shortwave flux at the surface. Runs with different initial conditions for various years show higher correlation between dust optical depth and surface albedo with the SNICAR integrated model. There are some minor technical issues which are yet to be resolved. We are hopeful that these issues will be resolved soon, and we will be able to include SNICAR in the new version of MGCM.

Chapter 5

Conclusions and Future Work

5.1 Summary of Results

Due to the strong feedback effect of ice-albedo on planetary climate systems, it is necessary to accurately account for this effect for producing realistic climate simulations on Earth and Mars. Being a strong feedback mechanism, albedo feedback can significantly delay or amplify a global seasonal change like melting of glaciers on Earth, CO_2 snow cover on Mars etc.

In Chapter 2, we apply measurements from the MODIS, combined with microwave retrievals of snow presence and radiative kernels produced from 4 different models, to derive CrRE over global land during 2001–2013. We estimate global annual mean land CrRE during this period of –2.6 W/m^2, with variations from –2.2 to –3.0 W/m^2 resulting from use of different kernels, and variations of –2.4 to –2.6 W/m^2 resulting from different algorithmic determinations of snow presence and surface albedo. Slightly more than half of the global land CrRE originates from perennial snow on Antarctica, whereas the majority of the northern hemisphere effect originates from seasonal snow. Mountain glaciers resolved in 0.05 degree MODIS data contribute about –0.037 W/m^2 (1.4%) of the global effect, with the majority (94%) of this contribution originating from the Himalayas. During a common overlap period of 2001–2008, our MODIS estimates of the northern hemisphere land CrRE are about 18% smaller (less negative) than previous estimates

derived from coarse-resolution AVHRR data, though inter-annual variations are well correlated (r=0.78), indicating that these data are useful in determining longer term trends in land CrRE.

In Chapter 3, we adapt the terrestrial SNICAR model to simulate CO_2 snow albedo across the ultraviolet, visible, and near-IR spectrum (0.2-5.0 μm). We apply recent laboratory derived refractive indices of CO_2 ice, which produce higher broadband CO_2 snow albedo (0.93–0.98) than previously estimated. Compared with H_2O snow, we find that CO_2 snow albedo is much higher in the near-IR spectrum, less dependent on ice grain size, less dependent on solar zenith angle, and more susceptible to darkening from dust. The presence of small amounts of H_2O snow on top of CO_2 snow can substantially decrease the surface albedo. Whereas 2.5 cm of H_2O snow (with 100 μm grain-size) can completely mask the impact of underlying CO_2 ice or the surface, roughly twice as much overlying CO_2 snow is required to mask underlying H_2O snow. Similarly, a 10% mixing ratio of H_2O ice embedded in CO_2 snow decreases broadband albedo by 0.18 (relative to pure CO_2 snow), while 10% CO_2 ice elevates H_2O snow broadband albedo by 0.10. We also achieve a reasonable agreement between modeled and observed Martian spectral surface albedo in the near-IR.

In Chapter 4, we successfully integrate the extended SNICAR model into the current version of MGCM to calculate real-time interactive surface broadband snow albedo. We use an initial dust content to constrain the surface albedo within realistic boundaries for Mars, and an exponential decay method to release surface dust over time. The SNICAR integrated model simulates a change of 0.47 W/m^2 in shortwave flux as compared to original MGCM. Real snow albedos are much lower than the dust-free albedos due to high

amount of dust deposition included with SNICAR implementation, and higher susceptibility of CO_2 snow to darkening as compared to H_2O snow. We estimate that the impact caused by dust is about 1.5 times (absolute values) of the impact caused by the presence of snow in shortwave flux at surface. Runs with different initial conditions for various years show higher correlation between albedo variation and dust opacity with SNICAR integrated model.

5.2 Future Work

This thesis opens multiple research topics which I plan to explore in future. In Chapter 4, we observe some technical issues occurring with SNICAR integrated MGCM for some specific initial conditions for long term runs of the model. These issues are most likely caused by erroneous dust deposition simulations on the surface within the model. I plan to resolve these issues as soon as possible so that we can release SNICAR integrated MGCM to the public.

I would also be interested in improving other aspects of MGCM that are dependent on snow/ice coverage of Mars. Dust in Mars's climate system significantly impacts (both darkening and brightening) the planetary albedo. Large global dust storms put enough dust in the air to completely cover the planet and block out the sun, hence largely affecting the planetary energy exchange with Sun and outer space. Although MGCM captures several aspects of the current Mars climate, they require further improvements to better understand surface albedo and emissivity feedbacks and thus to accurately determine the energy balance of the planet at any given time. Therefore, I would like to investigate the coupling of the dust, CO_2, and water cycles through surface albedo and emissivity feedbacks using variability of albedo feedback, radiative cooling, and adiabatic cooling caused by presence

of dust. Additionally, I would also like to explore the impact of these processes on present-day climate system of Mars. Improving planetary climate model is the key to better understand the evolution of, and to predict the future events of any planet.

Bibliography

Appéré, T., B. Schmitt, Y. Langevin, S. Douté, A. Pommerol, F. Forget, A. Spiga, B. Gondet, and J.-P. Bibring (2011), *Winter and spring evolution of northern seasonal deposits on Mars from OMEGA on Mars Express,* J. Geophys. Res., 116, E05001, doi:10.1029/2010JE003762.

Balkanski, Y., M. Schulz, T. Claquin, and S. Guibert (2007), *Reevaluation of Mineral aerosol radiative forcings suggests a better agreement with satellite and AERONET data,* Atmospheric Chemistry and Physics, 7(1), 81-95.

Banin, A., F. X. Han, I. Kan, and A. Cicelsky (1997), *Acidic volatiles and the Mars soil,* J. Geophys. Res., 102(E6), 13341–13356, doi:10.1029/97JE01160.

Barr, A. C., and S. M. Milkovich, (2008), *Ice grain size and the rheology of the martian polar deposits,* Icarus, 194(2), 513-518, doi:10.1016/j.icarus.2007.11.018.

Baum, W. A. (1974), *Earth-based observations of Martian albedo changes*. Icarus, 22(3), 363-370.

Bell III, J. F. (1996), *Iron, sulfate, carbonate, and hydrated minerals on Mars, in " Mineral Spectroscopy: A Tribute to Roger G. Burns,*" Geochemical Society Special Publication 5 (MD Dyar, C. McCammon, and MW Schaefer, eds.), 359-380.

Bell III, J. F., T. B. McCord, and P. D. Owensby (1990), *Observational evidence of crystalline iron oxides on Mars,* J. Geophys. Res., 95(B9), 14447–14461, doi:10.1029/JB095iB09p14447.

Bertaux, J. L., et al., (2007), *A warm layer in Venus' cryosphere and high-altitude measurements of HF, HCl, H_2O and HDO,* Nature, 450(7170), 646-649.

Bibring, J. P., Y. Langevin, A. Gendrin, B. Gondet, F. Poulet, M. Berthé, A. Soufflot, R. Arvidson, N. Mangold, J. Mustard, and P. Drossart (2005), *Mars surface diversity as revealed by the OMEGA/Mars Express observations,* Science, 307(5715), 1576-1581.

Bibring, J. P., Y. Langevin, F. Poulet, A. Gendrin, B. Gondet, M. Berthé, A. Soufflot, P. Drossart, M. Combes, G. Bellucci, and V. Moroz (2004), *Perennial water ice identified in the south polar cap of Mars,* Nature, 428(6983), 627-630.

Bonev, B. P., G. B. Hansen, D. A. Glenar, P. B. James, and J. E. Bjorkman (2008), *Albedo models for the residual south polar cap on Mars: Implications for the stability of the cap under near-perihelion global dust storm conditions,* Planetary and Space Science, 56(2), 181-193, doi:10.1016/j.pss.2007.08.003

Bony, S. et al. (2006), *How Well Do We Understand and Evaluate Climate Change Feedback Processes?,* J. Climate, 19, 3445–3482. doi: 10.1175/JCLI3819.1.

Box, J. E., X. Fettweis, J. C. Stroeve, M. Tedesco, D. K. Hall, and K. Steffen, (2012), *Greenland ice sheet albedo feedback: thermodynamics and atmospheric drivers,* The Cryosphere, 6, 821-839, doi:10.5194/tc-6-821-2012.

Brown, A. J., S. Piqueux, and T. N. Titus, (2014), *Interannual observations and quantification of summertime H2O ice deposition on the Martian CO_2 ice south polar cap,* Earth and Planetary Science Letters, 406, 102-109.

Brown, A. J., W. M. Calvin, and S. L. Murchie (2012), *Compact Reconnaissance Imaging Spectrometer for Mars (CRISM) north polar springtime recession mapping: First 3 Mars years of observations,* J. Geophys. Res., 117, E00J20, doi:10.1029/2012JE004113.

Brown, A. J., W. M. Calvin, P. C. McGuire, and S. L. Murchie (2010), *Compact Reconnaissance Imaging Spectrometer for Mars (CRISM) south polar mapping: First Mars year of observations,* J. Geophys. Res., 115, E00D13, doi:10.1029/2009JE003333.

Brown, R. D., and D. A. Robinson, (2011), *Northern hemisphere spring snow cover variability and change over 1922-2010 including an assessment of uncertainty,* The Cryosphere, 5 (1), 219-229, doi:10.5194/tc-5-219-2011.

Buratti, B., and J. Veverka, (1984), *Voyager photometry of Rhea, Dione, Tethys, Enceladus and Mimas,* Icarus, 58(2), 254-264.

Byrne, S., M. T. Zuber, and G. A. Neumann (2008), *Interannual and seasonal behavior of Martian residual ice-cap albedo,* Planetary and Space Science, 56(2), 194-211.

Cantor, B. A. (2007), *MOC observations of the 2001 Mars planet-encircling dust storm,* Icarus, 186(1), 60-96, doi:10.1016/j.icarus.2006.08.019

Cao, Y., S. Liang, X. Chen, and T. He, (2015), *Assessment of Sea Ice Albedo Radiative Forcing and Feedback over the Northern Hemisphere from 1982 to 2009 Using Satellite and Reanalysis Data,* J. Clim., 28, 1248–1259. doi: 10.1175/JCLI-D-14-00389.1.

Chapman, W. L., and J. E. Walsh, (2007), *A synthesis of Antarctic temperatures,* J. Clim. 20 (16), 4096-4117, doi:10.1175/JCLI4236.1.

Chesley, S. R., P. W. Chodas, A. Milani, G. B. Valsecchi, and D. K. Yeomans, (2002), *Quantifying the risk posed by potential Earth impacts*, Icarus, 159(2), 423-432.

Christensen, P. R. (1988), *Global albedo variations on Mars: Implications for active aeolian transport, deposition, and erosion,* J. Geophys. Res., 93(B7), 7611–7624, doi:10.1029/JB093iB07p07611.

Christensen, P. R., et al., (2000), *Detection of crystalline hematite mineralization on Mars by the Thermal Emission Spectrometer: Evidence for near-surface water,* J. Geophys. Res., 105(E4), 9623–9642, doi:10.1029/1999JE001093.

Christensen, P. R., et al., (2001a), *Mars Global Surveyor Thermal Emission Spectrometer experiment- Investigation description and surface science results,* J. Geophys. Res., 106(E10), 23823–23871, doi:10.1029/2000JE001370.

Christensen, P. R., R. V. Morris, M. D. Lane, J. L. Bandfield, and M. C. Malin (2001b), *Global mapping of Martian hematite mineral deposits: Remnants of water-driven*

processes on early Mars, J. Geophys. Res., 106(E10), 23873–23885, doi:10.1029/2000JE001415.

Clancy, R. T., S. W. Lee, G. R. Gladstone, W. W. McMillan, and T. Roush (1995), *A new model for Mars atmospheric dust based upon analysis of ultraviolet through infrared observations from Mariner 9, Viking, and Phobos,* J. Geophys. Res., 100, 5251–5264.

Clark, R. N., T. V. King, M. Klejwa, G. A. Swayze, and N. Vergo (1990), *High spectral resolution reflectance spectroscopy of minerals,* J. Geophys. Res., 95(B8), 12653–12680, doi:10.1029/JB095iB08p12653.

Cruikshank, D. P. (1980), *Near-infrared studies of the satellites of Saturn and Uranus,* Icarus, 41(2), 246-258.

Cruikshank, D. P., et al., (2015), *The surface compositions of Pluto and Charon,* Icarus, 246, 82-92.

Derksen, C., R. Brown, L. Mudryk, K. Luojus (2014), *Terrestrial Snow Cover [in Arctic Report Card 2014],* http://www.arctic.noaa.gov/reportcard.

Dery, S. J., and R. D. Brown, (2007) *Recent Northern Hemisphere snow cover extent trends and implications for the snow-albedo-feedback,* Geophys. Res. Lett., 34, L22504, doi:10.1029/2007GL031474.

Ding, Q., E. Steig, D. Battisi, and M. Kuttel (2011), *Winter warming in West Antarctica caused by central tropical Pacific warming,* Nature Geoscience 4, 398-403, doi:10.1038/ngeo1129.

Douté, S., and B. Schmitt (1998), *A multilayer bidirectional reflectance model for the analysis of planetary surface hyperspectral images at visible and near-infrared wavelengths,* J. Geophys. Res., 103(E13), 31367–31389, doi:10.1029/98JE01894.

Dumont, M., E. Brun, G. Picard, M. Michou, Q. Libois, J. R. Petit, M. Geyer, S. Morin, and B. Josse, (2014), *Contribution of light-absorbing impurities in snow to Greenland/'s darkening since 2009,* Nature Geoscience 7(7), 509-512, doi:10.1038/ngeo2180.

European Committee for Standardization, (2003), *EN 1991-1- 1: Eurocode 1 – Actions on Structures – Part 1–3: General Actions – Snow Loads.* European Committee for Standardization: Brussels

Fink, U., N. H. Dekkers, and H. P. Larson, (1973), *Infrared spectra of the Galilean satellites of Jupiter,* The Astrophysical Journal, 179, L155.

Flanner, M. G., C. S. Zender, J. T. Randerson, and P. J. Rasch (2007), *Present day climate forcing and response from black carbon in snow,* J. Geophys. Res., 112, D11202, doi:10.1029/2006JD008003.

Flanner, M. G., C. S. Zender, P. G. Hess, N. M. Mahowald, T. H. Painter, V. Ramanathan, and P. J. Rasch (2009), *Springtime warming and reduced snow cover from carbonaceous particles,* Atmos. Chem. Phys., 9, 2481-2497.

Flanner, M. G., K. M. Shell, M. Barlage, D. K. Perovich, and M. A. Tschudi, (2011), *Radiative forcing and albedo feedback from the Northern Hemisphere cryosphere between 1979 and 2008,* Nature Geoscience., 4(3), 151–155, doi:10.1038/ngeo1062.

Flato, G., et al. (2013), Evaluation of Climate Models. In: Climate Change 2013: *The Physical Science Basis. Contribution of Working Group I to the Fifth Assessment Report of the Intergovernmental Panel on Climate Change* [Stocker, T. F., et al. (eds.)]. Cambridge University Press, Cambridge, United Kingdom and New York, NY, USA, 741–866, doi:10.1017/CBO9781107415324.020.

Forget, F. (1998), *Mars CO_2 ice polar caps,* In Solar System Ices, Springer Netherlands, 477-507.

Forget, F., F. Hourdin, and O. Talagrand (1998), *CO_2 snowfall on Mars: Simulation with a general circulation model,* Icarus, 131(2), 302-316, doi:10.1006/icar.1997.5874.

Forget, F., F. Hourdin, R. Fournier, C. Hourdin, O. Talagrand, M. Collins, S. R. Lewis, P. L. Read, and J.-P. Huot (1999), *Improved general circulation models of the Martian atmosphere from the surface to above 80 km,* J. Geophys. Res., 104(E10), 24155–24175, doi:10.1029/1999JE001025.

Fouquart, Y., and B. Bonnel, (1980), *Computations of solar heating of the earth's atmosphere- A new parameterization,* Beitraege zur Physik der Atmosphaere, 53, 35-62.

Fu, Q. (2007), *A new parameterization of an asymmetry factor of cirrus clouds for climate models,* J. Climate, 64, 4140-4150, doi: 10.1175/2007JAS2289.1

Gardner, A. S., et al., (2013), *A reconciled estimate of glacier contributions to sea level rise: 2003 to 2009,* Science, 340, 852-857.

Greeley, R., et al., (1998), *Europa: initial Galileo geological observations,* Icarus, 135(1), 4-24.

Hansen, G. B. (1997), *The infrared absorption spectrum of carbon dioxide ice from 1.8 to 333 μm,* J. Geophys. Res., 102(E9), 21569–21587, doi:10.1029/97JE01875.

Hansen, G. B. (1999), *Control of the radiative behavior of the Martian polar caps by surface CO_2 ice: Evidence from Mars Global Surveyor measurements,* J. Geophys. Res., 104(E7), 16471–16486, doi:10.1029/1998JE000626.

Hansen, G. B. (2005), *Ultraviolet to near-infrared absorption spectrum of carbon dioxide ice from 0.174 to 1.8 μm,* J. Geophys. Res., 110, E11003, doi:10.1029/2005JE002531.

Hansen, J. E., and L. D. Travis (1974), *Light scattering in planetary atmospheres,* Space Science Reviews, 16(4), 527-610.

He, T., S. Liang, D. Wang, H. Wu, Y. Yu, and J. Wang, (2012), *Estimation of surface albedo and directional reflectance from Moderate Resolution Imaging Spectroradiometer (MODIS) observations,* Remote Sensing of Environment, 119, 286-300.

Herr, K. C., and G. C. Pimentel (1969), *Infrared absorptions near three microns recorded over the polar cap of Mars,* Science, 166(3904), 496-499.

Hess, S. L., J. A. Ryan, J. E. Tillman, R. M. Henry, and C. B. Leovy (1980), *The annual cycle of pressure on Mars measured by Viking Landers 1 and 2,* Geophys. Res. Lett., 7: 197–200. doi:10.1029/GL007i003p00197.

Hess, S. L., R. M. Henry, C. B. Leovy, J. A. Ryan, and J. E. Tillman (1977), *Meteorological results from the surface of Mars: Viking 1 and 2,* J. Geophys. Res., 82(28), 4559–4574, doi:10.1029/JS082i028p04559.

Hourdin, F., F. Forget, and O. Talagrand (1995), *The sensitivity of the Martian surface pressure and atmospheric mass budget to various parameters: A comparison between numerical simulations and Viking observations,* J. Geophys. Res., 100(E3), 5501–5523, doi:10.1029/94JE03079.

Hourdin, F., P. Le Van, F. Forget, and O. Talagrand, (1993), *Meteorological variability and the annual surface pressure cycle on Mars,* Journal of the atmospheric sciences, 50(21), 3625-3640, doi: 10.1175/1520-0469(1993)050<3625:MVATAS>2.0.CO;2

Hudson, S. R., *Estimating the global radiative impact of the sea ice–albedo feedback in the Arctic,* J. Geophys. Res., 116, D16102, doi:10.1029/2011JD015804, 2011.

Kahre, M. A., and R. M. Haberle, (2010), *Mars CO 2 cycle: Effects of airborne dust and polar cap ice emissivity,* Icarus, 207(2), 648-653, doi:10.1016/j.icarus.2009.12.016

Kargel, J. S. (2006), *Enceladus: cosmic gymnast, volatile miniworld,* Science, 311(5766), 1389-1391.

Kay, J. E., M. M. Holland, C. M. Bitz, E. Blanchard-Wrigglesworth, A. Gettelman, A. Conley, and D. Bailey, (2012), *The influence of local feedbacks and northward heat transport on the equilibrium Arctic climate response to increased greenhouse gas forcing,* J. Clim., 25(16), 5433–5450, doi:10.1175/JCLI-D-11-00622.1, 2012.

Keegan, K. M., M. R. Albert, J. R. McConnell, and I. Baker, (2014), *Climate change and forest fires synergistically drive widespread melt events of the Greenland Ice Sheet,* Proceedings of the National Academy of Sciences,111(22), 7964-7967.

Kieffer, H. H., and T. N. Titus, (2001), *TES mapping of Mars' north seasonal cap,* Icarus, 154(1), 162-180.

Kieffer, H. H., T. N. Titus, K. F. Mullins, and P. R. Christensen, (2000), *Mars south polar spring and summer behavior observed by TES: Seasonal cap evolution controlled by frost grain size,* J. Geophys. Res., 105(E4), 9653–9699, doi:10.1029/1999JE001136.

Kieffer, H. H., T. Z. Martin, A. R. Peterfreund, B. M. Jakosky, E. D. Miner, and F. D. Palluconi (1977), *Thermal and albedo mapping of Mars during the Viking primary mission,* J. Geophys. Res., 82(28), 4249–4291, doi:10.1029/JS082i028p04249.

Labs, D., H. Neckel (1968), *The Radiation of the Solar Photosphere from 2000 Å to 100 μm,* Zeitschrift fur Astrophysik, 69, 1.

Langevin, Y., J.-P. Bibring, F. Montmessin, F. Forget, M. Vincendon, S. Douté, F. Poulet, and B. Gondet (2007), *Observations of the south seasonal cap of Mars during recession in 2004–2006 by the OMEGA visible/near-infrared imaging spectrometer on board Mars Express,* J. Geophys. Res., 112, E08S12, doi:10.1029/2006JE002841.

Larson, H. P., and U. Fink (1972), *Identification of carbon dioxide frost on the Martian polar caps.* The Astrophysical Journal, 171, L91.

Leighton, R. B., and B. C. Murray (1966), *Behavior of carbon dioxide and other volatiles on Mars,* Science, 153(3732), 136-144.

Leovy, C. E., R. W. Zurek, and J. B. Pollack, (1973), *Mechanisms for Mars dust storms. Journal of the Atmospheric Sciences,* 30(5), 749-762, doi: 10.1175/1520-0469(1973)030<0749:MFMDS>2.0.CO;2.

Libois, Q., G. Picard, J. L. France, L. Arnaud, M. Dumont, C. M. Carmagnola, and M. D. King (2013), *Influence of grain shape on light penetration in snow,* The Cryosphere, 7, 1803-1818, doi:10.5194/tc-7-1803-2013.

Lopez-Puertas, M., and M. A. López-Valverde (1995), *Radiative energy balance of CO_2 non-LTE infrared emissions in the Martian atmosphere,* Icarus, 114(1), 113-129, doi:10.1006/icar.1995.1047.

Lyapustin, A., et al., (2014), *Scientific impact of MODIS C5 calibration degradation and C6+ improvements,* Atmos. Meas. Tech., 7, 4353-4365, doi:10.5194/amt-7-4353-2014.

Madeleine, J.-B., F. Forget, E. Millour, L. Montabone, and M. J. Wolff (2011), *Revisiting the radiative impact of dust on Mars using the LMD Global Climate Model,* J. Geophys. Res., 116, E11010, doi:10.1029/2011JE003855.

Manabe, S., and R. J. Stouffer, (1994), *Multiple-century response of a coupled ocean–atmosphere model to an increase of atmospheric carbon dioxide,* J. Clim., 7, 5–23.

Manabe, S., M. J. Spelman, and R. J. Stouffer, (1992), *Transient response of a coupled ocean–atmosphere model to gradual changes of atmospheric CO2. Part II: Seasonal response,* J. Clim., 5, 105–126.

Meehl, G. A., and W. M. Washington, (1990), *CO_2 climate sensitivity and snow-sea-ice parameterization in an atmospheric GCM coupled to a mixed-layer ocean model,* Climate Change, 16**,** 283–306.

Miller, J. R., and G. L. Russell, (2000), *Projected impact of climatic change on the freshwater and salt budgets of the Arctic Ocean by a GCM,* Geophys. Res. Lett., 27, 1183–1186.

Mitri, G., A. P. Showman, J. I. Lunine, and R. D. Lorenz, (2007), *Hydrocarbon lakes on Titan,* Icarus, 186(2), 385-394.

Monaghan, A. J., D. H. Bromwich, W. Chapman, and J. Comiso, (2008), *Recent variability and trends of Antarctic near-surface temperature,* J. of Geophy. Res., 113, D04105, doi: 10.1029/2007JD009094, 2008.

Montmessin, F., and F. Lefèvre (2013), *Transport-driven formation of a polar ozone layer on Mars,* Nature geoscience, 6(11), 930-933, doi:10.1038/ngeo1957.

Moody, E. G., M. D. King, C. B., Schaaf, and S. Platnick, (2008), *MODIS-derived spatially complete surface albedo products: Spatial and temporal pixel distribution and zonal averages,* J. Appl. Meteor., 47 (11), 2879-2894, doi:10.1175/2008JAMC1795.1, 2008.

Morrison, D., and T. Owen (1996), *The planetary system. The planetary system., by Morrison, D.; Owen, T., Addison-Wesley Publishing, Reading, MA (USA),* 1996, XVI+ 570 p., ISBN 0-201-55450-X, 1.

Nolin, A., R. L. Armstrong, and J. Maslanik, (1998), *Near-Real-Time SSM/I-SSMIS EASE-Grid Daily Global Ice Concentration and Snow Extent. Version 4 (2001-2013),* Boulder, Colorado USA: NASA DAAC at the National Snow and Ice Data Center.

Ockert-Bell, M. E., J. F. Bell III, J. B. Pollack, C. P. McKay, and F. Forget (1997), *Absorption and scattering properties of the Martian dust in the solar wavelengths,* J. Geophys. Res., 102(E4), 9039–9050, doi:10.1029/96JE03991.

Perket, J., M. G. Flanner, and J. E. Kay (2014), *Diagnosing shortwave cryosphere radiative effect and its 21st century evolution in CESM,* J. Geophys. Res. Atmos., 119, 1356–1362, doi:10.1002/2013JD021139.

Picard, G., F. Domine, G. Krinner, L. Arnaud, and E. Lefebvre, (2012*), Inhibition of the positive snow-albedo feedback by precipitation in interior Antarctica,* Nature Climate Change, vol. 2, 795 -798.

Pierrehumbert, R. T. (2010), *Principles of planetary climate,* Cambridge University Press.

Pistone, K., I. Eisenman, and V. Ramanathan, (2014), *Observational determination of albedo decrease caused by vanishing Arctic sea ice,* Proc. Natl. Acad. Sci. USA, 111, 3322–3326, doi:10.1073/pnas.1318201111.

Qu, X. and A. Hall, (2005), *Surface contribution to planetary albedo variability in cryosphere regions,* J. Clim. 18, 5239-5252.

Qu, X., and A. Hall (2007), *What controls the strength of snow-albedo feedback?,* J. Clim. 20: 3971-3981, 2007.

Quick, L. C., O. S. Barnouin, L. M. Prockter, and G. W. Patterson (2013), *Constraints on the detection of cryovolcanic plumes on Europa,* Planetary and Space Science, 86, 1-9.

Quirico, E., and B. Schmitt, (1997), *Near-infrared spectroscopy of simple hydrocarbons and carbon oxides diluted in solid N_2 and as pure ices: Implications for Triton and Pluto,* Icarus, 127(2), 354-378, doi:10.1006/icar.1996.5663.

Räisänen, P., A. Kokhanovsky, G. Guyot, O. Jourdan, and T. Nousiainen (2015), *Parameterization of single-scattering properties of snow,* The Cryosphere, 9, 1277-1301, doi:10.5194/tc-9-1277-2015.

Randall, D.A. et al. (2007), *The Physical Science Basis. Contribution of Working Group I to the Fourth Assessment Report of the Intergovernmental Panel on Climate Change* [Solomon, S., et al. (eds.)]. Cambridge University Press, Cambridge, United Kingdom and New York, NY, USA.

Rignot, E., I. Velicogna, M. R. van den Broeke, A. Monaghan, and J. T. M. Lenaerts, (2011), *Acceleration of the contribution of the Greenland and Antarctic ice sheets to sea level rise,* Geophys. Res. Lett., 38, L05503, doi:10.1029/2011GL046583.

Robinson, D. A., and A. Frei, (2000), *Seasonal variability of northern hemisphere snow extent using visible satellite data,* Professional Geographer, 51, 307-314.

Roman, M. O., C. B. Schaaf, P. Lewis, F. Gao, G. P. Anderson, J. L. Privette, A. H. Strahler, C. E. Woodcock, and M. Barnsley (2010), *Assessing the Coupling between Surface Albedo derived from MODIS and the Fraction of Diffuse Skylight over Spatially-Characterized Landscapes,* Remote Sensing of Environment 114 (4): 738–760. doi:10.1016/j.rse.2009.11.014.

Ryan, J. A., R. D. Sharman, and R. D. Lucich (1981), *Local Mars dust storm generation mechanism,* Geophys. Res. Lett., 8(8), 899–901, doi:10.1029/GL008i008p00899.

Schaaf, C. B., et al., (2002), *First operational BRDF, albedo nadir reflectance products from MODIS,* Remote Sensing of Environment, 83, 135–148.

Serreze, M. C., M. M. Holland, and J. Stroeve, (2007), *Perspectives on the Arctic's shrinking sea-ice cover,* Science, 315, 1533-1536, doi:10.1126/science.1139426.

Shell, K. M., J. T. Kiehl, and C. A. Shields, (2008), *Using the radiative kernel technique to calculate climate feedbacks in NCAR's community atmospheric model,* J. Clim. 21, 2269-2282.

Singh, D., M. G. Flanner, and J. Perket, (2015), *The global land shortwave cryosphere radiative effect during the MODIS era,* The Cryosphere, 9, 2057-2070, doi:10.5194/tc-9-2057-2015.

Soden, B. J., I. M. Held, R. Colman, K. M. Shell, J. T., Kiehl, and C. A. Shields (2008), *Quantifying climate feedbacks using radiative kernels,* J. Clim., 21(14), 3504–3520, doi:10.1175/2007JCLI2110.1.

Sokolik, I. N., and O. B. Toon (1999), *Incorporation of mineralogical composition into models of the radiative properties of mineral aerosol from UV to IR wavelengths,* J. Geophys. Res., 104(D8), 9423–9444, doi:10.1029/1998JD200048.

Sotin, C., et al., (2005), *Release of volatiles from a possible cryovolcano from near-infrared imaging of Titan,* Nature, 435(7043), 786-789.

Spencer, J. R. (1987). *Thermal segregation of water ice on the Galilean satellites,* Icarus, 69(2), 297-313.

Spencer, J. R., et al., (2009), *Enceladus: An active cryovolcanic satellite. In Saturn from Cassini-Huygens* (pp. 683-724), Springer Netherlands.

Steig, E., D. P. Schneider, S. D. Rutherford, M. Mann, J. C. Comiso, and D. T. Shindell, (2009), *Warming of the Antarctic ice-sheet surface since the 1957 International Geophysical Year,* Nature 457, 459-462, doi: 10.1038/nature07669.

Stern, S. A., et al., (2015), *The Pluto system: Initial results from its exploration by New Horizons,* Science, 350(6258), aad1815.

Stofan, E. R., C. Elachi, J. I. Lunine, R. D. Lorenz, B. Stiles, K. L. Mitchell, S. Ostro, L. Soderblom, C. Wood, H. Zebker, and S. Wall, (2007), *The lakes of Titan,* Nature, 445(7123), 61-64.

Stroeve, J., L. Hamilton, C. M. Bitz, and E. Blanchard-Wrigglesworth (2014), *Predicting September Sea Ice: Ensemble Skill of the SEARCH Sea Ice Outlook 2008–2013,* Geophy. Res. Lett., 41, 2411–2418, doi: 10.1002/2014GL059388.

Stroncik, N. A., and H. U. Schmincke (2002), *Palagonite–a review,* International Journal of Earth Sciences, 91(4), 680-697.

Sun, J., X. Xiong, A. Angal, H. Chen, A. Wu, and X. Geng, (2014), *Time-dependent response versus scan angle for MODIS reflective solar bands,* Geoscience and Remote Sensing, IEEE Transactions on 52.6: 3159-3174.

Tedesco, M., J. E. Box, J. Cappelen, X. Fettweis, T. Mote, R. S. W. van de Wal, C. J. P. P. Smeets, J. Wahr, (2014), *Greenland Ice Sheet [in Arctic Report Card 2014]*, http://www.arctic.noaa.gov/reportcard.

Tillman, J. E., N. C. Johnson, P. Guttorp, and D. B. Percival (1993), *The martian annual atmospheric pressure cycle: Years without great dust storms,* Journal of Geophysical Research: Planets (1991–2012), 98(E6), 10963-10971.

Titus, T. N., H. H. Kieffer, K. F. Mullins, and P. R. Christensen (2001), *TES premapping data: Slab ice and snow flurries in the Martian north polar night,* J. Geophys. Res., 106(E10), 23181–23196, doi:10.1029/2000JE001284.

Toon, O. B., C. P. McKay, T. P. Ackerman, and K. Santhanam (1989), *Rapid calculation of radiative heating rates and photodissociation rates in inhomogeneous multiple scattering atmospheres,* J. Geophys. Res., 94 (D13), 16287-16301, doi:10.1029/JD094iD13p16287.

Trafton, L. M. (2015), *On the state of methane and nitrogen ice on Pluto and Triton: Implications of the binary phase diagram,* Icarus, 246, 197-205.

Vaughan, D.G., et al., (2013), *Observations: Cryosphere. In: Climate Change 2013: The Physical Science Basis. Contribution of Working Group I to the Fifth Assessment Report of the Intergovernmental Panel on Climate Change* [Stocker, T.F., et al., (eds.)]. Cambridge University Press, Cambridge, United Kingdom and New York, NY, USA, 317–382, doi:10.1017/CBO9781107415324.012.

Verbiscer, A. J., and J. Veverka, (1994), *A photometric study of Enceladus,* Icarus, 110(1), 155-164.

Verbiscer, A., R. French, M. Showalter, and P. Helfenstein, (2007), *Enceladus: Cosmic graffiti artist caught in the act,* Science, 315(5813), 815-815.

Warren, S. G., and R. E. Brandt (2008), *Optical constants of ice from the ultraviolet to the microwave: A revised compilation,* J. Geophys. Res., 113, D14220, doi:10.1029/2007JD009744.

Warren, S. G., W. J. Wiscombe, and J. F. Firestone (1990), *Spectral albedo and emissivity of CO_2 in Martian polar caps: Model results,* J. Geophys. Res., 95(B9), 14717–14741, doi:10.1029/JB095iB09p14717.

Winton, M. (2006), *Surface albedo feedback estimates for the AR4 climate models,* J. Clim. 19, 359-365.

Wiscombe, W. J., and S. G. Warren (1980), *A Model for the Spectral Albedo of Snow. I: Pure Snow*, J. Atmos. Sci., 37, 2712–2733, doi:10.1175/1520-0469(1980)037<2712:AMFTSA>2.0.CO;2

Wolff, M. J., M. D. Smith, R. T. Clancy, R. Arvidson, M. Kahre, F. Seelos IV, S. Murchie, and H. Savijarvi (2009), *Wavelength dependence of dust aerosol single scattering albedo as observed by the Compact Reconnaissance Imaging Spectrometer,* J. Geophys. Res., 114, E00D04, doi:10.1029/2009JE003350.

Wolff, M. J., R. T. Clancy, J. D. Goguen, and M. C. Malin, and B. A. Cantor (2010), *Ultraviolet dust aerosol properties as observed by MARCI,* Icarus, 208(1), 143-155.

Wolff, M.J., M. D. Smith, R. T. Clancy, N. Spanovich, B. A. Whitney, M. T. Lemmon, J. L. Bandfield, D. Banfield, A. Ghosh, G. Landis, P. R. Christensen, J. F. Bell III and S. W. Squyres (2006), *Constraints on dust aerosols from the Mars Exploration Rovers using MGS overflights and Mini-TES,* J. Geophys. Res., 111, E12S17, doi:10.1029/2006JE002786.

Zurek, R. W., and C. B. Leovy (1981), *Thermal tides in the dusty Martian atmosphere: A verification of theory,* Science, 213(4506), 437-439, doi: 10.1126/science.213.4506.437.

Zurek, R. W., and L. J. Martin (1993), *Interannual variability of planet-encircling dust storms on Mars,* J. Geophys. Res., 98(E2), 3247–3259, doi:10.1029/92JE02936.